

INSTITUTE OF PHYSICS
POLISH ACADEMY OF SCIENCES

Paweł Jakubas

**Theory of generation of Frenkel pairs in
semiconductors: consequences for
electric, magnetic, and structural
properties**

PH. D. DISSERTATION

**SUPERVISOR
PROF. PIOTR BOGUSŁAWSKI
INSTITUTE OF PHYSICS
POLISH ACADEMY OF SCIENCES**

June 2009

Contents

Scientific activity during PhD studies	4
Introduction	8
Chapter 1. Methods of calculation	11
1.1 Density Functional Theory	11
1.2 Methodology of formation energy calculation of defects	14
1.2.1 The defect formation energy formula	14
1.2.1.1 Chemical potentials	15
1.2.1.2 Determination of VBM	17
1.2.1.3 Potential alignment correction of VBM	18
1.2.1.4 Image charge correction	18
1.2.1.5 Band filling correction	19
1.2.1.6 Band gap correction	20
1.2.1.7 Finite-size effects	22
1.2.2 Transition energy levels	23
1.3 Minimal energy path of rare events	23
1.3.1 NEB methods	24
Chapter 2. Native defects in CdTe and ZnTe	27
2.1 Cation vacancies	27
2.1.1 Diffusion of cation vacancies	31
2.1.1.1 Diffusion to the first neighbor	31
2.1.1.2 Diffusion to the second neighbor	33
2.1.1.3 Diffusion to the fourth neighbor	36
2.2 Cation interstitials	38
2.2.1 Zn and Cd interstitials in CdTe	39
2.2.2 Zn and Cd interstitials in ZnTe	45
2.2.3 Diffusion of cation interstitials	47
2.3 Anion vacancies	51
2.3.1 Diffusion of anion vacancies	58

2.4	Anion interstitials	59
2.4.1	Diffusion of anion interstitials	66
2.5	Compensation of doping by vacancies and interstitials	67
Chapter 3. Frenkel pairs in CdZnTe		68
3.1	Cation sublattice	68
3.2	Anion sublattice	82
3.3	Conductivity switching and electric polarization effects – a microscopic model	89
3.4	Influence of the electrical conductivity on magnetic properties of CdZnMnTe	94
Chapter 4. Frenkel pairs in other semiconductors		98
4.1	GaAs	98
4.2	3C-SiC	101
4.3	ZnO	105
4.4	GaN	112
Conclusions		116
References		119

Scientific activity during PhD studies

PUBLICATIONS

1. ‘Magnetism of CaAs, CaP, and CaN half-metals’, O. Volnianska, *P. Jakubas*, and P. Bogusławski. *J. Alloys and Compounds* **423** (2006) 191-193.
2. ‘Ferroelectricity in ternary (Cd,Zn)A_{VI} crystals’, T. Wojciechowski, *P. Jakubas*, P. Bogusławski, and G. Karczewski, *J. of Korean Phys. Soc.* **53** (1): 23-27 Jul 2008.
3. ‘Generation of native defects as a possible origin of resistivity switching and ferroelectric properties in CdZnTe’, *P. Jakubas* and P. Bogusławski, *Phys. Rev. B* **77**, 214104 (2008).
4. ‘Influence of the electrical conductivity on magnetic properties of CdZnMnTe epitaxial layers’, T. Wojciechowski, *P. Jakubas*, V. Kolkovsky, K. Świątek, W. Knoff, T. Story, P. Bogusławski, and G. Karczewski, conference paper in 29th International Conference on the Physics of Semiconductors, Rio de Janeiro (Brazil) – 2008.
5. ‘Microscopic stability and generation of Frenkel pairs in (Cd,Mn,Zn)Te and ZnO: ab-initio study’, *P. Jakubas*, Science and Supercomputing in Europe: report 2008, HPC-Europa ++, 2008 CINECA Consorzio Interuniversitario, p. 521.
6. ‘Theory of Frenkel pairs in semiconductors’, *P. Jakubas* and P. Bogusławski – in preparation.

RESEARCH STAYS ABROAD

1. Scuola Normale Superiore, Pisa (Italy) – September 2005 (1 month).
2. CINECA, Bologna (Italy) – September 2008 (1 month)

PARTICIPATION IN RESEARCH GRANTS

1. Nosce Memorias grant N 5070934 funded under the 6th EU Framework programme; project’s duration - 1 January 2004 to 31 March 2007; responsible for theoretical inquiries into defect physics, conductivity switching phenomena and electric polarization in CdZnTe.

2. HPC-Europa Transnational Access programme (CINECA) grant N RII3-CT-2003-506079; the project duration – 1 September 2005 to 31 December 2006; topic: Researching ferroelectricity in (Cd,Zn)Te alloys.
3. Interdisciplinary Centre for Mathematical and Computational Modeling (Warsaw University) computational grant G16-11; the project duration - September 2004 to present; topic: Researching semiconductor physics from first principles.
4. HPC-Europa++ Transnational Access programme (CINECA) grant N RII3-CT-2003-506079; the project duration - 25 August 2008 to 31 December 2008; topic: Researching Frenkel Pair formation from first principles.
5. Polish Ministry of Science and Higher Education PhD grant N N202 172935; the project duration -September 2008 to August 2009; topic: Microscopic structural stability and Frenkel pair formation in GaN, SiC, and ZnO from first principles calculations.
6. Mazovia PhD grant N 1058/6; the project duration – October 2008 to June 2009.

TALKS AND PRESENTATIONS

1. ‘Electron Beam Lithography In Laboratory Practice’, J. Wróbel, *P. Jakubas*, CEPHONA Workshop on Semiconductor Processing, Warsaw (Poland), 30 September – 2 October 2004 – **invited talk**
2. ‘Calculated magnetic properties of MgP, MgAs, CaP, and CaAs’, O. Volnianska, *P. Jakubas*, P. Bogusławski, XXXIV International School on the Physics of Semiconducting Compounds, Jaszowiec (Poland), 4 – 10 June, 2005 – **oral presentation**
3. ‘Structural stability of (Ga,Mn)As and (Cd,Mn)Te alloys by ab-initio calculations’, *P. Jakubas*, P. Bogusławski, XXXIV International School on the Physics of Semiconducting Compounds, Jaszowiec (Poland), 4 – 10 June, 2005 – **poster presentation**
4. ‘Structural stability and formation of MnAs inclusions in (Ga,Mn)As’, *P. Jakubas*, P. Bogusławski, E-MRS 2005 Fall Meeting, Symposium D: Magnetoelectronics, Warsaw University of Technology (Poland), 5-9 September, 2005 – **oral presentation**
5. ‘Theoretical investigations of the electrical polarization in (Cd,Zn)Te’, *P. Jakubas*, P. Bogusławski, 12th International Conference on II-VI Compounds, Warsaw (Poland), 12-16 September, 2005 – **poster presentation**
6. ‘Structural Stability and the Formation of Mn-rich Inclusions in Magnetic Semiconductors: (Ga,Mn)As, (Zn,Mn)Te, and (Cd,Mn)Te’, *P. Jakubas*, N. G. Szwacki, P. Boguslawski, J. Bernholc, 2005 MRS Fall Meeting, Symposium II: Fabrication and Characterization Methods

for Novel Magnetic Nanostructures, Boston (USA), 27 – 30 November, 2005 – **oral presentation**

7. ‘Structural Stability and the Formation of Magnetic Inclusions in (Ga,Mn)As and (Cd,Mn)Te’, *P. Jakubas*, P. Bogusławski, XI Workshop on Semimagnetic Semiconductors – Materials for Spintronics, Obory (Poland), 17 December, 2005 – **oral presentation**

8. ‘Ferromagnetism without transition metal atoms: CaN, SrN, and BaN’, O. Volnianska, *P. Jakubas*, P. Bogusławski, XI Workshop on Semimagnetic Semiconductors – Materials for Spintronics, Obory (Poland), 17 December, 2005 – **oral presentation**

9. ‘Formation and properties of interstitial Zn in (Cd,Zn)Te’, *P. Jakubas*, P. Bogusławski, XXXV International School on the Physics of Semiconducting Compounds, Jaszowiec (Poland), 17 – 23 June, 2006 – **oral presentation**

10. ‘Generation of native defects in (Cd,Zn)Te: a possible origin of resistive switching and ‘dark defects’’, *P. Jakubas*, P. Bogusławski, XXXVI International School on the Physics of Semiconducting Compounds, Jaszowiec (Poland), 9 – 15 June, 2007 – **oral presentation**

11. ‘Energy band structure of (Zn,Be)O and (Zn,Mg)O’, *P. Jakubas*, P. Bogusławski, XXXVI International School on the Physics of Semiconducting Compounds, Jaszowiec (Poland), 9 – 15 June, 2007 – **poster presentation**

12. ‘Ferroelectricity in ternary (Cd,Zn)AVI crystals’, T. Wojciechowski, *P. Jakubas*, P. Bogusławski, G. Karczewski, II-VI 2007, The 13th International Conference on II-VI Compounds, 10-14 September, 2007 Jeju, Korea - **oral presentation**

13. ‘Influence of the electrical conductivity on magnetic properties of CdZnMnTe epitaxial layers’, *P. Jakubas*, T. Wojciechowski, V. Kolkovsky, K. Świątek, W. Knoff, T. Story, P. Bogusławski, G. Karczewski, XXXVII International School on the Physics of Semiconducting Compounds, Jaszowiec (Poland), 7 – 13 June, 2008 – **oral presentation**

14. ‘Crystal stability of representative IV-IV, II-VI and III-V compounds in the context of Frenkel pairs generation’, *P. Jakubas*, P. Bogusławski, XXXVII International School on the Physics of Semiconducting Compounds, Jaszowiec (Poland), 7 – 13 June, 2008 – **poster presentation**

15. ‘Influence of the electrical conductivity on magnetic properties of CdZnMnTe epitaxial layers’, T. Wojciechowski, *P. Jakubas*, V. Kolkovsky, K. Świątek, W. Knoff, T. Story, P. Bogusławski, G. Karczewski, 29th International Conference on the Physics of Semiconductors, Rio de Janeiro (Brazil), 27 July – 1 August, 2008 - **poster presentation**

16. ‘Theory of interfacial interdiffusion and electromigration of H, dopants, and vacancies in GaN/AlN’, P. Bogusławski, J. Bernholc, *P. Jakubas*, N. Gonzalez Szwacki, Gordon Research

Conference on Defects in Semiconductors, August 3-8, 2008, Colby-Sawyer College, New London, NH (USA) - **invited talk**

17. 'Microscopic crystalline stability of SiC, III-V, and II-VI crystals in the context of high-power/high-temperature applications', *P. Jakubas*, P. Bogusławski, 14th International Workshop on Computational Physics and Materials Science: Total Energy and Force Methods, 8 - 10 January 2009, Trieste (Italy) – **poster presentation**

PARTICIPATION IN WORKSHOPS, SCHOOLS, TUTORIALS, FORUMS

1. Tutorial on Old and New Quasiparticles, XXXIV International School for the Physics of Semiconducting Compounds, Jaszowiec (Poland), 4 – 5 June 2005.

2. Tutorial on the ab-initio simulations of the electronic, structural and dynamical properties of materials: a hands-on introduction to the quantum-ESPRESSO package INFM-SLACS, Cagliari (Italy), 26 – 30 September 2005.

3. 14th International Winter school on New Developments in Solid State Physics: Charges and Spins in Nanostructures: Basis and Devices, Mauterndorf, Province of Salzburg (Austria), 13-17 February 2006.

4. Intel 11th EMEA Academic Forum, Dublin (Ireland), 30th and 31st May and 1st June 2006.

5. Tutorial on Novel Quantum Devices, XXXV International School for the Physics of Semiconducting Compounds, Jaszowiec (Poland), 17 - 18 June 2006.

6. 16th Jyväskylä Summer School, Jyväskylä (Finland), 31 July – 11 August 2006: Introduction to the Theory of Magnetic Nanostructures (30-hour course); Quantum Electromechanical Systems (15-hour course).

7. E-MRS 2007 Fall Meeting, Warsaw (Poland), 16th September 2007, GENETIC ALGORITHMS FOR BEGINNERS (Workshop).

Introduction

Defect physics has always been of paramount significance in materials research and technology. The understanding and control of defect engineering has enabled progress in wide range classes of materials, starting from metals and ending in semiconductors, which are the subject of this thesis. The proper comprehension of native defects and their complexes is essential to the successful application of any semiconductor. They are directly or indirectly responsible for compensation, doping, minority carrier lifetimes, luminescence efficiency, and a number of other crucial properties. The defects assist the diffusion mechanism, which influences growth, processing, and degradation of any device. Investigation of Frenkel pairs (FPs), which are the core subject of this thesis, has played an important role in the study of metals, where it was mainly analyzed from the point of view of mechanical properties. In semiconductors, FPs did not receive a lot of attention. At the beginning of defect physics, they played important role in studying native defects using irradiation experiments [1], their mutual interaction, and diffusion. Then, when the calculations from first principles became available, they were sometimes delved into, usually as a background to intensively covered native defects – see for example [2, 3]. Recently, Frenkel pairs in Si [4] and chalcopyrite semiconductors [5] were studied, but the treatment is also far from being comprehensive, although the papers constitute progress.

My motivation is to treat FP more deeply than it was up to this time, and devise a scheme that systematizes the approach to study this defect. I give special treatment to FPs in CdZnTe compound, and I cover them in the most detail out of all semiconductors, because (i) FPs in CdZnTe may be responsible for bistability effect and ‘dark defects’ in II-VI LEDs and finding theoretical explanation to these experimental conundrum engrossed my attention at the beginning of my PhD studies, (ii) the relative importance in comparison with other semiconductors, and (iii) my research group specializes in fabrication and investigation of this

compound. The methodology and approach implemented initially to FPs in CdZnTe is also utilized in the case of GaAs, SiC, ZnO, and GaN – already very important or/and emerging semiconductors. A FP is generated when an atom is ejected from its substitutional site, leaving vacancy behind, and stabilizes in the metastable position. In effect, interstitial-vacancy complex is created. The most important issues are following: how much does it cost to produce a FP? What influences this cost? What factors influence the stability of a FP? What are the optical, electrical, and magnetic consequences of FPs generation? It is significant to stress that if a FP generation cost is similar to the energy available in the material, it can substantially affect structural properties and behavior of the material. The valid and characteristic energy scales in material depends on the way of excitation: electric and optical transitions can be on the order of band gap, thus if a FP generation barrier is comparable to bandgap, the material can be unstable from the point of view of the FP generation. Thermal excitations define another scale that has to be taken into consideration while assessing the feasibility of activating rare events ruled by diffusion, generation, and recombination barriers. The organization of my PhD thesis can be advocated and justified as follows:

First of all, my approach bases on ab-initio supercell approach, which has its own limitations and errors. The calculation of formation energies has to be treated with due diligence, as it is the most fundamental quantity to be determined upon the study of defects. A judicious methodology correcting GGA and finite-size supercell errors has to be employed to guarantee correspondence to the experiment and predictive capabilities. The Chapter 1 is dedicated to this problem. The general information on Minimum Energy Path (MEP) methods is also covered in this chapter. The determination of MEP is important if one is interested in energy landscape, and thus the feasibility of dynamical transitions of defects, i.e., the determination of diffusion, generation, and recombination barriers. I use the most advanced methods available in both cases.

Second, because FP is a complex that is composed of two native defects, namely vacancy and interstitial, I focus on the native defects properties. As it follows later, the deep knowledge of native defects, i.e., constituents of a FP, is very important when studying the complex. I give special treatment to the calculation of formation energy, energy levels, and diffusion patterns of the native defects. The comprehensive study of both cation and anion vacancy and interstitials in CdTe and ZnTe is covered in Chapter 2.

Chapter 3 is dedicated to studying of FPs in CdTe and ZnTe. FPs are analyzed from the point of view of the interaction of their constituents. The discrepancies between FPs on

anion and cation sublattices are underlined. The generation of a FP is elucidated as a function of Fermi level. Charge state of FP determined by the type of doping, influences vehemently the generation barriers. The stability of FPs are investigated from the point of view of recombination and dissociation of their constituents. Finally, the FP's generation is relevant to experimentally established bistability in CdZnTe. Defect-induced changes of magnetic behavior in CdZnTe with Mn ions are also calculated and explained.

Chapter 4 deals with FPs in other important semiconductors. The special treatment is given to the comparison of generation of FPs in two different crystal structures, namely zinc blende and wurtzite. FPs in zinc blende GaAs and SiC were previously investigated and I compare my results with other authors. FPs in wurtzite GaN and ZnO were not addressed until my work.

I acknowledge the help, intellectual inspiration, and, highly revered by me, critical approach of my PhD supervisor, prof. P. Bogusławski. I also appreciate all scientific interactions with colleagues from Institute of Physics, Polish Academy of Sciences and other research and academic institutions I visited and collaborated with. I especially would like to thank prof. G. Karczewski and T. Wojciechowski for fruitful and numerous discussions on experiments in CdZnTe. Finally, I appreciate the support of Polish Ministry of Science and Higher Education, 6th UE Framework programme, HPC-Europa and HPC-Europa++ Transnational Access programmes, Interdisciplinary Centre for Mathematical and Computational Modeling, and Mazovia PhD grant.

Chapter 1

Methods of calculation

In this Chapter computational details are presented. Special treatment is given to the determination of defect's formation energy and the calculation of the lowest energy paths.

1.1 Density Functional Theory

Density functional theory (DFT) has become widely acknowledged and adopted theoretical machinery since its inception in sixties of the previous century [6]. Its numerous implementations have allowed to solve a plethora of problems in various fields, spanning from chemistry, to physics, to biology, and to materials science and technology. As it advanced and nurtured, and computational power increased, more complex issues and more realistic systems could have been tackled successfully. Although many challenges still remain, which unable desired accuracy of answers or restrain applicability in some important research areas, the techniques based on DFT have become mainstream and standard theoretical procedures when dealing with microscopic treatment of various material problems. The approach is well established now, an array of codes are available, and the field, which already has a huge number subfields (and counting), is burgeoning.

By and large, DFT allows solving many-body Schrödinger equation adopting ab-initio approach, i.e., one where calculations are only based on the laws of physics and the values of nature constants. Because the interesting problems consist usually a considerable or a huge number of ions and electrons, several approximations had to be invented. First of all, Born-

Oppenheimer approximation which separates the motion of ions and electrons is usually implemented. The approximation is justified due to different timescales of the two kinds of particles, and stems from substantial differences of their masses. In effect, the ions are treated as stationary with the electrons rearranging themselves to the ions configuration, which decreases significantly the computational burden. As a result, total Schrödinger equation can be separated into two equations: one for the nuclei, and the second for electrons corresponding to the frozen ionic configuration. The milestone was to treat electron density as the main quantity, and to show that expectation value of electron Hamiltonian can be expressed only depending on the electron density. It was possible to advance further after proving by Kohn and Hohenberg [7] that (i) the ground state expectation value of any observable is a unique functional of the exact ground state electron density, and that (ii) for a given external potential, the true density minimizes the total energy functional. Hence, all ground states properties, especially total energy of a system, can be extracted from the exact electron density if one can determine it. The holy grail then was to determine the exact electron density. The breakthrough was to show that the solving of many-body Hamiltonian can be mapped into the problem of noninteracting electrons moving in an effective potential coming from other electrons [8]. Using variational principle with restrain that the total electron density integrated over the space gives the constant number of electrons, Kohn and Sham rewrote the many-body Schrödinger equation in the form of one particle Kohn-Sham (K-S) equations that can be solved self-consistently. As a consequence, instead of minimizing the electron density functional of total energy, one has to solve eigenproblem as formulated by K-S equations. The challenge is to propose the form of exchange-correlation potential that is the only part of the effective potential and not known analytically. Many methods has been invented to address this problem, including the well known Local Density Approximation (LDA) or General Gradient Approximation (GGA). The properties of bulk crystals are very often of the research significance, thus to avoid dealing with the infinite numbers of electrons, the periodicity of the crystals is utilized. The effective potential is then periodic and the wavefunctions can be expanded in the form of plane waves using Bloch's theorem. This enables to use efficient Fast Fourier Transform algorithms during computation. Moreover, due to Bloch's theorem the eigenproblem of infinitely many electrons is translated into eigenproblem of finitely many k-points in reciprocal k-space. This trick is possible due to the exploitation of the fact that the first Brillouin zone entails all required k-points and because of the symmetry considerations that reduce the number of k-points to be calculated. The electronic part, to the good approximation, can be calculated using a small number of k-

points, making the cutoff energy and k-point mesh the parameters of convergence. Finally, the problem of representing the electrons in atoms had to be solved. The outer electrons that are engaged in chemical bonding of a crystal can be easily represented by plane waves (i.e. using a small number of plane waves), in opposition to the core electrons, which, to a good accuracy, can be treated as inert and localized. Because a computationally huge number of plane waves has to be entangled to represent core electrons, the pseudopotential approximation was invented [6].

The calculations have been performed using DFT in GGA [9]. The numerical implementation in the QUANTUM-ESPRESSO code [10] uses ultrasoft Vanderbilt pseudopotentials [11] and plane waves as the basis set. The Methfessel–Paxton smearing method [12] has been used for obtaining partial occupancies. The width of smearing has been chosen to be 0.272 eV. The cut-off energies of 408 eV for the plane waves' expansion and 1632 eV for the electronic charge density have been found to be sufficient in all studied cases to obtain convergent results. Ionic positions have been optimized until the forces acting on ions were smaller than $0.026 \text{ eV}\text{\AA}$. Large unit cells with 64, 128, 256, 512, and 1024 atoms have been employed. Thus, substitution of one Cd atom by Zn in CdTe corresponds to the CdZnTe alloy containing 3.1% of Zn (for 64 atom-supercell), and etc. Brillouin-zone summations have been performed using the Monkhorst–Pack scheme [13] with at least $3\times 3\times 3$ k -point mesh. The calculations do not include spin-orbit interaction.

Bulk Cd and Zn metals crystallize in the hexagonal-close packed (hcp) structure. Lattice parameters have been found with $16\times 16\times 16$ Monkhorst-Pack sampling. The results for Cd ($a=3.030 \text{ \AA}$, $c=5.752 \text{ \AA}$) agree with experiment [14] ($a=2.98 \text{ \AA}$, $c=5.62 \text{ \AA}$), and the results for Zn ($a=2.657 \text{ \AA}$, $c=4.963 \text{ \AA}$) are even closer to the experimental values [14] ($a=2.66 \text{ \AA}$, $c=4.95 \text{ \AA}$). Bulk Te crystallizes in the γ Se trigonal structure (space group $P3121$, no. 152). The calculated lattice parameters are $a=4.64 \text{ \AA}$, $c=6.01 \text{ \AA}$, and $u=0.249$. The cohesive energy, E_{coh} , of elemental solids is the difference between the total energies of a solid and of isolated atoms. The calculated values for Cd, Zn and Te are -0.76 , -1.13 , and -2.91 eV per atom, while the respective experimental values are -1.16 , -1.35 , and -2.19 eV [14]. The calculated lattice constants of CdTe and ZnTe are 6.62 and 6.21 \AA , while the experiment gives 6.46 and 6.10 \AA , respectively [15]. The cohesive energies of CdTe and ZnTe are the differences in total energy between the bulk E_{CdTe} and E_{ZnTe} and isolated atoms. The calculated $E_{\text{coh}}^{\text{CdTe}} = -4.61$ eV and $E_{\text{coh}}^{\text{ZnTe}} = -4.98$ eV per two atoms are reasonably close to the corresponding experimental values of -4.4 and -4.7 eV [16]; the calculated heats of formation are ΔH_f

(CdTe)=-0.94 eV and $\Delta H_f(\text{ZnTe})=-0.95$ eV, while the respective measured values are -0.86 and -0.92 eV [17]. The overall agreement with experiment is satisfactory. Finally, LDA and GGA are known to underestimate the band gaps of semiconductors. In our case, the calculated band gaps $E_{\text{gap}}^{\text{GGA}}$ of ZnTe and CdTe are 1.05 and 0.60 eV, respectively, while the corresponding experimental values $E_{\text{gap}}^{\text{exp}}$ are 2.39 and 1.60 eV.

The satisfactory correspondence between experiment and calculation results (obviously taking into consideration the common errors of GGA) was also obtained for compounds treated in Chapter 4, namely GaAs, SiC, ZnO, and GaN.

1.2 Methodology of formation energy calculation of defects

There are two main features that are important to know when it comes to the defect, namely its transition levels and its concentration. The former property implies whether the defect acts like an acceptor, donor, or both, and whether the defect is deep or shallow. The relative concentration of the defect determines whether its presence really influences the properties of the material. The formation energy is the foremost entity to be calculated, as it explicitly determines the concentration and the transition levels of the defect. The defect concentration N is related explicitly with its formation energy E_{form} by $N = N_0 \exp(-E_{\text{form}}/kT)$, where N_0 is the density of the appropriate lattice sites. The definition of the transition level requires previous clarification, thus is described after the introduction of the formation energy.

1.2.1 The defect formation energy formula

The formation energy of the defect is the energy required to generate the defect in the perfect crystal. There are two types of reservoirs, namely atoms and electrons reservoirs, that interchange particles with the perfect crystal upon the creation of the defect. The energy of the atom and electrons reservoir are determined by the chemical potential and Fermi energy, respectively.

Formation energy of a defect A in a charge state Q is defined as [18]:

$$E_{\text{form}}[A^Q] = E_{\text{tot}}[A^Q] - E_{\text{tot}}^{\text{bulk}} - \sum_i n_i \mu_i + Q(E_F + E_{\text{VBM}}^{\text{bulk}}) - \Delta E_{\text{form}} . \quad (1.1)$$

Here $E_{\text{tot}}[A^Q]$ is the total energy of a supercell containing the defect, $E_{\text{tot}}^{\text{bulk}}$ is the total energy of the ideal supercell, n_i is the number of i-th type of (host or impurity) atoms that are transferred from the supercell to the atom reservoir while forming the defect, $n_i = -1$ (+1) if an atom is removed (added), and μ_i is the chemical potential of the i-th atomic species. Thus, this part of the equation depicts the interchange of atoms between the perfect crystal and the atoms reservoirs.

The next expression in the sum quantifies the exchange of electrons between the perfect crystal and the electron reservoir depicted by Fermi energy, E_F , referenced to the maximum of the valence band (VBM). The VBM of the ideal crystal is denoted by $E_{\text{VBM}}^{\text{bulk}}$.

The last expression of the sum in the right hand side of Eq. (1.1), ΔE_{form} , includes any corrections that are applied to the basic energy formula and are described below.

1.2.1.1 Chemical potentials

Chemical potential of i-th atomic species μ_i is referenced here to the chemical potential of the elemental solid μ_i^{bulk} according to

$$\mu_i = \mu_i^{\text{bulk}} + \Delta\mu_i. \quad (1.2)$$

Cohesive energy of the elemental solid is obtained by subtracting the energy of the isolated atom from μ_i^{bulk} . Chemical potentials depend on experimental growth conditions, which range from cation-rich to Te-rich. They determine formation energies, because formation of a defect requires exchange of atoms between the host and the reservoirs. For instance, when a substitutional Zn_{Cd} is created, Zn atom is taken from the reservoir of Zn and embedded into the host substituting Cd, and the Cd atom is removed from the host and put into the reservoir of Cd. Consequently, E_{form} of Zn_{Cd} increases when the μ_{Zn} decreases and/or μ_{Cd} increases, as explicitly reflected in Eq. (1.1).

Chemical potentials are variables subject to firm bounds. For example, μ_{Cd} assumes the maximum value when the growth occurs under Cd-rich conditions, that is

$$\mu_{\text{Cd}} = \mu_{\text{Cd}}^{\text{bulk}}, \text{ and } \Delta\mu_{\text{Cd}} = 0. \quad (1.3a)$$

Thermodynamic equilibrium requires that μ_{Cd} cannot be higher than the energy of bulk Cd, $\mu_{\text{Cd}}^{\text{bulk}}$, otherwise precipitates of metal Cd in the bulk or at the surface would form. Similarly, Zn- or Te-rich conditions define the upper limits of μ_{Zn} by $\Delta\mu_{\text{Zn}} = 0$ and $\Delta\mu_{\text{Te}} = 0$, respectively. On the other hand, lower bounds of chemical potentials are given by, e. g.,

$$\Delta\mu_{\text{Cd}} + \Delta\mu_{\text{Te}} = \Delta H_f(\text{CdTe}), \quad (1.3b)$$

where $\Delta H_f(\text{CdTe})$ is the heat of formation of CdTe. Thus, in the case of CdTe at Cd-rich conditions, $\Delta\mu_{\text{Cd}} = 0$ eV, $\Delta\mu_{\text{Te}} = \Delta H_f(\text{CdTe}) = -0.94$ eV, and at the Te-rich conditions $\Delta\mu_{\text{Cd}} = \Delta H_f(\text{CdTe}) = -0.94$ eV and $\Delta\mu_{\text{Te}} = 0$ eV. Analogous relations hold for ZnTe.

Finally, possible formation of secondary phases between a dopant A and the constituents of a compound BC imposes additional limitations on the chemical potential of A, which in general affect dopant solubilities [18, 19]. In the case under study, when, e.g., Zn is introduced in CdTe it should be treated as a dopant. Consequently, besides the bounds (1.3a) and (1.3b), formation of ZnTe as a secondary phase in CdTe (and CdTe as secondary phase in ZnTe) should be considered. This imposes additional upper bounds on dopants in the considered compounds:

$$\Delta\mu_{\text{Zn}} + \Delta\mu_{\text{Te}} = \Delta H_f(\text{ZnTe}) \text{ for Zn in CdTe, and} \quad (1.4)$$

$$\Delta\mu_{\text{Cd}} + \Delta\mu_{\text{Te}} = \Delta H_f(\text{CdTe}) \text{ for Cd in ZnTe.}$$

In particular, in the case of Zn in CdTe at the Cd-rich growth conditions, $\Delta\mu_{\text{Cd}} = 0$ eV, $\Delta\mu_{\text{Te}} = \Delta H_f(\text{CdTe}) = -0.94$ eV according to Eq. (1.3), and $\Delta\mu_{\text{Zn}} = \Delta H_f(\text{ZnTe}) - \Delta\mu_{\text{Te}} = \Delta H_f(\text{ZnTe}) - \Delta H_f(\text{CdTe}) = -0.01$ eV according to Eq. (1.4). Thus, the excess chemical potentials of Zn and Cd are practically equal and vanishing. In this particular case, additional constrains (1.4) have no practical implications because $\Delta H_f(\text{ZnTe})$ and $\Delta H_f(\text{CdTe})$ are equal to within 0.01 eV. For the same reason chemical potentials of Zn and Cd are equal in all the remaining cases. However, it should be stressed that in general, when ΔH_f of the compounds under study are different, constrains (1.4) strongly affect the results. Similarly, the formation of secondary phases such as $\text{Cd}_{0.5}\text{Zn}_{0.5}\text{Te}$

practically does not affect the chemical potentials of Zn and Cd. This is because the heat of formation of $\text{Cd}_{0.5}\text{Zn}_{0.5}\text{Te}$ is equal to $\Delta H_f(\text{ZnTe})$ or $\Delta H_f(\text{CdTe})$ to within 0.01 eV. In other words, the mixing enthalpy of CdZnTe alloy is about 10 meV.

1.2.1.2 Determination of VBM

The energy $E_{\text{VBM}}^{\text{bulk}}$ is determined from the total energy difference between the perfect crystal with and without a hole at the VBM in the nondegenerate regime, i.e.,

$$E_{\text{VBM}}^{\text{bulk}}(q) = \lim_{q \rightarrow 0} \frac{E_{\text{tot}}^{\text{bulk}}(0) - E_{\text{tot}}^{\text{bulk}}(q)}{q} \quad (1.5)$$

In such a case, the energy of the VBM is tantamount to that of a dilute hole gas. The procedure is equivalent to the one with $q=1$, when the supercell size increases to the infinity. $E_{\text{VBM}}^{\text{bulk}}(q)$ converges to the K-S eigenvalue of the VBM, ε_{VBM} . Hence, the corresponding ε_{VBM} is set in Eq. (1.1). Figure 1.1 shows the energy difference defined in (1.5) as a function of $1/q$ in a 2 atom unit cell of CdTe and ZnTe. The problem is that ε_{VBM} depends on the unknown average potential that can be defined only up to a constant. This is why comparing the VBM between the different charged states one has to align the average potentials of the perfect crystal and the defected crystal (see Sec. 1.2.1.3)

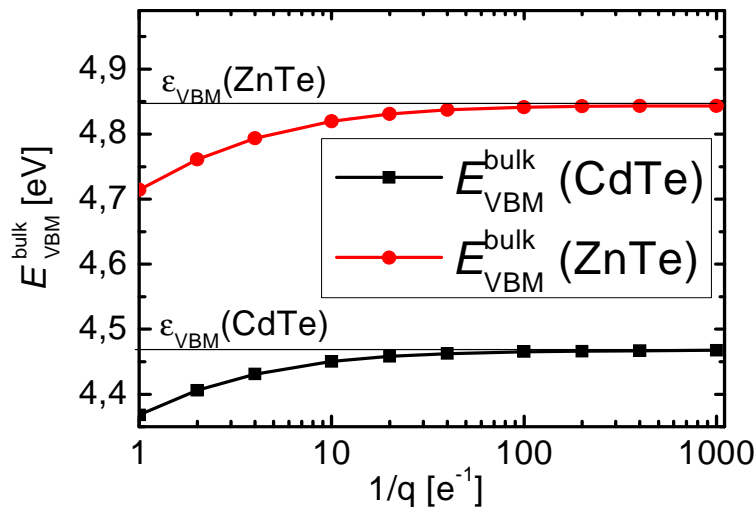


FIG. 1.1. Total energy difference $E_{\text{VBM}}^{\text{bulk}}$ per hole in eV between the neutral host material and the positively charged host material in CdTe and ZnTe. Increasing $1/q$ corresponds to a more dilute hole concentration.

1.2.1.3 Potential alignment correction of VBM

When dealing with charged defects, a compensating uniform background has been assumed [20]. The top of the valence band in the ideal supercell, $E_{\text{VBM}}^{\text{bulk}}$, and in the supercell with a (charged) defect differ by the electrostatic potential ΔV for reasons described in Sec. 1.2.1.2. The alignment of ΔV was obtained following Ref. 18, i.e., using 2 methods. First, by comparing the potential at two reference points far from the defect in the respective supercells with $V[A^{\varrho}]$ and without $V[0]$ the defect. Second, by comparing LDOS of atoms far from the defect. In particular, consideration of energies of strongly localized $d(\text{Zn})$, $d(\text{Cd})$, and $s(\text{Te})$ states giving sharp peaks was employed. Both methods give the same alignment to within 0.05 eV. This correction term has been evaluated for neutral defects, and used for charged states using the following formula:

$$\Delta E_{\text{form}}^{\text{pac}} = Q \cdot (V[A^{\varrho}] - V[0]) \quad (1.6)$$

1.2.1.4 Image charge correction

Makov and Payne [21] (M-P) have shown that because of electrostatic interaction between the periodically spaced charged defects, total energy converges as $1/\epsilon L$ as a function of the supercell size, where L is the linear dimension of the supercell and ϵ is the static dielectric constant. To compensate this effect a correction term $\Delta E_{\text{form}}^{\text{M-P}}$ is added, which takes into account electrostatic energy of point charges in the compensating background. This term is given by the Madelung expression divided by dielectric constant of the host. Since the defect-induced charge density is not point-like, there is a quadrupole contribution to the electrostatic energy. Typically, the quadrupole term decreases the interaction energy by about 30 %, which is included. The image charge correction takes following form:

$$\Delta E_{\text{form}}^{\text{M-P}}[A^{\varrho}] = \frac{Q^2 \cdot \alpha_M}{2\epsilon V_c^{1/3}} + \frac{2\pi \cdot QS}{3\epsilon V_c} + O(V_c^{-5/2}) \quad (1.7)$$

Here, α_M is lattice dependent Madelung constant, which for cubic supercell is 1.76 [22], V_c is the volume of the cubic supercell, and S is the second radial moment of the aperiodic density.

The detailed value of the defect-defect interaction depends on the change of the total electron density Δn induced by a defect, which is not point-like. However, in general Δn is limited to a distance comparable to the distance to the nearest neighbors, i.e., the perturbation is localized [23]. The localization of Δn is stronger than the localization of individual defect states, which may extend over several unit cells. However, the M-P corrections are expected to be larger for interstitials (inducing deep and localized states) than for vacancies (which levels are close to VBM and more delocalized). In any case, we stress that the used values, $\Delta E_{\text{form}}^{\text{M-P}} [A^{Q=1}] = 0.11$ eV for CdTe and 0.13 eV for ZnTe, are the upper limit for vacancies.

1.2.1.5 Band filling correction

Because of relatively small supercell sizes corresponding to the high defect densities, the defect concentrations computed in supercell approach are of the order of 10^{22} cm⁻³. This high doping concentration gives rise to the unwanted impurity bands instead of a single defect eigenstate. The defect electrons (for donors) and hole (for acceptors) populate states with energies higher (for donors) and lower (for acceptors) than that characteristic of the defect energy in the dilute limit (Fig. 1.2). Thus there is a need to correct the total energy, and also consequently E_{form} to this Moss-Burstein type band filling and band dispersion effects. It can be done by subtracting energy difference of the higher energy populations and the lowest (highest) populated donor (acceptor) level [18]:

$$\Delta E_{\text{form}}^{\text{bf}} = - \sum_{j \in \text{BZ}} (w_k \cdot \eta_{jk} \cdot \epsilon_{jk} - \epsilon_{\text{min}}) \quad \text{for donors} \quad (1.8a)$$

$$\Delta E_{\text{form}}^{\text{bf}} = - \sum_{j \in \text{BZ}} (w_k \cdot \eta_{jk} \cdot \epsilon_{jk} - \epsilon_{\text{max}}) \quad \text{for acceptors.} \quad (1.8b)$$

Here, ϵ_{jk} is the single particle eigenstate of the defect electron (hole). ϵ_{min} (ϵ_{max}) is the lowest (highest) populated defect state, usually for shallow defects located at the Γ -point. The mesh of k-space determines the weights w_k of the k-points, and from the tetrahedral k-space integration [24] the weights η_{jk} of the electron population are obtained. Obviously, if one aims to calculate the defects properties of highly doped semiconductors, the band filling correction is zero.

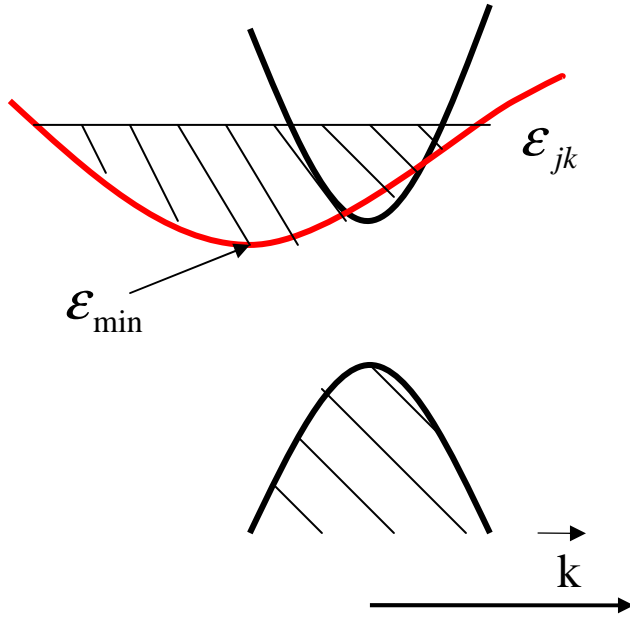


FIG. 1.2. Schematic figure showing the band-filling correction problem in GGA finite supercell calculations. The case of shallow donor is illustrated. Due to impurity band, except ϵ_{\min} depicting energy of the lowest populated shallow donor level, usually for Γ point, there are other contributions to total energy, ϵ_{jk} , calculated for other k -points. ϵ_{jk} is higher in energy than ϵ_{\min} , thus the total energy without correction is enlarged in comparison with total energy of shallow donor in the dilute limit.

1.2.1.6 Band gap correction

The results of the GGA calculations of defect properties are often corrected to account for the underestimation of the gap. In fact, DFT relates the ground state energy of an arbitrary system, e.g., a crystal with or without native defects, with its electron density calculated using the K-S equations. The one-electron K-S states are identified with the actual one-electron states. Solution of the K-S equation requires the knowledge of the exchange and correlation potentials, and typically LDA or GGA is assumed. However, the GGA/LDA K-S eigenenergies underestimate band gaps of insulators, which may be interpreted as a result of the fact that DFT does not describe properly excited states of a system. More accurate band gap energies are obtained within the GW approximation [25], which shows that the errors mainly arise from the underestimation of the energies of conduction states. The underestimation may also occur in the case of deep defect-induced levels in the band gap, which leads to a question about the accuracy of both the energies of the defect-induced levels and of their formation energies obtained within LDA/GGA. An empirical procedure to correct the LDA/GGA gap errors consists in shifting the energies of defect states, and then to

accordingly modify formation energies. More precisely, after finding the underestimation of the gap relative to the experimental value, $\Delta E_{\text{gap}} = E_{\text{gap}}^{\text{exp}} - E_{\text{gap}}^{\text{GGA}}$, the GGA defect levels $\mathcal{E}_{\text{defect}}^{\text{GGA}}$ are shifted upwards. One may assume the shift to be proportional to the contribution of the conduction states to the defect level. This contribution in turn may be assumed to be proportional to the energy of the level relative to the conduction bands, i.e., the corrected defect energy $\mathcal{E}_{\text{defect}}^{\text{corrected}}$ is rescaled by the correction of the band gap, and is given by $\mathcal{E}_{\text{defect}}^{\text{corrected}} = \mathcal{E}_{\text{defect}}^{\text{GGA}} (E_{\text{gap}}^{\text{exp}} / E_{\text{gap}}^{\text{GGA}})$. Thus, the levels close to the top of the valence band are almost non-shifted, while the levels close to the conduction band are shifted by about ΔE_{gap} . Finally, formation energy of the defect is increased by $\mathcal{E}_{\text{defect}}^{\text{corrected}} - \mathcal{E}_{\text{defect}}^{\text{GGA}}$ times the number of electrons that occupy the gap state. This approach is empirical. In particular, considering the energy corrections, energies of shallow effective-mass donors, which wave functions are built up from the states close to the minimum of the conduction band, are expected to shift by the same amount as the bottom of the conduction band itself. Corrections of the deep levels are less straightforward, since their wave functions are derived from various bands and various points of the Brillouin Zone. For example, the wave functions of the interstitials are considered to have a non-bonding character, and thus the contribution of the conduction states should not be dominant.

A better justified scheme improving some of the LDA/GGA deficiencies is the LDA+ U approach, which provides a better description of correlation effects important in the case of localized d orbitals. In particular, the LDA energies of $d(\text{Zn})$ are too high, thus the coupling between $d(\text{Zn})$ and the top of the valence band is overestimated, which results in an overestimation of its upward shift. This effect is important in ZnO [26], where the energy of $d(\text{Zn})$ is close to the VBM, and the LDA energy of the VBM is overestimated by 0.8 eV [27]. On the other hand, the energy of $d(\text{Zn})$ in ZnTe is lower, and the overestimation is 0.2 eV only [27]. A similar overestimation is expected for CdTe, since according to our results both $d(\text{Zn})$ in ZnTe and $d(\text{Cd})$ in CdTe are ~ 7 eV below the VBM. Finally, even in ZnO the differences in LDA and LDA+ U formation energies are about 0.3 eV [26], and the LDA gap corrections lead to much larger changes of formation energies. Consequently, I neglect the LDA+ U corrections. The band gap correction procedure is discussed also in detail in Sec. 2.2.

1.2.1.7 Finite-size effects

Supercell approximation, in line with band-edge corrections due to the approximate DFT functional (Sec. 1.2.1.6), introduces errors to the calculated properties of isolated defects. The image charge (Sec. 1.2.1.4) and band filling (Sec. 1.2.1.5) corrections are the most significant measures to improve the quality of results. The efficacy of the above corrections is illustrated in Fig. 1.3 for Cd_i in CdTe.

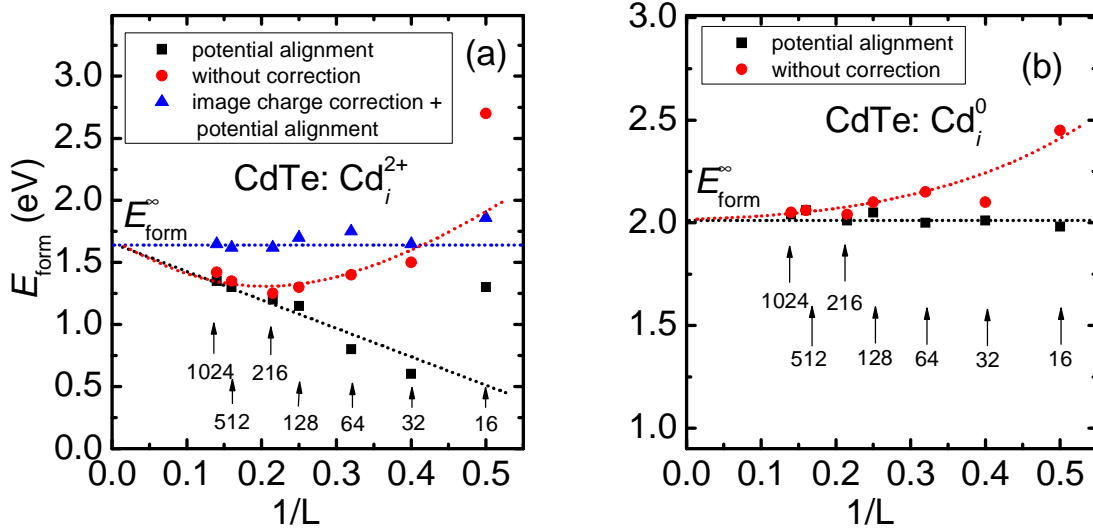


FIG. 1.3. Scaling of formation energy of Cd_i in CdTe as a function of the reciprocal linear supercell dimension $1/L$. Various supercell sizes, varying from 16 to 1024 atoms, were employed to construct the figure. The effect of different corrections on scaling is presented. In the case of (a) Cd_i^{2+} no size dependence is achieved after both image charge and potential alignment correction (blue diamond). $1/L + 1/L^3$ scaling is obtained using no corrections (red circles). Bare potential alignment gives $1/L$ scaling (black squares). Employing only potential alignment correction is enough to obtain elimination of finite-size effects for (b) Cd_i^0 . E_{form}^∞ depicts the theoretical formation energy of infinitely large supercell with a defect, which corresponds to $1/L = 0$, thus the formation energy of a perfectly isolated defect.

The general conclusions are as follows. In order to adopt correct methodology each defect has to be considered separately, using several supercell sizes. The corrections are performed properly when E_{form} is size independent. Potential alignment correction has to be implemented in each case. Image charge correction is important for charged states of deep defects. It has to be also implemented for the neutral charge state of shallow defects that exhibit dependence of E_{form} on the size of supercell (see for example zinc interstitial in ZnO [28]). Finally, it has been very recently shown [29] that explicit expression for the L^{-3} term can be derived and

implemented efficiently in existing codes. This novel approach requires no fitting procedures or empirical parameters and is expected to be adopted widely in the immediate future.

1.2.2 Transition energy levels

Transition energy level of a defect, $\varepsilon(Q/Q')$, is the Fermi energy at which the formation energies of the charge states Q and Q' are equal. These levels are observed in experiments such as deep level transient spectroscopy, where in the final state the defect relaxes to its equilibrium configuration. In optical experiments, optical transitions are much faster than lattice relaxation to equilibrium. Accordingly, the transition energy between the charge states Q and Q' , $\varepsilon^{\text{opt}}(Q/Q')$ is obtained when in the final state Q' the atomic configuration is that of the initial state Q . Atomic relaxations of the final state give Franck-Condon shifts. Finally, in principle free energy should be used in Eq. (1.1), but in general contributions of vibrational entropy are small and do not affect qualitative conclusions [18]. Summarizing, all factors considered, the errors in the calculated formation energies and energy levels are estimated to about 0.2 eV and 0.1 eV, respectively. The errors can be larger for very localized defects in high charge states [18, 30].

1.3 Minimal energy path of rare events

Computational methods that enable the study of complex systems, whose dynamics is driven by rare events, base on the correct identification of transition states. In the simplest case the transition states, which manifest bottleneck of a given reaction, can be encapsulated in a saddle point that separates two stable states represented by two minima. The saddle point has potential energy higher than those corresponding to minima, which represent the energy barrier that has to be surmounted to realize a given rare event. The transition rate of the rare event can be estimated by harmonic transition state theory, and the probability is proportional to $\exp(-E_{\text{barrier}}/kT)$. This approach is substantiated only if potential energy surface (PES) of the system is smooth enough, and the temperature is low enough to ensure entropic effects to be described within harmonic approximation. The most daunting problem is usually to identify correctly the saddle points. Methods based on the first derivative of PES (i.e., forces) are not convergent to the unstable stationary points. Nevertheless, despite local convergence to stationary points, approaches dependent on the second derivatives of PES (i.e., Hessian matrix) are not practical within first principles calculations (due to difficulty of the evaluation

of second derivatives in this computational framework). The breakthrough was to propose by Elber and Karplus [31] to search for the saddle point by investigating a path connecting the initial point with the final one, instead of searching transition point starting from the initial state. The approach is very innovating since it focuses on the global property of the path rather than on the local properties of the PES like it was before Elber and Karplus paper. Nudged Elastic Method (NEB) [32] is the extension of this approach. Minimum Energy Path (MEP), joining stable points in the configuration space, is defined by its property to zeroing the orthogonal component forces to it. In effect, because vector force is always parallel to MEP's tangent, finding MEP guarantees finding a path that crosses the saddle point. The saddle point is then the configuration with the highest energy on this path. If the temperature is considerably lower than characteristic barrier energy one can show within stochastic dynamics (i.e., the evolution of the system can be described by a first order Langevin equation) that MEP represents the most probable path connecting two minima of PES. NEB proves to be much more efficient and more accurate than methods based on the harmonic approximation, and gives reasonable results also in the regime when kinetics is dominated by entropic effects.

The satisfactory results can be also obtained using string method [34], that also develops further the approach of Elber and Karplus.

If the energy potential is rugged and there are a lot of stationary points, a number of MEPs is allowed, and the concept of saddle point in the PES is not valid any more. The assumptions of transition state theory are not operative, and sometimes only one dynamical trajectory is known. In this case, simulated annealing in the space of reactive trajectories [35] or identification of dynamical trajectory based on the Hamilton's least action principle [36] can be applied. Finally, if the knowledge of initial and final state of investigated reaction is missing, one can employ coarse-grained molecular dynamics approach (called metadynamics) [37] that explore free energy surface landscape.

1.3.1 NEB methods

MEP, x , is the path connecting reactants and products, or minima, that has the property of vanishing components of the force perpendicular to the path:

$$\nabla V[x(t)] - \tau(t) \cdot \langle \tau(t), \nabla V[x(t)] \rangle = 0. \quad (1.9a)$$

Here, $\tau(t)$ is the normalized tangent vector, and V is the potential energy of the system. The PES is a function of x and describes how V changes as the nuclei move relative to each other. The potential energy in Eq. (1.9a) is stationary on each hyperplane perpendicular to MEP. MEP is parametrized by the arbitrary reaction coordinate, $t \in [0,1]$. In this notation $x(0)$ depicts the initial state, and $x(1)$ is the final state. Solving Eq. (1.9a) numerically enables the identification of MEP and the saddle point. The continuous path $x(t)$ is discretized into so called images, signified by x_i , and Eq. (1.9a) turns into:

$$\nabla V[x_i] - \tau_i \cdot \langle \tau_i, \nabla V[x_i] \rangle = 0. \quad (1.9b)$$

For each image, all Eqs. (1.9b) are solved when the energy is minimized on the hyperplane perpendicular to the discretized path. Such a minimization can be achieved iteratively using steepest-descent dynamics in the space of paths [37]. The computation starts with the initial path of equidistant images, which evolve by fictitious dynamics according to the projected force:

$$F[x_i]_{\perp} = -\{\nabla V[x_i] - \tau_i \cdot \langle \tau_i, \nabla V[x_i] \rangle\} \quad (1.10a)$$

$$x_i(s + ds) = x_i(s) + ds \cdot F[x_i(s)] \quad (1.10b)$$

The procedure is continued (i.e., the path converges to MEP) until $F[x_i]_{\perp} = 0$ for all images x_i . The disadvantage of this direct approach, especially when small number of images is used, is that the images tend to slide down as the iteration procedure ensues. This is due to limited accuracy of the path, imperfect estimation of the tangent, and additional influencing of the parallel component of the force on the path. As the sliding occurs, the further lost of accuracy is experienced. If this tendency is not counterbalanced, all images can eventually collapse into two minima. Thus, proper strategy to discretize the path and judicious constraints imposed on the parametrization influencing evolution of inter-image distance are of great significance if one wants to solve correctly Eqs. (1.10). A number of strategies were devised to address above numerical challenges (to get familiarized with the most famous see Ref 37):

(i) **NEB** [32]. Path parametrization is realized by introducing virtual force (which manifests itself in connecting of images by zero-length virtual string), in addition to the true projected force stemming from external potential. In effect, the discretized path is described by elastic

band. The disadvantage is that when the evolving path bends, there is artificial, undesired addition to the orthogonal component, which can prevent correct convergence of the path to MEP. To reduce this effect, the elastic forces are projected (which is called *nudging*) onto path's tangent. Then the effect of the elastic forces is decoupled from the external forces. As a result, the virtual springs act like a penalty function. Because, all elastic constants are equal, the configuration with equidistant images is the one that converges to MEP.

(ii) **Climbing-image NEB** [33]. This procedure is an improvement to NEB. The maximum energy image is free (i.e., is not affected by spring forces) to move up-hill along the path's tangent and simultaneously down-hill along all directions perpendicular to the path's tangent. Other images are utilized as a degree of freedom for this optimization. The procedure is very computationally effective and swiftly converges.

The Climbing-NEB method was used to calculate minimum energy pathways and energy barriers for both the defects diffusion, generation, and recombination of FPs. Five (for interstitials) and seven (for FPs) intermediate configurations (replicas) were chosen between the two stable configurations. The computations were done with the convergent parameters given in Sec. 1.1. The forces in each image were computed with stop criterion fixed at 0.026 eV/Å. Due to the optimization with the DIIS algorithm [38] applied to the image with the highest energy, the errors on barriers at saddle points are similar to those at the stable states.

Chapter 2

Native defects in CdTe and ZnTe

In this Chapter vacancies and interstitials in bulk CdTe and ZnTe are investigated in great detail. Both cation- and anion-originating defects are considered. Both electronic structure and diffusion are examined. Special treatment is given to the analysis of the formation energies, the influence of relaxation, electronic levels, and the compensation ensued from the defects under study.

2.1 Cation vacancies

Formation of a vacancy implies a formation of four dangling bonds of the four neighbors. In a zinc-blende host, their linear and symmetries combinations result in a singlet a_1 , and a triplet t_2 that is located higher in energy. Their energies relative to the top of VBM depend on the host. These four orbitals may accommodate up to eight electrons. Because each Te bond is occupied with $6/4$ electrons, the levels of a neutral cation vacancy are occupied with $4 \cdot (6/4) = 6$ electrons. Two of them are located on the a_1 singlet, and the remaining four on the t_2 triplet. Thus, a neutral cation vacancy in II-VI compounds has two empty states on t_2 , and is a double acceptor. The fact that the states induced by both V_{Cd} and V_{Zn} are formed by Te dangling bonds explains the similarities between the two defects that are discussed below. Next, since vacancy states are derived mostly from the valence states, energies of vacancy levels relative to the top of the valence band are determined accurately in spite of substantial

bandgap errors typical for GGA. In both CdTe and ZnTe, the a_1 singlet is resonant with the valence band and is located at about 3.3 eV below the top of the valence bands. The t_2 triplet is at about 0.1 eV above the VBM in both crystals (Fig. 2.1). Because of the fact that the t_2 is close to the VBM, it is delocalized in real space and wave function is not localized only around vacancy region (Fig. 2.2). Both differences in total density of states between defect supercell and ideal supercell, and wave function square of cation vacancy t_2 state, $|\psi|^2$, are qualitatively very similar in ZnTe. The energies of t_2 are listed in Tables I and II. They depend on the charge of the defects. The energy of t_2 increases with the growing number of electrons occupying this state, which stems from the increasing electron-electron repulsion.

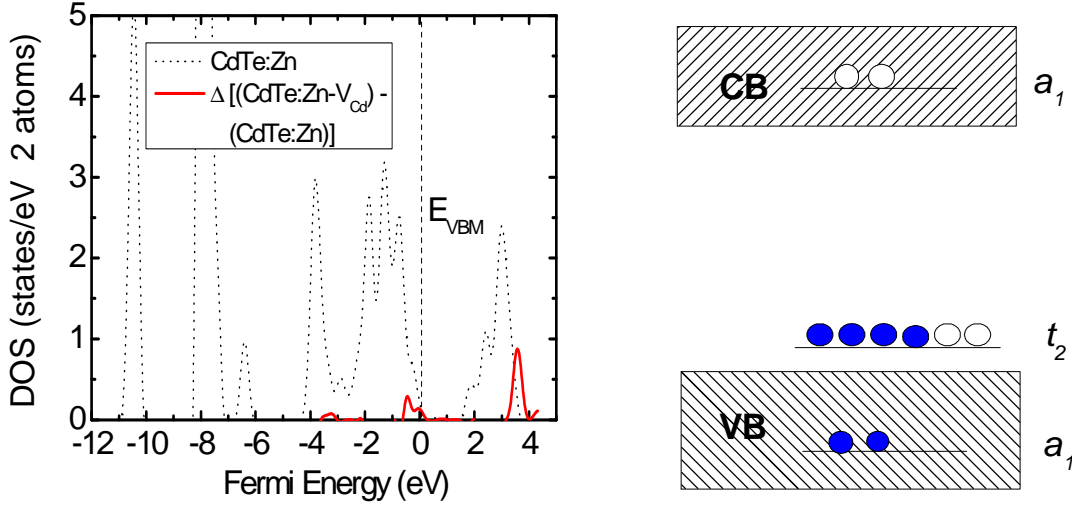


FIG. 2.1. Calculated density of states for CdTe with substitutional Zn, CdTe:Zn, and density of states' difference between CdTe:Zn with cation vacancy, CdTe:Zn- V_{Cd} , and CdTe:Zn without the defect. The energy alignment is implemented (see Chapter 1). The left diagram represents single particle energy states for the tetrahedrally coordinated neutral V_{Cd} in CdTe.

TABLE I. Energies of the vacancy-induced triplet state t_2 , changes of distances to the first (Δd_1) and second (Δd_2) neighbor, and total energy gains due to relaxation ΔE_{relax} for the neutral and charged states of V_{Cd} in CdTe. Δd is defined as the difference between the relaxed and unrelaxed bond length relative to the unrelaxed bond. Negative Δd means inward relaxation.

	V_{Cd}^0	V_{Cd}^-	V_{Cd}^{--}
t_2 (eV)	0.04	0.05	0.08
Δd_1 (%)	-7.96	-7.64	-8.70

Δd_2 (%)	-1.86	-1.85	-2.31
ΔE_{relax} (eV)	0.23	0.30	0.47

TABLE II. Energies of the vacancy-induced triplet state t_2 , changes of distances to the first (Δd_1) and second (Δd_2) neighbor, and total energy gains due to relaxation ΔE_{relax} for neutral and charged states of V_{Cd} in ZnTe.

	V_{Zn}^0	V_{Zn}^-	V_{Zn}^{--}
t_2 (eV)	0.05	0.07	0.10
Δd_1 (%)	-4.87	-4.88	-5.51
Δd_2 (%)	-1.31	-1.47	-1.65
ΔE_{relax} (eV)	0.11	0.23	0.41

Figure 2.3 presents the calculated formation energies of Cd vacancy V_{Cd} in CdTe as a function of the Fermi energy for both Cd-rich and Te rich conditions. Only line segments that correspond to the charge state with the lowest energy are shown. Thus, the slope of the line reflects the charge state of the defect at a particular E_{F} , and the change in the slope corresponds to the change in the charge state and determines the transition energy level. Throughout the available values of E_{F} , cation vacancy can assume one of the three charge states, which range from the neutral one in p-type samples to 2- in n-type samples. As it follows from Fig. 2.3, the calculated transition energy levels from the neutral to the singly charged state V_{Cd}^- is $\epsilon_{\text{Vcd}}(0/-) = 0.1$ eV and to 2- state V_{Cd}^{--} $\epsilon_{\text{Vcd}}(-/--) = 0.25$ eV. Next, formation of V_{Cd} is easier in the Te-rich limit than in the Cd-rich limit since the formation energy is lower by 0.95 eV, i.e., by the calculated values of $\Delta H_f(\text{CdTe})$ (see Chapter 1). Finally, the very low values of E_{form} for high Fermi energies indicate that cation vacancies act as compensating acceptors, as it will be discussed in more details below. The obtained results agree to within 0.1 eV with those of Ref. 39.

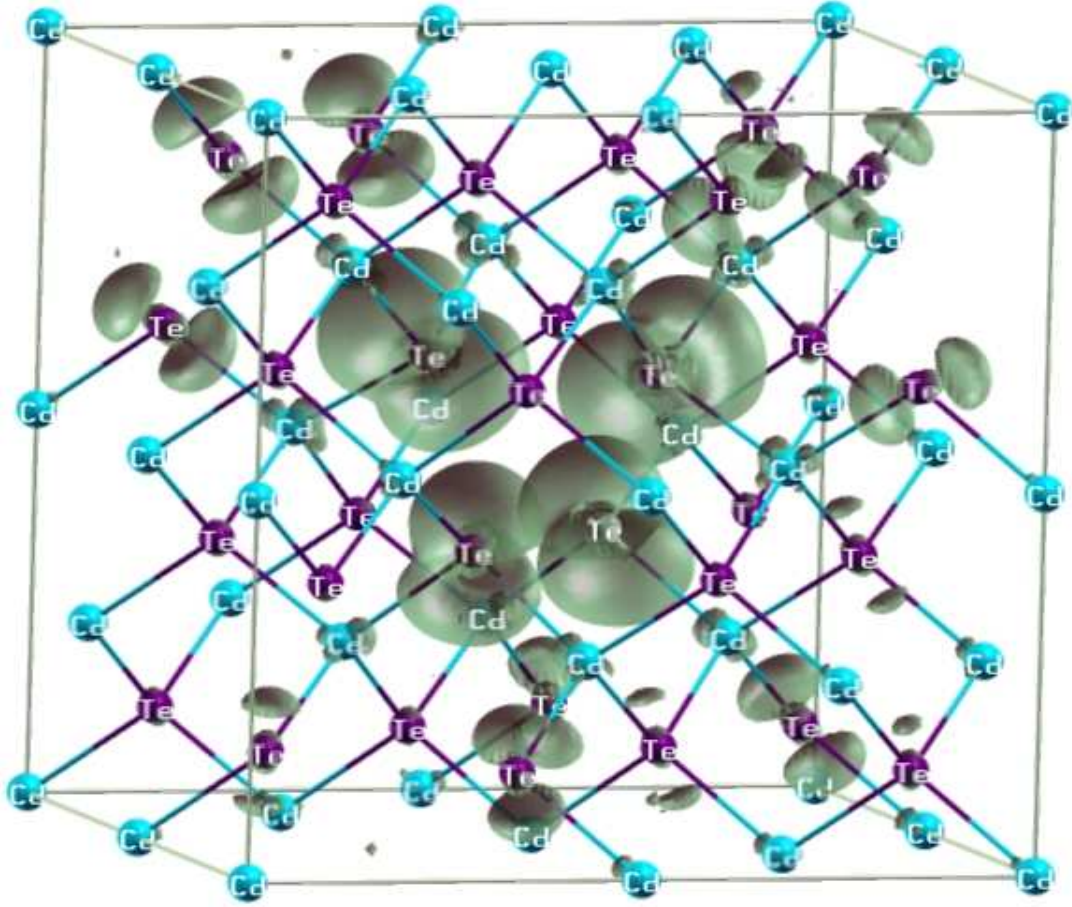


FIG. 2.2. Wave function square of the cation vacancy t_2 state in CdTe.

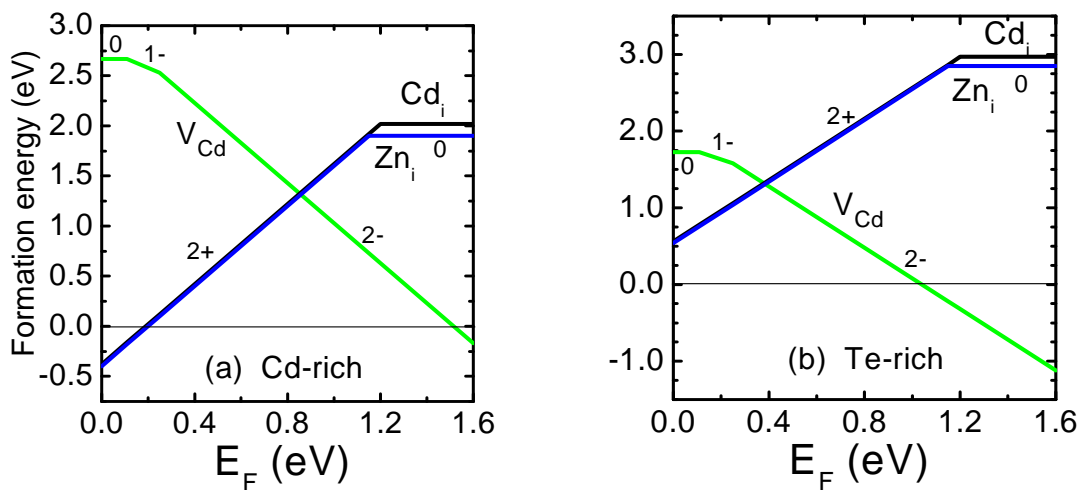


FIG. 2.3. Calculated formation energies of V_{Cd} , Cd_i and Zn_i in CdTe as a function of the Fermi energy in the (a) Cd-rich and (b) Te-rich limit. The transition energy levels correspond to the values of E_F at which the slope changes.

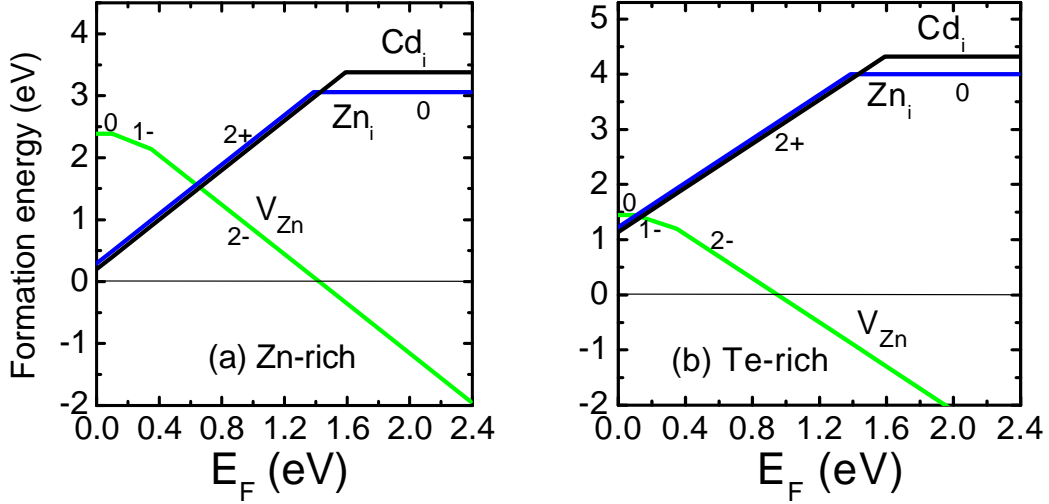


FIG. 2.4. Calculated formation energies of V_{Zn} , Cd_i and Zn_i in ZnTe as a function of the Fermi energy in the (a) Zn-rich, and (b) Te-rich limit.

The formation energies of the V_{Zn} in ZnTe are shown in Fig. 2.4. The transition levels $\varepsilon_{V_{\text{Zn}}}(0/-)$ and $\varepsilon_{V_{\text{Zn}}}(-/--)$ are 0.06 and 0.36 eV, respectively. Comparing the results for CdTe with ZnTe, one may see that for given growth conditions (i.e., cation-rich or Te-rich), the formation energy of V_{Zn}^0 in ZnTe is lower than that of V_{Cd}^0 in CdTe by 0.28 eV. According to Eq. (1.1), this result may be due to (a) the lower value of energy necessary to extract a Zn atom from the crystal, given by $E_{\text{tot}}[V_{\text{Zn}}] - E_{\text{tot}}[\text{ZnTe}]$, or to (b) the lower cohesive energy $\mu_{\text{Zn}}^{\text{solid}}$ compared to $\mu_{\text{Cd}}^{\text{solid}}$. The first contribution favors the formation of V_{Cd} in CdTe. This stems from the fact that ZnTe is less ionic than CdTe, and, as a rule, more covalent compounds are characterized by stronger bonds. However, this factor is overcompensated by the fact that the cohesive energy of solid Zn, -1.13 eV, is higher than that of solid Cd, -0.76 eV. Thus, ultimately, this is the higher stability of solid Zn that favors the formation of V_{Zn} over V_{Cd} .

A comparison of the results from Tables I and II shows that the relaxation of atoms neighboring the vacancy depends on its charge state, and the relaxation effects are stronger in CdTe than in ZnTe. The four nearest-neighbor Te atoms and twelve second-neighbor cations surrounding a vacancy relax symmetrically toward the center. The contraction of the distances and relaxation energy are the highest for doubly charged centers (Tables I and II), when the triplet is fully occupied with six electrons. In the case of V_{Zn} , both the changes in the bond lengths and relaxation energy are smaller than in the case of V_{Cd} since the radius of a Zn atom

is smaller than that of Cd and the stiffness of ZnTe is greater (the calculated bulk modulus of ZnTe, 43 GPa, is larger than that of CdTe, 36 GPa).

In the case of neutral and singly charged vacancies, a partial occupation of the t_2 level can lead to the Jahn-Teller distortion. However, the obtained results show that the T_d symmetry of the cation vacancies in both CdTe and ZnTe is maintained. Stability has been verified by imposing appropriate atomic distortions with either C_{3v} or D_{2d} symmetry. For the trigonal distortion, a Te atom is displaced along the [111] direction away from the center, while the other Te atoms are moved toward the center. Tetragonal distortion was imposed by moving along the [110] direction two Te atoms at (1,1,1) and (-1,-1,1) sites toward each other, and simultaneously moving closer Te atoms at (1,-1,-1) and (-1,1,-1) sites along the [1-10] direction. In both cases, the T_d symmetry is found to be more stable than the distorted one. The same result was obtained in Ref. 40. However, the relatively small supercell (64 atom) used here may be not sufficient to assess the exact geometry of an isolated vacancy, see Ref. 41.

The calculated optical levels for CdTe are $\epsilon_{V_{Cd}}^{opt}(0/-) = 0.16$ eV, $\epsilon_{V_{Cd}}^{opt}(0/--) = 0.16$ eV and $\epsilon_{V_{Cd}}^{opt}(-/--) = 0.17$ eV. The corresponding Franck-Condon shifts are 0.002 eV, 0.031 eV and 0.017 eV. For ZnTe we find $\epsilon_{V_{Zn}}^{opt}(0/-) = 0.06$ eV, $\epsilon_{V_{Zn}}^{opt}(0/--) = 0.18$ eV, and $\epsilon_{V_{Zn}}^{opt}(-/--) = 0.34$ eV with the Franck-Condon shifts of 0.005, 0.063, and 0.016 eV. Thus, optical processes entail more relaxation in ZnTe, in spite of the fact that Zn vacancy induces less surrounding relaxation than V_{Cd} in CdTe.

2.1.1 Diffusion of cation vacancies

Several mechanisms of the diffusion of cation vacancies were investigated [42, 43] (Fig. 2.5). The feasibility and efficiency of the relevant diffusion mechanism are investigated below.

2.1.1.1 Diffusion to the first neighbor

Diffusion to the first neighbor entails the diffusion of the first neighbor of the vacancy, i.e., Te^{1st} , along the [111] direction. This is realized by the displacement of Te^{1st} toward the vacant site via a split vacancy configuration during which one bond of the Te^{1st} atom is

initially stretched (namely the $\text{Te}^{1\text{st}}\text{-Cd}^{2\text{nd}}$ bond), and finally broken. The process bears a close resemblance to the diffusion of a neutral silicon vacancy in Si [44]. In the case of V_{Ga} in GaAs the diffusion to the first neighbor is possible, charge dependent, and efficient for all charge states except V_{Ga}^{3-} [43], and results in metastable antisite –vacancy pair, $\text{As}_{\text{Ga}}+V_{\text{As}}^{1\text{st}}$. This means that it is possible to transform V_{Ga} into the defect pair by the mechanism of the first neighbor diffusion. In the case of both V_{Cd} in CdTe, and V_{Zn} in ZnTe, in all accessible charge states, this mechanism is not operative. $\text{Te}_{\text{Cd}}+V_{\text{Te}}^{1\text{st}}$ and $\text{Te}_{\text{Zn}}+V_{\text{Te}}^{1\text{st}}$ defect pairs are unstable with respect to the cation vacancy, since Te_{Cd} and Te_{Zn} antisite atoms spontaneously relax into the original substitutional position, $\text{Te}^{1\text{st}}$.

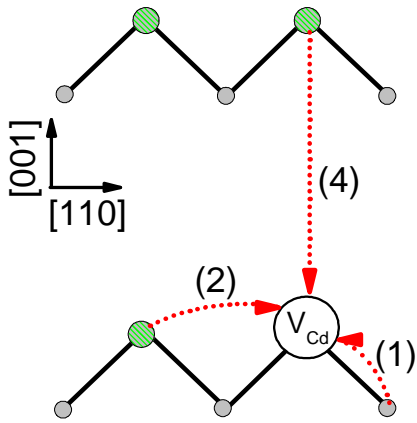


FIG. 2.5. Schematic representation of diffusion mechanisms of V_{Cd} in the (110) plane of zinc blende in CdTe. The large green circles represent Cd atoms, medium grey circles Te atoms. (1), (2), and (4) arrows represent diffusion to the first, second, and fourth neighbor, respectively. (2) trajectory is out of the plane.

2.1.1.2 Diffusion to the second neighbor

Diffusion to the second neighbor involves at first breaking the $\text{Cd}^{2\text{nd}}\text{-Te}^{3\text{rd}}$ bond, i.e., displacing the $\text{Cd}^{2\text{nd}}$ atom along the [111] direction toward the interstitial region. During subsequent displacement, the diffusing atom passes through the diffusion plane perpendicular to the [110] direction causing three $\text{Te}^{1\text{st}}$ atoms move away from the surrounding vacancy, and opening the cage which facilitates the successful diffusion (hence the name – *plane-passing* mechanism [42, 43]). The diffusing atom undergoes curvilinear motion which is presented in Figs. 2.5 and 2.6. It is the case also of the migration to the second neighbor for both V_{Cd} in

CdTe and V_{Zn} in ZnTe. The mechanism is operative in all accessible charge states (Table III). The heights of diffusion barriers show a tendency to be slightly higher for higher charged states. The increase is relatively small, but evident in both CdTe and ZnTe.

TABLE III. Calculated diffusion barriers (in eV) for different diffusion mechanism and charged states of V_{Cd} in CdTe and V_{Zn} in ZnTe.

	CdTe			ZnTe		
	V_{Cd}^0	V_{Cd}^{1-}	V_{Cd}^{2-}	V_{Zn}^0	V_{Zn}^{1-}	V_{Zn}^{2-}
First neighbor	-	-	-	-	-	-
Plane passing	1.00	1.05	1.10	1.25	1.30	1.35
Cluster assisted	1.70	1.80	1.90	2.20	2.30	2.35
Fourth neighbor	2.60	2.70	2.75	3.40	3.45	3.50

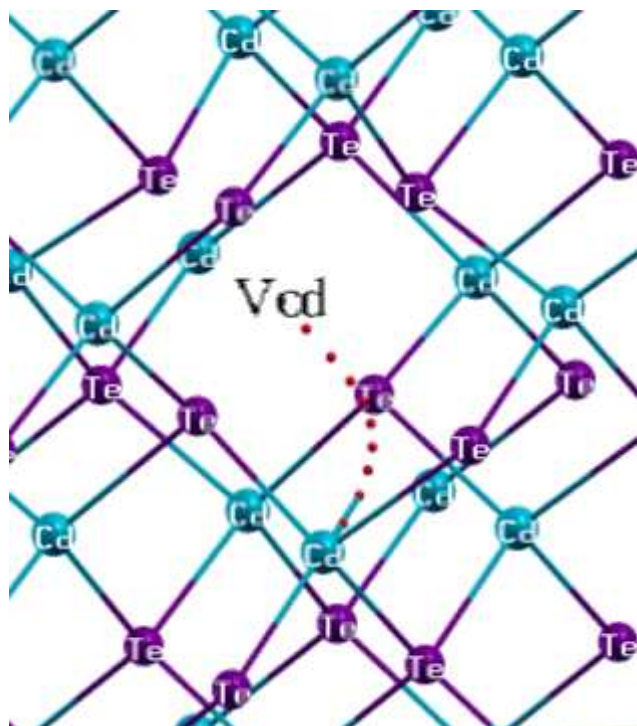


FIG. 2.6. Migration path of V_{Cd} in CdTe to the second neighbor by plane passing mechanism.

I found based on the charge density plots and the Milliken populations that the electrons added to the neutral vacancy are delocalized and distributed themselves on the direction parallel to the [111] direction in all studied charge states. Less than 10 % of the charge is located on the four Te^{1st} with the remaining 90 % spread over more distant neighbors (Figs. 2.7a and b). This suggests that Te-Cd and Te-Zn bonds are somehow stiffened upon the addition of extra electrons. Extra electrons localized in a given direction are tantamount to the statement that it is more difficult to break the bond in this direction. Obviously, if extra electron density is localized in the region of barrier, this would translate also into the increase of the height of the diffusion barriers. I found that the barriers are only slightly enhanced when additional electrons are added (Table III). The additional charge distribution overlaps the trace of displacement to the limited degree and the amount is small. The deficit regions which lose charge density when the defect is ionized, and if matched to the trajectory region would weaken the bond structure, are predicted to decrease the heights of the diffusion barriers provided they intersect these regions, and consequently facilitate the diffusion. Nevertheless, the deficit regions are negligible upon addition of extra electrons (their spatially corresponding isosurfaces are order of magnitude lower in value than the surplus regions depicted above and presented in Fig. 2.7), and their impact can be excluded here.

Moreover, the heights of diffusion barriers are higher for ZnTe than for CdTe because of the higher stiffness and bulk modulus of the former as it was underscored in Sec. 2.1.

The *cluster-assisted* mechanism first analyzed in Ref. 43 was also investigated. Instead of crossing the [110] diffusion plane, the Cd^{2nd} atom goes into the interstitial region with the assistance of three atoms, Te^{1st}, Te^{3rd}, and Cd^{3rd} or Zn^{3rd} depending whether the diffusion takes place in CdTe or ZnTe. From the initial to the transition state (i.e., saddle point), Cd^{2nd} and Te^{3rd} experience incomplete bond exchange mechanism of Wooten-Winer-Weaire type [45] which is also valid in Si. The cluster composed of the four aforementioned atoms is central to this mechanism, hence the name coined by El-Mellouhi and Mousseau [43]. Regardless of the charge state, the bond distances Cd^{2nd}-Te^{1st} and Cd^{2nd}-Te^{3rd} does not alter (2.75 and 2.57 Å for CdTe and ZnTe, respectively) while the V_{cation}^q -Cd^{2nd} distance increases when the number of electron rises. After passing the saddle point only Cd^{2nd} continues its displacement toward the vacancy, the other atoms forming the cluster remain their initial positions. It is characteristic of cluster-assisted mechanism that all cluster atoms undergo displacements from the initial to the transition point and remain unarranged after

passing saddle point with only interstitial $\text{Cd}^{2\text{nd}}$ experiencing displacement. This is in contrast to the plane-passing mechanism where from the initial to the final point in migration path all neighbors along with diffusing $\text{Cd}^{2\text{nd}}$ experience rearrangements and displacements. A similar microscopic behavior of atoms is found here for ZnTe. The most important result is that energy barrier for cluster-assisted mechanism is higher by about 0.7 eV than for plane-passing mechanism. Nevertheless, the mechanism is operative and can be important as the additional way of migration to the second neighbor by cation vacancies in CdTe and ZnTe, especially in higher temperature regimes.

Finally, comparing the obtained results with those for V_{Ga} in GaAs, one may note following:

- (i) In the case of V_{Ga} in GaAs the diffusion to the second neighbor is also charge dependent and the diffusion barrier increases as the defect is ionized [43]. The increases are more pronounced in the case of V_{Ga} in GaAs, and equals 0.3 eV while going from V_{Ga}^0 to V_{Ga}^{3-} [43].
- (ii) The distribution of additional charge is more localized in V_{Cd} or V_{Zn} than in the case of V_{Ga} in GaAs where 4% charge is located on the four $\text{As}^{1\text{st}}$ with the remaining 96 % spread over more distant neighbors. The delocalized additional charge was calculated to be distributed along the 111 axis [43]. I attribute the increase and the ratio discrepancies concerning localization of additional charge to the fact that the t_2 orbital in CdTe or ZnTe is higher with respect to the VBM than in GaAs, and thus is less genetically related to the valence band.
- (iii) Similarly as for V_{Cd} in CdTe the energy barrier for cluster-assisted mechanism of V_{Ga} in GaAs [43] is higher than that for plane-passing channel of diffusion. In CdTe and ZnTe the process is also allowed in neutral state which is excluded in the diffusion of V_{Ga} in GaAs [43], because of the higher softness of the materials compared to the stiffer GaAs.

2.1.1.3 Diffusion to the fourth neighbor

Diffusion to the fourth neighbor engages the displacement of the fourth neighbor of the vacancy, namely $\text{Cd}^{4\text{th}}$ and $\text{Zn}^{4\text{th}}$, along the [100] direction. Because during this displacement the diffusing atom is bound to break simultaneously two bonds with $\text{Te}^{5\text{th}}$ and twist the remaining $\text{Te}^{3\text{rd}}$ bonds, and obviously the breaking is not undergoing along the bond direction of any two fractured bonds, the energy required to accomplish this is much higher than in mechanisms described in (ii) (Table III). The barrier is attained when $\text{Cd}^{4\text{th}}$ or $\text{Zn}^{4\text{th}}$ is placed between two distant cation vacancies. The stabilization after passing this transition

point is facilitated by the formation of two bonds with $\text{Te}^{1\text{st}}$. The path of migration to the fourth neighbor is presented in Figs. 2.5 and 2.8.

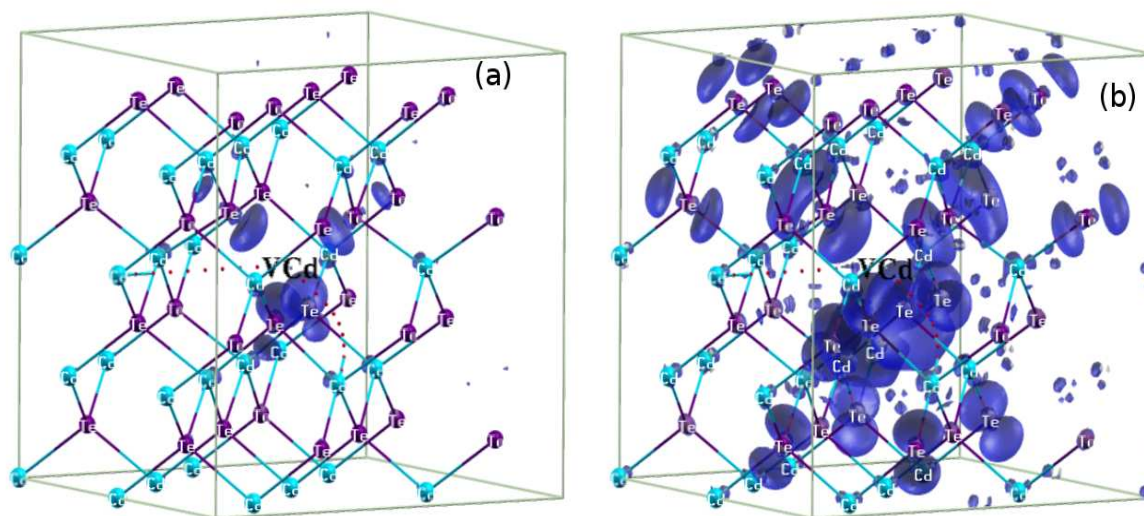


FIG 2.7. Isosurfaces at (a) 0.001, and (b) 0.0004 $\text{electron}/\text{\AA}^3$ of the difference in electronic charge density between the 2- charged and the neutral cation vacancy in CdTe. In the case of both neutral and 2- charged state the same atomic coordinates were employed. Note that the isosurface represents positive values, the complementary negative values that give comparable spatial volume are the order of magnitude lower.

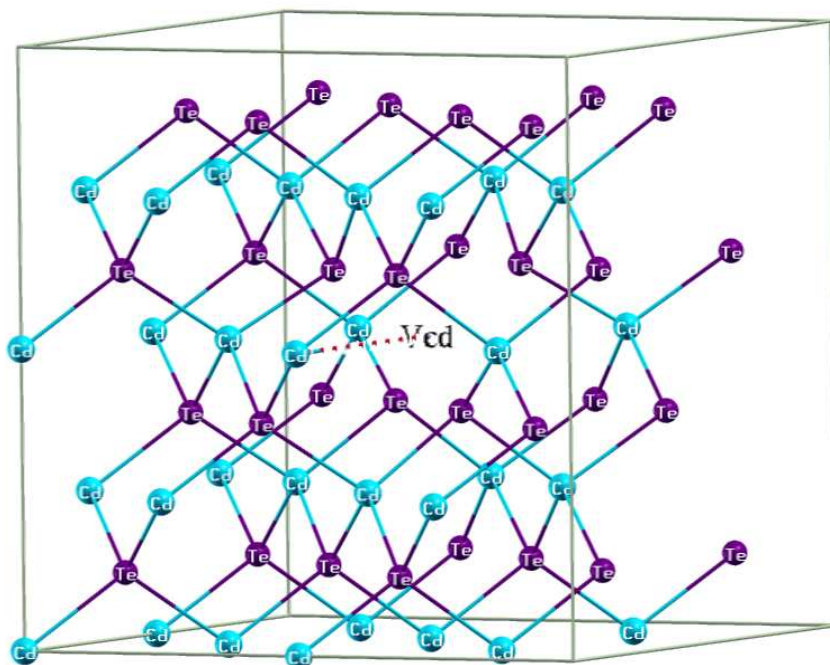


FIG 2.8. Migration path of V_{Cd} in CdTe to the fourth neighbor.

The dependence of the barrier on the charge state is small and comparable to the second neighbor because of still weak overlap of the extra electron region in the charged states with the trajectory of displaced atom (Fig. 2.7).

As it was pointed above the charge density coming from extra electrons in GaAs is more delocalized than in case of CdTe, with the topology of the wave vacancy function in GaAs and CdTe similar. In both CdTe and ZnTe the process is also allowed in the neutral state (in V_{Ga} in GaAs it is not active in neutral state [43]), because of the higher softness of the materials comparing to the stiffer GaAs.

To the best knowledge of the author the diffusion of vacancies in CdTe and ZnTe, both anion and cation, was not addressed prior to 2009.

2.2 Cation interstitials

In the zinc-blende structure there are two nonequivalent interstitial sites with the tetrahedral symmetry, the first of which is surrounded by four anions, T:anion, and the other by four cations, T:cation. They are shown in Fig. 2.9. In an ideal crystal, the distance from these sites to the nearest neighbors is equal to the bond length of the host. The location in the middle between T:cation and T:anion is denoted as H. The results obtained for both Cd_i and Zn_i in CdTe are given in Tables IV and V and shown in Fig. 2.3 while those for ZnTe are given in Tables VI and VII and shown in Fig. 2.4. According to the obtained results, interstitials at both sites induce a singlet state a_1 located in the upper half of the band gap, about 1.5 eV above the top of the valence band. This follows from the fact that an atom located at an interstitial site is surrounded by host atoms that have formed bonds with their four (host) neighbors. Consequently, the electrons of an interstitial do not form bonds with its neighbors, and the induced gap states are predominantly of non-bonding character. The a_1 level of the neutral interstitial is occupied by the number of electrons that is equal to the valence of the interstitial atom, i.e., by two electrons of cation interstitials in II-VI compounds. The Kohn-Sham energies of a_1 corrected for the GGA underestimation of the gap are given in Tables IV and V.

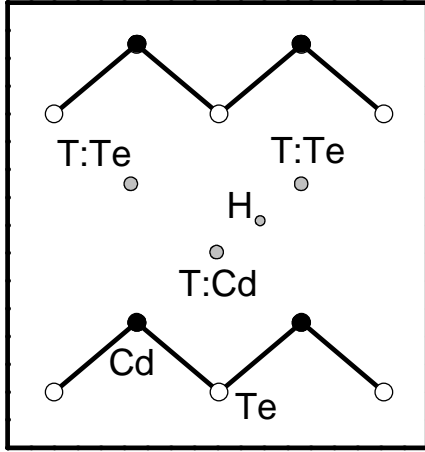


FIG 2.9. Locations of the two tetrahedral (T) and of the 'hexagonal' (H) interstitial sites in CdTe in a (110) plane. Cd and Te atoms are represented by solid and open circles, respectively. The x axis is in the [110] direction, and y axis in the [001] direction. Each tetrahedral site is surrounded by four atoms of the same type, two of which are out of the plane of the figure and are not shown.

2.2.1 Zn and Cd interstitials in CdTe

The calculated formation energies of Cd_i and Zn_i in CdTe as a function of the Fermi energy in Cd-rich conditions for minimum formation energy locations are presented in Fig. 2.3. The difference in E_{form} between the Cd-rich and Te-rich limits is the heat of formation of a given compound, in accordance with Eq. (1.4).

As it was mentioned above, both interstitials induce levels in the upper part of the gap, which may lead to errors in formation energies calculated within GGA. A scheme to estimate and correct these errors, indicated in Chapter 1, is now applied to both interstitials, and the results are shown in Figs. 2.10 and 2.11. Figure 2.10 shows E_{form} of Cd_i in CdTe for both interstitial sites obtained using (a) GGA, (b) GGA and the M-P corrections, and (c) including both the M-P corrections and shifting the interstitial energies by the underestimation of the band gap $\Delta E_{\text{gap}} = E_{\text{gap}}^{\text{exp}} - E_{\text{gap}}^{\text{GGA}}$. From Fig. 2.10 it follows that the M-P corrections and the gap corrections act in opposite ways. The M-P corrections decrease E_{form} of the charged defects, and thus increase the difference between the transition levels $\epsilon(0/+)$ and $\epsilon(+/2+)$. In contrast, the gap corrections increase E_{form} of interstitials in the neutral and 1+ charge state, which favors the negative- U situation. Cd_i is a negative- U defect in the GGA, positive- U defect after the M-P corrections, and again negative- U with the gap corrections included. The final

results (with both M-P and band gap corrections) for both interstitials in CdTe and ZnTe are shown in Figs. 2.10 and 2.11, respectively.

In agreement with the fact that cation interstitials are donors, their charge state depends on the Fermi energy, and is neutral in n-type samples and 2+ in p-type samples. As it follows from Figs. 2.10 and 2.11, formation energies of neutral interstitials are relatively large, and their equilibrium concentrations are lower than 10^6 cm^{-3} (computed by supposing $T=600 \text{ K}$, i.e., the temperature of molecular beam epitaxy (MBE) growth of CdZnTe samples). Thus, they play a negligible role in n-type samples. In contrast, in p-type samples Cd_i^{++} have low formation energies and they are the dominant compensating donors, as it is discussed in Sec. 2.5.

A comparison of the results in Figs. 2.10 and 2.11 shows that under Cd-rich conditions the expected concentrations of Zn_i and Cd_i at the T:Te sites are high and very close. Relative energies of interstitials at the T:Te and T:Cd sites are discussed in detail in Sec. 2.5 devoted to the interstitial diffusion.

Formation energies are affected by atomic relaxations. As it follows from Tables IV and V, the sign and the magnitude of lattice relaxation effects depend on the charge state, and on the interstitial site. In particular, neutral interstitials induce fully symmetric breathing-mode outward displacements of neighbors. For example, in the case of Cd_i at the T:Cd site, the outward relaxation of the first neighbors, Δd_1 , increases from 3.7 % for the neutral to 8.3 % for the doubly charged state, while simultaneously the distance to the six second neighbors Δd_2 decreases. These tendencies can be explained in terms of simple electrostatic considerations based on the fact that cations are positively charged and anions are negatively charged: an interstitial located at the T:cation site repels the cation neighbors more strongly when it is more positively charged. The opposite effect is expected and found for the second neighbors, Te, which are anions. For Cd_i at the T:Te site, the increased Coulomb attraction explains why the outward relaxation of anions, given by Δd_1 , is reduced from 6.9 % for the neutral state to 1 % for the 2+ state. Finally, in agreement with the non-bonding character of the defect-induced a_1 states, their energies are practically not affected by the relaxation

effects.

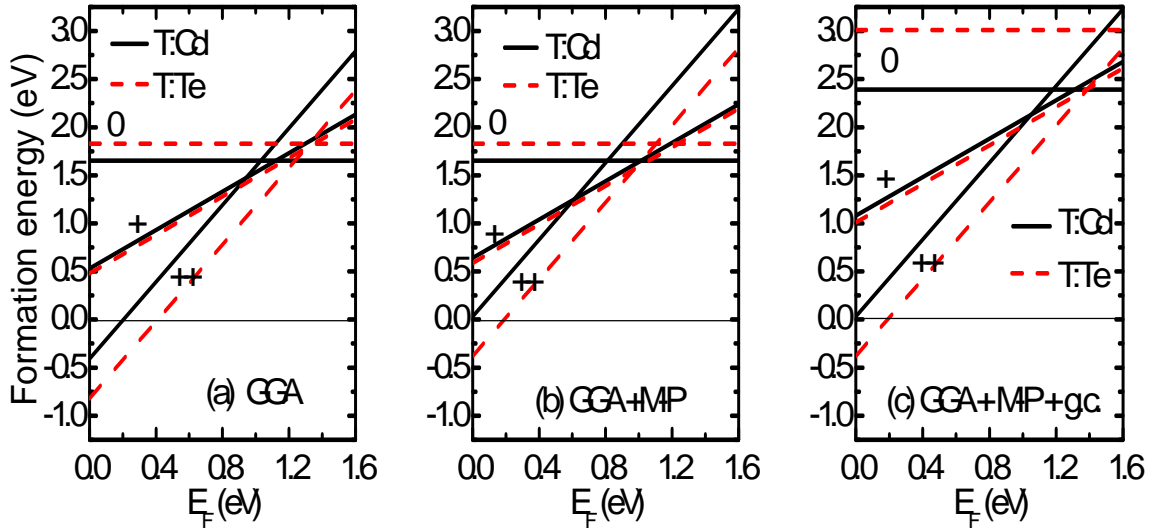


FIG. 2.10. Calculated formation energies of Cd_i in CdTe as a function of the Fermi energy at the Cd-rich limit for both the T:Cd and T:Te sites. (a) bare GGA results, and those after including (b) the M-P corrections, and (c) both M-P and the gap corrections. See text for details.

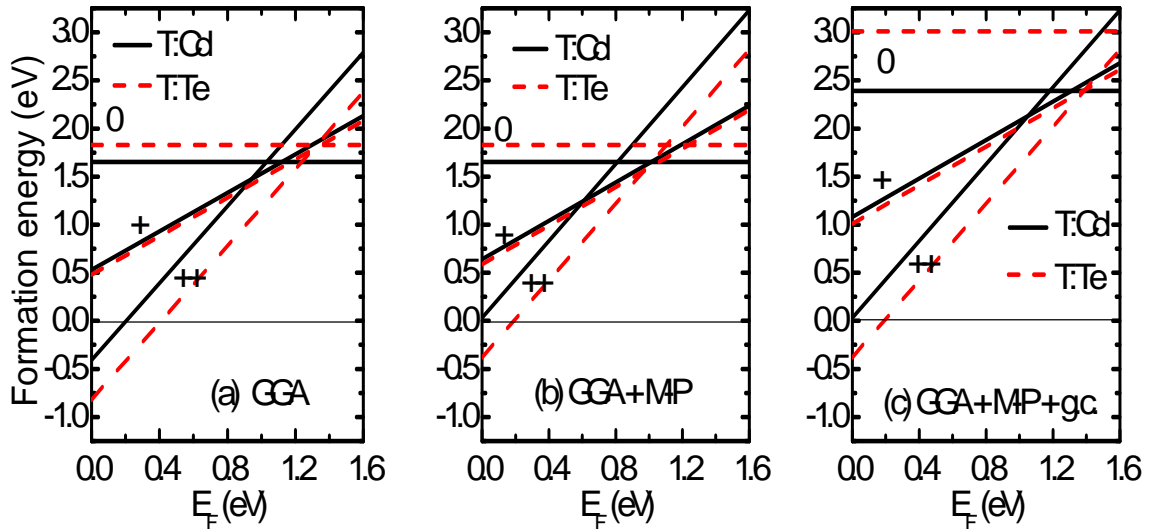


FIG. 2.11. Calculated formation energies of Zn_i in CdTe as a function of the Fermi energy at the Cd-rich limit for both the T:Cd and T:Te sites. (a) bare GGA results, and those after including (b) the M-P corrections, and (c) both M-P and the gap corrections. See text for details.

TABLE IV. Energies of the singlet state a_1 , changes of the distances to the first Δd_1 and the second Δd_2 neighbors, and relaxation energies ΔE_{relax} for neutral and charged states of Cd_i in CdTe. When presenting energy of the a_1 state band gap correction ΔE_{gap} was taken into account.

	Cd_i^0		Cd_i^+		Cd_i^{++}	
	T: Cd	T: Te	T: Cd	T: Te	T: Cd	T: Te
a_1 (eV)	0.75	1.10	0.80	1.10	0.90	1.10
Δd_1 (%)	3.72	6.90	6.37	2.76	8.31	1.01
Δd_2 (%)	2.58	0.19	0.29	3.22	-1.64	4.40
ΔE_{relax} (eV)	0.26	0.45	0.31	0.40	0.52	0.60

In general, properties of Zn_i and Cd_i in both ZnTe and CdTe are similar. I discuss here in detail Zn_i in CdTe. The contributions to the DOS of the Zn_i in CdTe at the T:Te and T:Cd sites are presented in Figs. 2.12 and 2.15, respectively. Zn_i at the two tetrahedral sites have distinct electronic structure. At both sites Zn_i in CdTe introduces deep d metal state in the valence band, at about -6 eV, and a localized state in the bandgap. Wave function square is mainly localized around interstitial atom and surrounding atoms (see Fig. 2.14a i b). In case of T:Te, $|\psi|^2$ of the a_1 state has the antibonding character with respect to the interstitial atom at the four surrounding Te nearest neighbors. The nearest six Cd atoms do not contribute to the a_1 state. It is clearly evident in Fig. 2.13 where contributions to DOS from the nearest Cd and Te atoms are presented. Transition to the T:Cd case alters the character of the a_1 state. $|\psi|^2$ is still localized around the interstitial atom, but with the additional bonding character at the six surrounding Te atoms (the second nearest neighbors of the interstitial atom) with respect to the Zn_i atom (Fig. 2.14b). The first nearest neighbors, the four Cd atoms, contribute very scantily to $|\psi|^2$ of the a_1 state (Figs. 2.14b and 2.16). The spread of charge to the neighbors by the interstitials is strongly suggesting that they can play a crucial assisting role in diffusion of anion based defects, and this is charge dependent phenomena.

TABLE V. Energies of the singlet state a_1 , changes of the distances to the first Δd_1 and the second Δd_2 neighbors, and relaxation energies ΔE_{relax} for Zn_i in CdTe. When presenting energy of the a_1 state band gap correction ΔE_{gap} was taken into account.

	Zn_i^0		Zn_i^+		Zn_i^{++}	
	T: Cd	T: Te	T: Cd	T: Te	T: Cd	T: Te
a_1 (eV)	0.85	1.20	0.85	1.20	0.85	1.20
Δd_1 (%)	1.25	2.53	3.55	-1.35	6.86	-3.00
Δd_2 (%)	2.06	1.50	0.21	3.50	-2.45	4.38
ΔE_{relax} (eV)	0.09	0.35	0.37	0.50	0.55	0.85

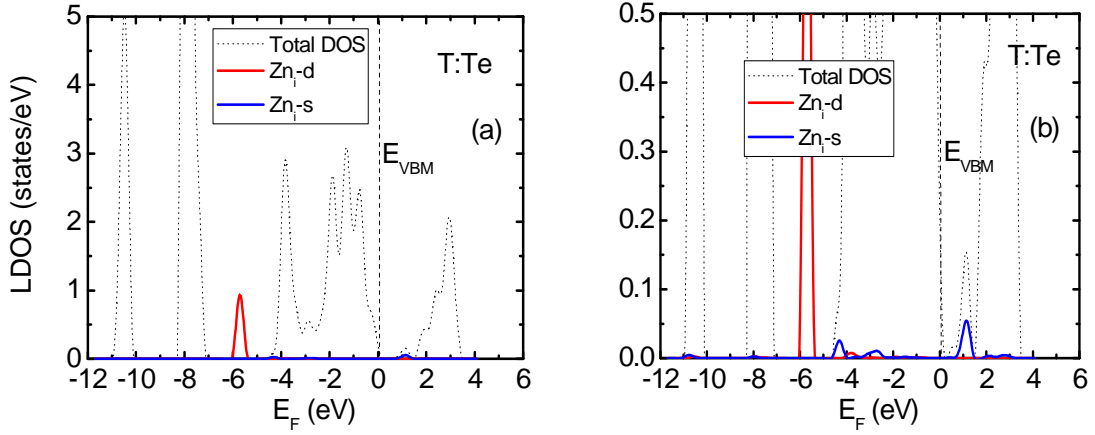


FIG. 2.12. Total DOS of CdTe:Zn and angular momentum projected local density of states (LDOS) for Zn_i at the T:Te site in CdTe:Zn. Zero energy is at the VBM. (b) figure is ten-fold magnified with respect to (a) figure to highlight small features at about -4 eV.

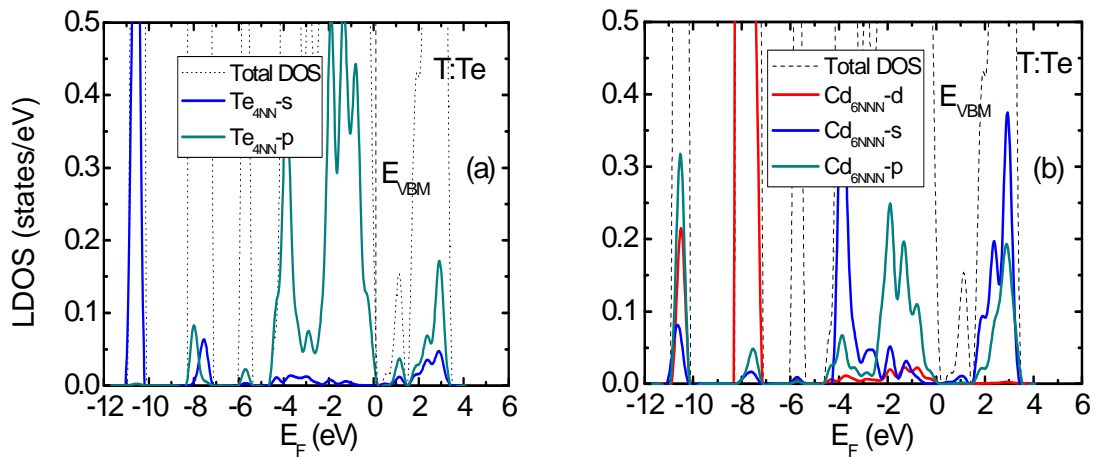


FIG. 2.13. Total DOS of CdTe:Zn, and LDOS for (a) the four nearest neighbor Te atoms and (b) the six nearest neighbor Cd atoms of Zn_i at the T:Te site in CdTe:Zn. Zero energy is at the VBM. y axis is magnified with respect to Fig. 2.12a to highlight features.

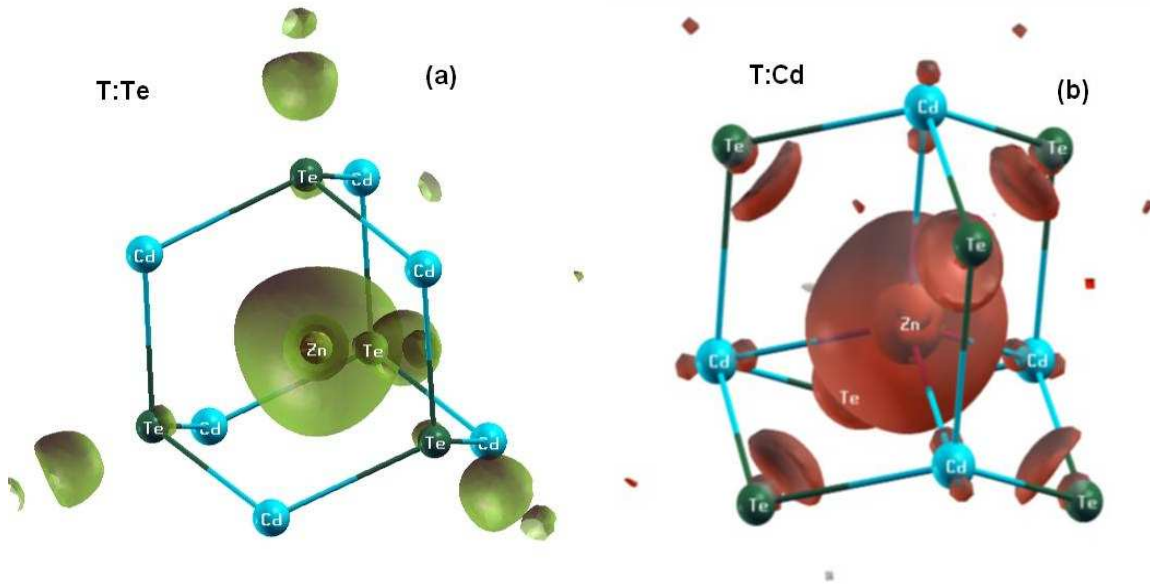


FIG. 2.14. Wave function square of the a_1 state of Zn_i at the (a) T:Te and (b) T:Cd sites in CdTe.

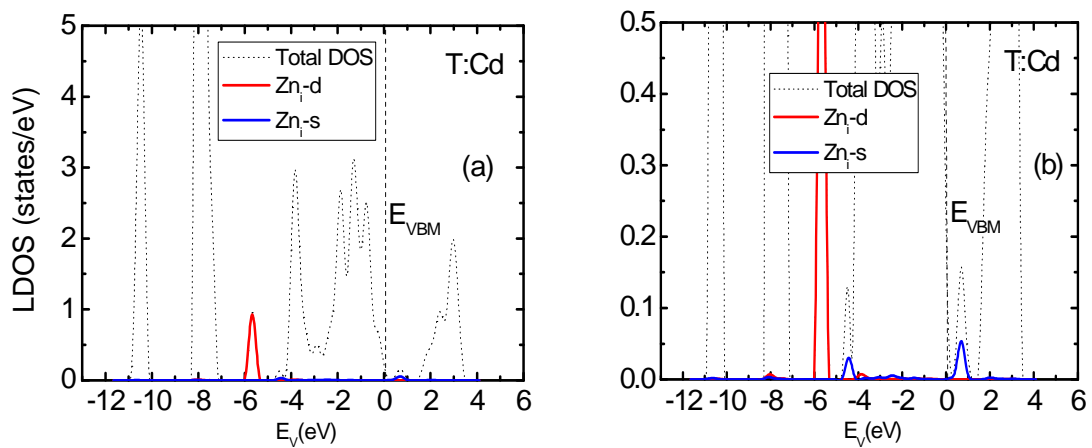


FIG. 2.15. Total DOS of CdTe:Zn and LDOS for Zn_i at the T:Cd site in CdTe:Zn. Zero energy is at the VBM. (b) figure is ten-fold magnified with respect to (a) figure to highlight small features at about -4 eV.

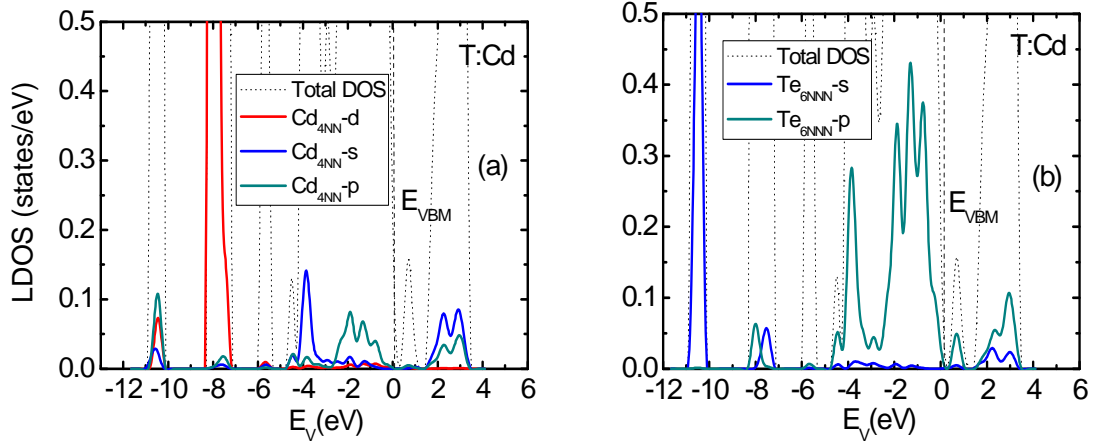


FIG. 2.16. Total DOS of CdTe:Zn and LDOS for (a) four nearest neighbor Cd atoms and (b) six nearest neighbor Te atoms of Zn_i at the T:Cd site in CdTe:Zn. Zero energy is at the VBM. y axis is magnified with respect to Fig. 2.15a to highlight features.

It is relevant to compare formation energies of Cd_i in CdTe with those calculated in Ref. 39, using the LAPW method and neglecting the M-P corrections. LAPW has given in Ref. 39 almost correct gap of CdTe, and therefore the gap corrections was not necessary. For the neutral Cd_i the results of Figs. 2.10a and b, 1.6 and 2.4 eV, respectively, bracket the value 2.0 eV of Ref. 39. Moreover, in the spirit of arguments presented in Chapter 1, the mid-gap interstitial levels should be corrected by one-half of the band gap error. Applying this correction leads to a very good agreement with both E_{form} and transition level energies of Cd_i in CdTe. However, the accuracy is too low to unambiguously assess the negative- U character of the defect. A more detailed comparison is not possible, since in Ref. 39 E_{coh} of elemental Cd and Te are not given.

2.2.2 Zn and Cd interstitials in ZnTe

I now turn to Cd and Zn interstitials in ZnTe. The results are shown in Fig. 2.14 and in Tables VI and VII. In general, the calculated properties of both interstitials are similar to those in CdTe. In particular, both interstitials are donors with the singlet a_1 state located in the upper half of the band gap.

TABLE VI. Energies of the singlet state a_1 , changes of the distances to the first Δd_1 and the second Δd_2 neighbors, and relaxation energies ΔE_{relax} for neutral and charged states of Cd_i in ZnTe. When presenting energy of the a_1 state band gap correction ΔE_{gap} was taken into account.

	Cd_i^0		Cd_i^+		Cd_i^{++}	
	T:Zn	T:Te	T:Zn	T:Te	T:Zn	T:Te
a_1 (eV)	1.55	1.85	1.60	1.90	1.60	1.95
Δd_1 (%)	3.16	8.73	5.23	6.55	7.06	5.04
Δd_2 (%)	4.00	0.68	2.24	2.19	0.86	3.22
ΔE_{relax} (eV)	0.41	0.89	0.40	0.83	0.53	0.95

TABLE VII. Energies of the singlet state a_1 , changes of the distances to the first Δd_1 and the second Δd_2 neighbors, and relaxation energies ΔE_{relax} for Zn_i in ZnTe. When presenting energy of the a_1 state band gap correction ΔE_{gap} was taken into account.

	Zn_i^0		Zn_i^+		Zn_i^{++}	
	T:Zn	T:Te	T:Zn	T:Te	T:Zn	T:Te
a_1 (eV)	1.45	1.90	1.45	1.90	1.35	1.90
Δd_1 (%)	0.44	4.64	3.31	2.47	5.19	0.87
Δd_2 (%)	2.96	1.17	1.03	2.36	-0.47	3.40
ΔE_{relax} (eV)	0.15	0.26	0.14	0.32	0.28	0.56

Zn_i in ZnTe was considered in Ref. 46. The results given in Fig. 2.14, obtained using both the M-P expression, and additionally corrected for the half of the underestimation of the GGA band gap, agree with those of Ref. 46 to within 0.2 eV. A more detailed comparison is not possible, since in Ref. 46 the correction of the band gap refers to its value at the mean value point rather than to the gap calculated at Γ .

Analysis of the obtained results allows drawing several general conclusions regarding the properties of interstitials:

1. Energy levels (Tables IV-VII) as well as transition energies (Figs. 2.13 and 2.14) of Zn_i are lower than those of Cd_i by about 0.3 eV. This holds for both T:Te and T:cation sites, and for both CdTe and ZnTe hosts. The effect follows from the fact that the interstitial-induced a_1 level is dominated by the s orbital of the interstitial, it retains its chemical identity. Thus it mainly reflects the energy of the relevant orbital of an isolated atom. In fact, the

energy of s orbital of isolated Zn, -5.96 eV, is about 0.3 eV lower than that of Cd, -5.64 eV (both values are obtained for the employed pseudopotentials).

2. A comparison of Figs. 2.13 and 2.14 with the corresponding Tables IV-VII shows that the transition energies relative to the VBM of both interstitials at both sites in ZnTe are higher than those in CdTe. This result agrees with the fact that the top of the valence band of ZnTe is lower than that in CdTe, as the experimental valence band discontinuity in a ZnTe/CdTe heterojunction is 0.10 eV [47]. Thus, because of their non-bonding character, interstitial states may be regarded as 'absolute reference levels'.

3. Formation energies of Zn_i are in general lower than those of Cd_i . The energy difference is about 0.35 eV in neutral state, see Figs. 2.13 and 2.14. The effect follows from the smaller atomic radius of Zn. In fact, as it was mentioned at the beginning of this Section, both interstitials induce non-negligible outward displacements of neighbors, and thus generate excess elastic energy of local strains. On the other hand, for low Fermi energies, i.e., for the $2+$ charge state, the stable sites of both defects are T:Te, and formation energies of Zn_i and Cd_i are almost equal according to Figs. 2.13 and 2.14. In this case, the strain is lower for Cd_i , for which $\Delta d_1 = 1\%$, than for Zn_i , for which $\Delta d_1 = -3\%$.

4. Strain effects also explain the fact that formation energies of interstitials in ZnTe are higher than in CdTe by about $0.7-0.8$ eV. This effect follows from the smaller lattice constant and higher stiffness of ZnTe, and thus higher strain energies generated by interstitials.

2.2.3 Diffusion of cation interstitials

Diffusion of self-interstitials occurs along paths that contain the interstitial tetrahedral sites, i.e., along $-T:Te-T:Cd-T:Te-$ path shown in Fig. 2.9. Changes of the total energy of both Zn and Cd interstitials as a function of their location along the diffusion path in CdTe and ZnTe are presented in Figs. 2.17 and 2.18, respectively. Both neutral and positively charged defects were considered. The results strongly depend on the charge state.

I begin with neutral defects. As it was discussed in Sec. 2.2.1, in all cases under study the stable location of interstitials is T:cation, while the T:Te sites are metastable. More precisely, total energy of both Cd_i and Zn_i at T:Cd in CdTe is lower than at the T:Te site by 0.38 eV and 0.16 eV, respectively, see Fig. 2.17 and Table VIII. In ZnTe, the stability at T:Zn is more pronounced, since energy of both interstitials at T:Zn is lower by 0.4 eV, see Fig.

2.18. The maximum of the energy barrier separating the two sites is close to the H site shown in Fig. 2.9. Diffusion can occur by thermally activated jumps between the two types of sites, and is determined by the larger barrier. In the case of CdTe, the diffusion barriers of both Zn_i^0 and Cd_i^0 are close, about 0.7 eV in CdTe, Fig. 2.17, and somewhat higher, about 1.1 eV, in ZnTe, Fig. 2.18. Barriers for the reverse jumps from the metastable T:Te to the stable T:cation sites are higher in ZnTe, and amount to about 0.7 eV. In CdTe, these barriers are lower, 0.55 eV and 0.31 eV for Zn_i^0 and Cd_i^0 respectively.

TABLE VIII. Calculated diffusion barriers (in eV) for different configurations and charge states of cation interstitials in CdTe and ZnTe. T:c denotes the T: Cd and the T: Zn site depending whether the interstitial is considered in CdTe or ZnTe, respectively.

Path	Charge State	Barriers			
		CdTe: Cd	CdTe: Zn	ZnTe: Cd	ZnTe: Zn
T:Te-T:c	0	0.3	0.6	0.8	0.6
T:c-T:Te	0	0.7	0.7	1.2	1.0
T:Te-T:c	+	0.6	0.5	0.8	0.6
T:c-T:Te	+	0.7	0.1	1.0	0.6
T:Te-T:c	2+	0.9	0.9	0.8	0.4
T:c-T:Te	2+	0.6	0.0	0.8	0.0

Energetics and diffusion of a doubly charged Zn_i^{++} in CdTe is qualitatively different than that of the neutral one, see Fig. 2.17a. In fact, the only stable site is T:Te, while the T: Cd site, which is the ground state configuration of the neutral Zn_i^0 , corresponds to the maximum of the energy barrier. Consequently, the diffusion occurs by long and curvilinear jumps between two adjacent T:Te sites with the energy barrier of 0.85 eV. From Figs. 2.18 it follows that a similar situation takes place also for Zn_i^{++} in ZnTe, where the energy barrier is close to 0.45 eV, and the T: Zn site is a center of a large energy plateau between adjacent T:Te sites. Finally, interstitial Cd_i^{++} in both CdTe and ZnTe diffuses with a barrier of 0.87 eV between T: Cd and T:Te sites. In ZnTe, its energies are identical within our accuracy. In CdTe, the T: Cd site is less stable by about 0.25 eV than the T:Te site.

Analysis of these results shows that energetics of interstitials, i.e., the dependence of total energy on the location in the unit cell and on the charge state, is determined by two

factors. The first one is the dependence of energy of the defect-induced a_1 level on the defect location, shown in Fig. 2.17c for CdTe and in Fig. 2.18c for ZnTe. The second factor is the ionicity of the host. Both factors will now be discussed.

Relative energies of interstitials at T:cation and T:Te sites are mainly determined by energies of the a_1 levels. In particular, in the case of Zn_i in CdTe, the a_1 level decreases by 0.4 eV from 1.2 to 0.8 eV when the interstitial moves from T:Te to T:Cd, see Fig. 2.17c. This fact does not affect the energy of Zn_i^{++} , since for this charge state the a_1 level is empty. In contrast, in the case of the neutral Zn_i this level is occupied with two electrons, and the shift of Zn_i from T:Te to T:Cd induces an energy gain of $2 \cdot 0.4 \text{ eV} = 0.8 \text{ eV}$ that stabilizes Zn_i at the T:Cd site, which correlates well with the total energy gain of 1 eV. Similarly, in the case of Cd_i at T:Cd in CdTe, total energy of Cd_i^0 is 0.6 eV lower than that of Cd_i^{2+} (Fig. 2.17b), which is fully accounted for by the change of the energy of the doubly occupied a_1 by 0.3 eV (Fig. 2.17c). The comparison of Figs. 2.18a and 2.18b with Fig. 2.18c shows that the same explanation is also valid for interstitials in ZnTe. Moreover, results found for singly charged interstitials are intermediate between these for neutral and doubly charged defects.

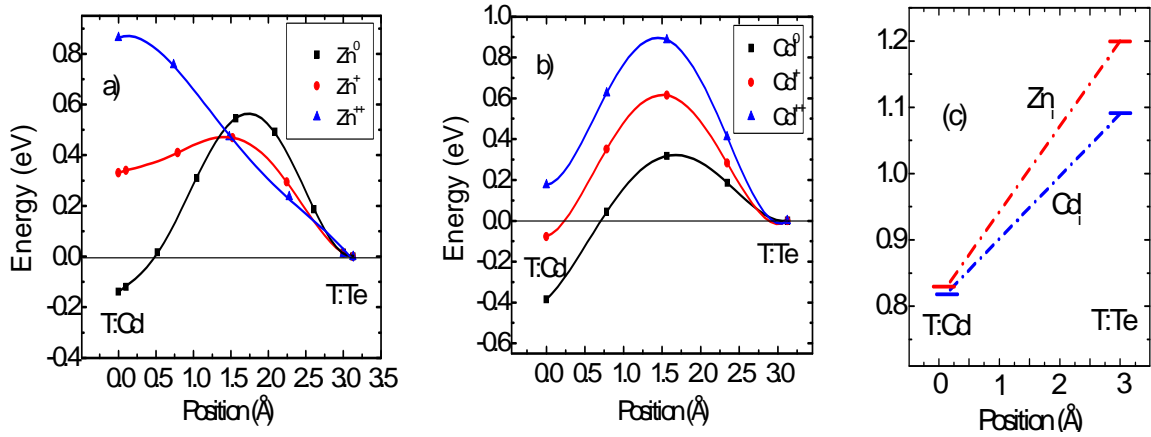


FIG. 2.17. The total energy of (a) Zn_i and (b) Cd_i in CdTe as a function of the location along the diffusion path for three charge states. The zero of energy is assumed at the T:Te site. Figure (c) shows the energy of the a_1 level at both tetrahedral sites for Zn_i and Cd_i . The lines are to guide eye only.

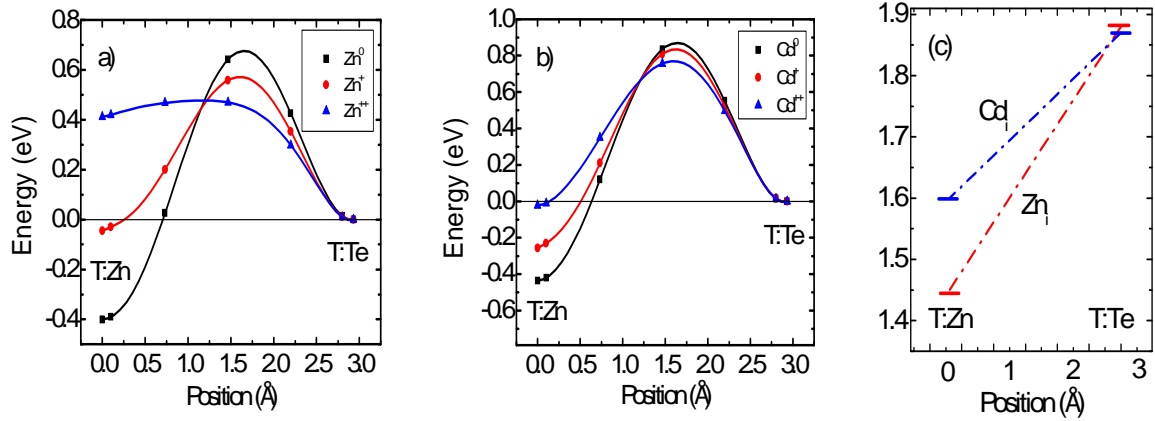


FIG. 2.18. The total energy of (a) Zn_i and (b) Cd_i in ZnTe as a function of the location along the diffusion path for three charge states. The zero of energy is assumed at the T:Te site. Figure (c) shows the energy of the a_1 level at both tetrahedral sites for Zn_i and Cd_i . The lines are to guide eye only.

Turning to the effects of the ionicity of the host we observe that in the case of interstitials in the 2+ state, the energy difference between T:Te and T:cation is higher in the more ionic CdTe due to Coulomb interactions. This is in line with charge dependence of the interstitial-host bond lengths discussed in Sec. 2.2.1. These results are also consistent with those of Ref. 46 studying ZnO, ZnS, ZnSe, and ZnTe, in which ionicity differs due to the different anions (and not cations, as in our case). This indicates that the role of ionicity has a universal character. Moreover, the ionicity of the host may play a role even in the case of neutral interstitials. From Figs. 2.17 and 2.18 it follows that the energy of a neutral interstitial is lower in T:cation than in T:Te, and this difference is higher in less ionic ZnTe. This trend is also present in the series of compounds studied in Ref. 46.

Interestingly, Figs. 2.17 and 2.18 suggest that diffusion of neutral Zn_i in both CdTe and ZnTe can be enhanced by injection of holes or illumination of the sample. The mechanism is similar to the Bourgoin-Corbett mechanism of athermal recombination-enhanced diffusion provoked by successive capture/emission of electrons by a defect [48]. In fact, the T:cation site is stable for a neutral Zn_i , but is an energy maximum for Zn_i^{2+} . Consequently, after a capture of 2 holes, Zn_i^{2+} relaxes with no energy barrier to the T:Te site. Here, either the interstitial persists in the 2+ state and migrates with the barrier of 0.4 eV in ZnTe (0.9 eV in CdTe), or it captures two electrons, and returns to the stable T:cation site

with the barrier of 0.6 eV (ZnTe) or 0.6 eV (CdTe). In both cases (except Zn_i^{++} in CdTe), the effective diffusion barrier is *reduced* relative to that of the neutral interstitial.

Table IX summarizes the obtained diffusion barriers with those of [46] that were calculated using a 'direct' approach, i.e., by fixing the position of an interstitial at a number of sites between T:cation and T:Te. Comparison of the two methods indicates that the two methods give qualitatively similar results, but in general the NEB barriers are higher, which is surprising since in principle NEB allows to find the lowest barriers.

TABLE IX. Calculated diffusion barriers (in eV) for different configurations and charged states of Zn_i in ZnTe.

Starting point	Charge State	This work NEB	Ref. 46
T:Te	(0)	0.6	0.24
T:Te	(+)	0.6	0.27
T:Te	(2+)	0.4	0.45
T:Zn	(0)	1.0	0.80
T:Zn	(+)	0.6	0.47
T:Zn	(2+)	0.0	0.15

In summery, the most important result of this Section is that the diffusion barriers are rather small, 0.45-1.05 eV, what implies a possible mobility of interstitials even at room temperature. Finally, relative energies of an interstitial at the two tetrahedral sites as well as their energy dependencies on the charge state are almost completely determined by the energy of the a_1 state, its occupation by electrons, and its dependence on the location of the interstitial.

2.3 Anion vacancies

As in the case of cation vacancy, the formation of anion vacancy implies four dangling bonds of the four cation nearest neighbors, i.e. the Cd or Zn atoms depending whether CdTe or ZnTe is considered, which form a singlet a_1 and triplet t_2 states. However, since the cation orbitals are higher in energy than the anion orbitals, both a_1 and t_2 levels of anion vacancy are

shifted upwards relative to those of cation vacancy. Because each Cd bond is occupied with $2/4$ electrons, the levels of a neutral anion vacancy are occupied with $4 \cdot (2/4) = 2$ electrons. Two of them are located on the a_1 singlet, which is below VBM (Fig. 2.19). There is also the higher energetic triplet t_2 state which is resonant with the conduction band and lies about 1.5 eV above the CBM (Fig. 2.19).

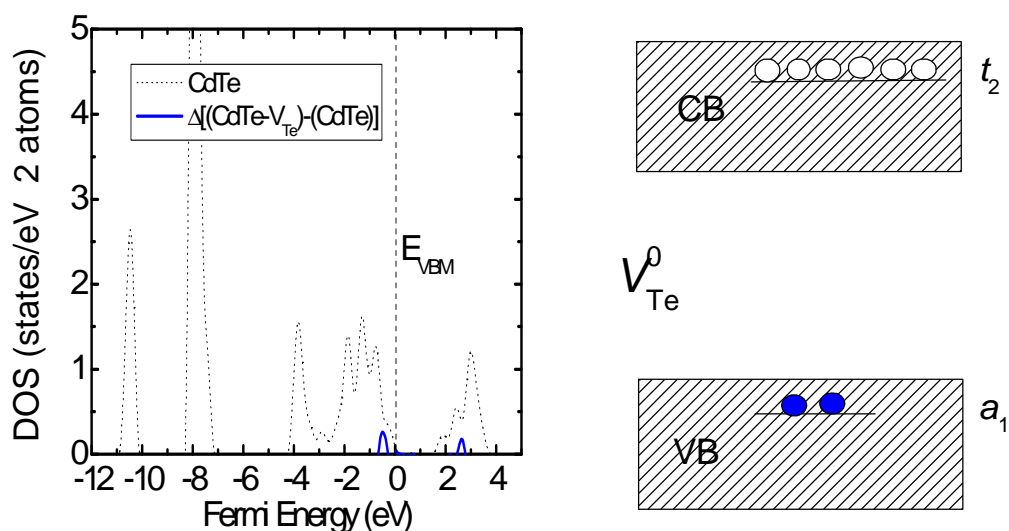


FIG. 2.19. Calculated density of states for CdTe and density of states' difference between CdTe with neutral anion vacancy, $\text{CdTe-V}_{\text{Te}}^0$, and CdTe without the defect. The energy alignment is implemented (see Chapter 1).

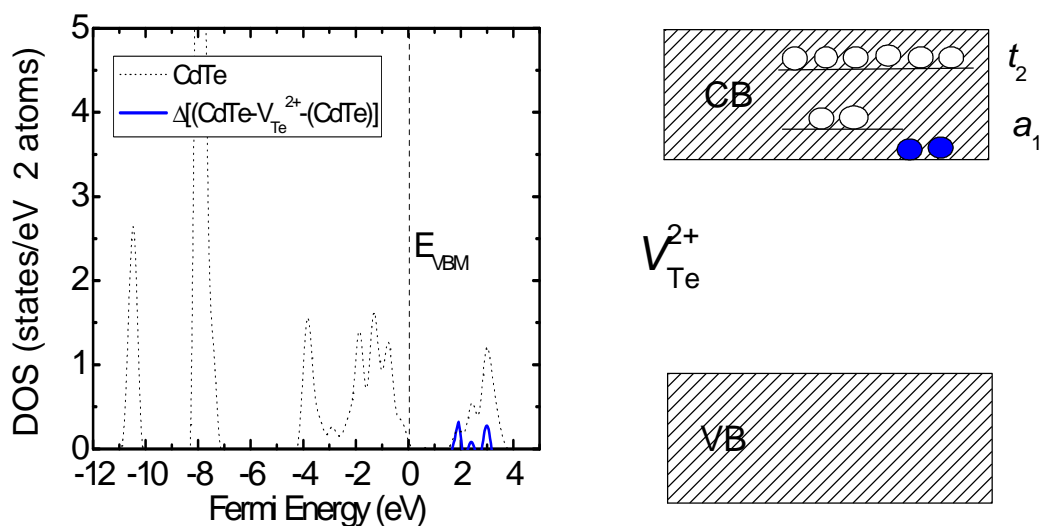


FIG. 2.20. Calculated density of states for CdTe and density of states' difference between CdTe with anion vacancy in 2+ charge state, $\text{CdTe-V}_{\text{Te}}^{2+}$, and ideal CdTe without the defect. The energy alignment is implemented.

Relaxation plays a crucial role in the stability of anion vacancy. I discuss it in the case of CdTe, since ZnTe is qualitatively very similar. In the ideal non-relaxed case, the a_1 vacancy state is in the gap, and the transition levels $\varepsilon_{V_{\text{Te}}}(0/+)$ and $\varepsilon_{V_{\text{Te}}}(+/++)$ are 0.60 and 1.35 eV, respectively. This is in good agreement with the values of 0.67 and 1.27 eV calculated in Ref. 49 for the abovementioned transition levels. The energy levels and the E_{form} of non-relaxed V_{Te} are shown in Fig. 2.21. When relaxation is included, the energetics of the charged states alters dramatically. Both V_{Te}^0 and V_{Te}^{++} lower their formation energies due to relaxation by more than 1 eV, which is also accompanied by huge shifts of the corresponding energetic positions of the a_1 levels. Inward relaxation mainly caused by nearest neighbor Cd atoms is valid for V_{Te}^0 . It pushes the a_1 level deep in the valence band (Figs. 2.19 and 2.21a). Outward relaxation of the nearest neighbor Cd atoms is characteristic of V_{Te}^{++} and gives rise to the upward shift of a_1 level above the CBM (Figs. 2.20 and 2.21a). The relaxation stands behind this upward shift and diminishes the role played by electrostatic Coulomb repulsion which, if dominating, would have displaced a_1 level downward in V_{Te}^{++} . V_{Te}^+ , in opposition to neutral and 2+ charged states, experiences small relaxation ($\Delta E_{\text{relax}} = 0.15$ eV) and subsequent shift of the a_1 level (it relaxes to 0.6 eV above VBM). It is interesting to understand different relaxation modes occurring in neutral and 2+ charge state in more detail.

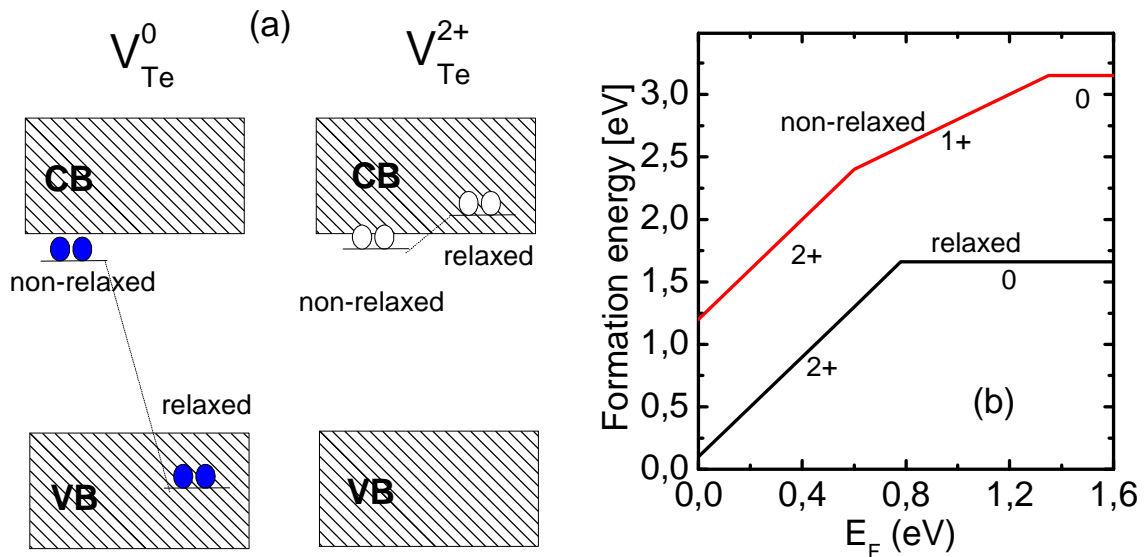


FIG. 2.21. (a) Schematic representation of a_1 level, and (b) E_{form} of V_{Te} in CdTe in non-relaxed and relaxed cases. See text for more details.

Outward relaxation of the nearest neighbor Cd atoms in V_{Te}^{++} can be interpreted in terms of the rehybridization toward sp^2 bonding. Both the nearest neighbor Cd atoms and the next nearest neighbor Te atoms move about 65% of their way in the direction to create deformed planar sp^2 bonding (Fig. 2.22). The next nearest neighbor Te atoms experience inward relaxation enabling the rehybridization. This behavior bears the close resemblance to 3+ charged arsenic vacancy in GaAs, also provoked by the empty a_1 level [50].

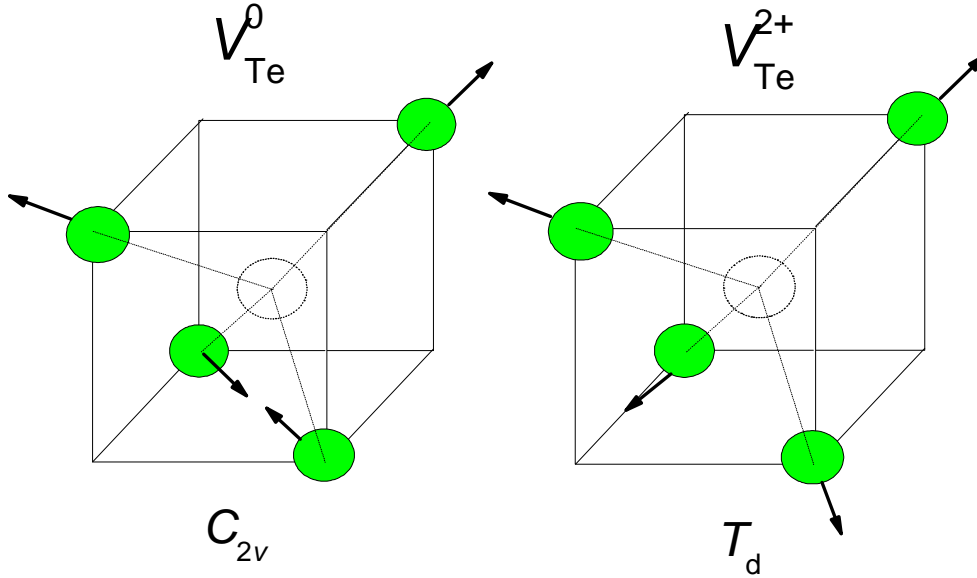


FIG. 2.22. The relaxation pattern and point-group symmetry corresponding to the neutral and 2+ state of V_{Te} in CdTe.

In contrast to V_{Te}^{++} which experience outward relaxation that maintains T_d symmetry, V_{Te}^0 undergoes sharp symmetry lowering. The orthorhombic (C_{2v}) relaxation mode (Fig. 2.22), which is the lowest in energy, entails the formation of Cd-Cd dimer bonds which is realized when two Cd atoms are displaced outward anion vacancy with the remaining two Cd atoms engaged in the formation of the dimer. Analysis of the wavefunctions shows that the a_1 orbital pertaining to the V_{Te}^0 is constructed from bondinglike combination of two Cd dangling bond orbitals, in contrast to V_{Te}^{++} state which is formed by combination of four nearest neighbor orbitals. Due to nondegeneracy of a_1 orbital of V_{Te}^0 the Jahn-Teller effect cannot explain the lowering of symmetry. It can be attributed to the chemical stability of metal-metal bonds that leads to the formation of the dimer. The structural configurations around relaxed anion vacancies are given in Table X. The dimer formation in neutral anion vacancy was identified for almost all II-VI and chalcopyrite compounds [51,

52]. 20% of outward relaxation was calculated for nearest neighbors in 2+ state in CdTe in Ref. 53, which is close to 28.5% calculated in this work. The comparison is not possible for the neutral vacancy, because Cd-Cd dimer formation was not considered in Ref. 53.

The V_{Te}^+ case with half-occupied a_1 orbital is intermediary between above cases, and the above two mechanisms (i.e., those characteristic of V_{Te}^0 and V_{Te}^{2+}) partially cancel. That is why the relaxation and the shift of the a_1 level are so weak compared with 0 and 2+ charge states. V_{Te}^+ is unstable against charge disproportion $2V_{\text{Te}}^+ \rightarrow V_{\text{Te}}^{2+} + V_{\text{Te}}^0$, thus V_{Te} in CdTe is a negative- U defect with $U=-0.75$ being the energy balance of the above reaction. This results in the lack of V_{Te}^+ in the ground state for all accessible Fermi energies (Figs. 2.23 and 2.24) of anion vacancies, and with transition energy $\varepsilon_{V_{\text{Te}}}(0/++) = 0.80$ eV.

The E_{form} of anion vacancy in CdTe was calculated in Ref. 39 and Ref. 53. In Ref. 53 the absolute values of E_{form} were not provided, the defect was identified as a negative U -center with $\varepsilon_{V_{\text{Te}}}(0/++)$ transition at 0.85 eV which is close to 0.80 eV calculated in this work. Nevertheless, the authors failed to identify the possibility of the C_{2v} symmetry reconstruction due to the formation of Cd-Cd dimers in the neutral state, which is critical for the correct description of the ground state of V_{Te} . The same shortcoming is present in Ref. 39, which also lacks in the examination of the C_{2v} reconstruction, but presents absolute value for the formation energy, which in Cd-rich regime is close to 2.5 eV in neutral state with $\varepsilon_{V_{\text{Te}}}(0/++)$ at about 0.8 eV.

The behavior of anion vacancy in ZnTe is very similar to CdTe. The relaxation modes valid for CdTe are also operative here (Table X). The relaxation of the neighborhood in ZnTe is comparable to the values presented in Ref. 51 with the differences not exceeding 5%. V_{Te}^+ is unstable against charge disproportion $2V_{\text{Te}}^+ \rightarrow V_{\text{Te}}^{2+} + V_{\text{Te}}^0$, thus V_{Te} in ZnTe is also a negative- U defect with $U= -0.83$ eV. Thus, the defect is not expected to be seen in EPR experiments. The formation energies presented in Figs. 2.23 and 2.24 show that anion vacancy in ZnTe is higher in energy than in CdTe, which stems from the arguments already given in Secs. 2.1 and 2.2.

The calculated electronic structure of V_{Te} has important consequences for experiment. First, because of the instability of the paramagnetic 1+ charge state of anion vacancy in both CdTe it can be easily explained why EPR signal is not observed or not straightforward to measure. Moreover, due to a substantial Franck-Condon effect, thermal and optical energies

are not comparable for V_{Te} . Because the a_1 level of V_{Te}^0 is broad resonance in the valence band, the optical excitations are negligible. Second, there are two conditions for persistent photoconductivity (PPC) to occur, namely, (i) optical availability of the neutral state, and (ii) metastability of 2+ charge state that introduce carriers into conduction band. The first condition out of the two required for the occurrence of PPC seems to be not satisfied even in n-type samples of CdTe and ZnTe [51], i.e., although the neutral charge state V_{Te}^0 is the initial equilibrium state in n-type material, it is not optically active. It is important to underline that if the computational procedure of Ref. 51 is employed, i.e., the VBM is shifted downward due to LDA+U correction, the a_1 level of V_{Te}^0 is above VBM in both CdTe and ZnTe, and therefore can be optically excited. Then since $\epsilon_{V_{\text{Te}}}(0/++)$ is around the mid-gap PPC can occur in CdTe and ZnTe, although only if the Fermi level is above $\epsilon_{V_{\text{Te}}}(0/++)$, i.e., in n-type material. The second condition demands precisely the a_1 orbital in 2+ charge state to be above CBM, and is satisfied in my computational scheme for both compounds. In this case V_{Te}^{++} leads to PPC by transferring the electrons to conduction band. The a_1 is a resonance with the conduction band and electrons occupying the perturbed host state do not spontaneously relax to deep localized state pertaining to V_{Te}^0 . The unoccupied a_1 state is above CBM. The transition to 0 charged state requires simultaneous capture of two electrons with thermal activation of approximately 0.25 eV. The feasibility of second condition of PPC, similar to the first condition, depends on the details of calculations. When the scheme [18, 51] of upward shift of CBM accommodating the discrepancy between experimental and calculated band gap after downward shift of VBM is employed, the a_1 level in ZnTe is no longer above CBM, and the photoexcited electrons relax spontaneously into deep localized state returning the vacancy into nonconducting V_{Te}^0 . The upward shift of CBM in CdTe is small enough, and even after correction PPC is possible provided the a_1 level in equilibrium stable V_{Te}^0 is above VBM and the material is n-type doped.

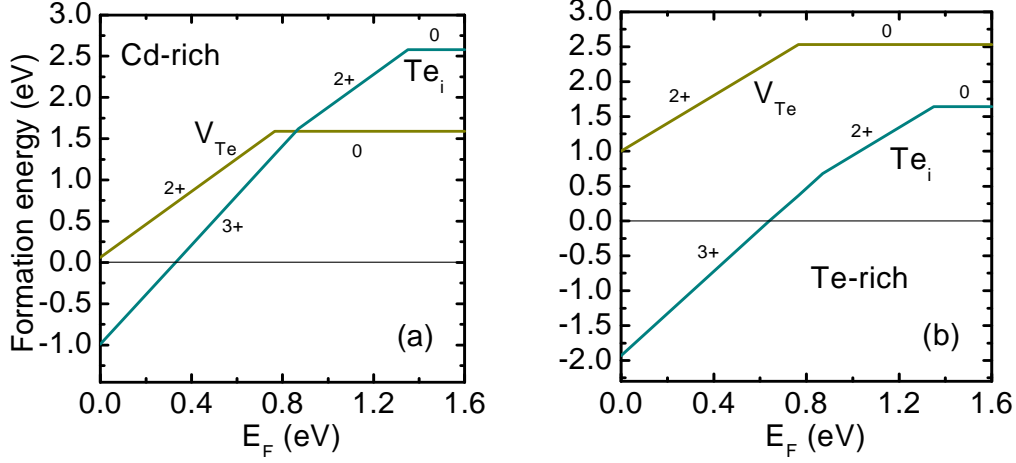


FIG. 2.23. Calculated formation energies of V_{Te} and Te_i in CdTe as a function of the Fermi energy in the (a) Cd-rich, and (b) Te-rich limit.

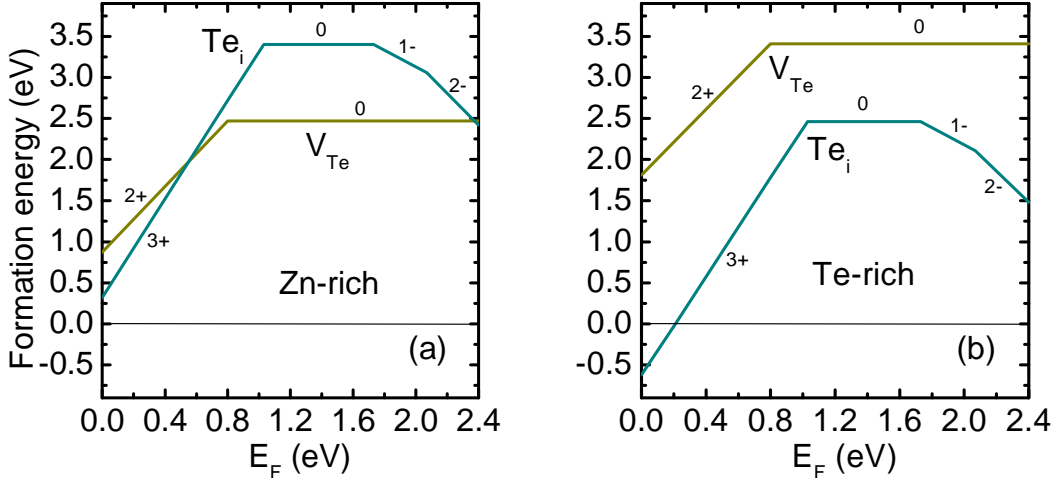


FIG. 2.24. Calculated formation energies of V_{Te} and Te_i in ZnTe as a function of the Fermi energy in the (a) Zn-rich, and (b) Te-rich limit.

TABLE X. Energies of the vacancy-induced singlet state a_1 with respect to VBM, the percentage changes of distances to the first (Δd_1) and second (Δd_2) neighbor with respect to the perfect crystal, and total energy gains due to relaxation ΔE_{relax} for neutral and charged states of V_{Te} in CdTe and ZnTe. In the case of neutral anion vacancy, where dimerized C_{2v} structure is the most stable, the changes of relative distances between the inward (in) and outward (out) relaxing metal neighbors are given with respect to the metal-metal distances in the perfect crystal. In 2+ charge state the T_d symmetry is maintained. The a_1 levels in V_{Te}^{++} are non-corrected GGA values.

	V_{Te}^0		V_{Te}^{++}	
	CdTe	ZnTe	CdTe	ZnTe
a_1 (eV)	-0.55	-0.45	1.80	1.95
Δd_1 (%)	(in) -55.8 (out) 28.2	(in) -43.2 (out) 25.3	28.5	25.3
Δd_2 (%) (average)	-5.1	-3.1	-6.6	-4.7
ΔE_{relax} (eV)	0.91	0.84	1.13	1.03

2.3.1 Diffusion of anion vacancies

In this section I analyze the diffusion of anion vacancies considering for all mechanisms investigated in detail in Sec. 2.1.1. The results are presented in Table XI and following:

(i) Diffusion to the first neighbor ($V_{\text{Te}} \rightarrow \text{Cd}_{\text{Te}} + V_{\text{Cd}}^{1st}$) is possible although not efficient in the case of V_{Te} both in CdTe and ZnTe, in all accessible equilibrium charge states. $\text{Cd}_{\text{Te}} + V_{\text{Cd}}^{1st}$ and $\text{Zn}_{\text{Te}} + V_{\text{Zn}}^{1st}$ defect pairs are unstable with respect to the anion vacancy, since the barriers for return are negligible, and the Cd_{Te} and the Zn_{Te} atoms spontaneously relax into the substitutional position, Cd^{1st} and Zn^{1st} , respectively. Due to huge atomic relaxations in the C_{2v} reconstruction in the neutral charge state, the energy barrier for V_{Te}^0 is much lower than that for V_{Te}^{2+} . Significant reorientation of atomic positions diminishes diffusion barrier of V_{Te}^0 , however it is too short-range to guarantee efficiency of diffusion. The phenomenon is lacking in more well-behaved V_{Te}^{2+} .

(ii) Diffusion to the second neighbor is possible for both plane-passing and cluster-assisted mechanisms. Firstly, diffusion is more energetically demanding for ZnTe, for reasons described in Sec. 2.1.1. Secondly, cluster-assisted mechanism is less efficient like in the case of diffusion of cation vacancies. Finally, the barriers for diffusion to the second neighbor are higher by about 1 eV in the case of anion vacancy. The C_{2v} reconstruction and higher concentration of charge enhance the barriers of V_{Te}^0 , which are larger than in the 2+ charge state.

(iii) Diffusion to the fourth neighbor is possible, but prohibitively high-cost in terms of diffusion barriers. The differences between materials and dependence on the charge state can be explained using the same reasoning like above and in Sec. 2.1.1.

TABLE XI. Calculated diffusion barriers (in eV) for different diffusion mechanism and charged states of V_{Te} in CdTe and ZnTe. The values in parentheses represent diffusion barriers for the return.

	CdTe		ZnTe	
	V_{Te}^0	V_{Te}^{2+}	V_{Te}^0	V_{Te}^{2+}
First neighbor	0.20 (0.00)	1.65 (0.00)	0.25 (0.00)	1.75 (0.00)
Plane passing	1.75	1.60	2.60	1.95
Cluster assisted	2.30	2.15	2.90	2.50
Fourth neighbor	3.60	3.55	4.30	4.20

2.4 Anion interstitials

Based on the premises elucidated while considering the previous native defects, a charge neutral anion interstitial in zinc blende II-VI compounds is expected to introduce six electrons in nonbonding orbitals. In site with T_d symmetry two of them occupy the singlet a_1 that lies below VBM, and the remaining four occupy the t_2 triplet states which are expected to be in the band gap. Similar to cation interstitial, and in opposition to vacancies where the crucial defect orbitals have the host valence origin, the occupied a_1 and t_2 defect states are created from the host conduction band states. Since the t_2 orbital is partially occupied (in the neutral charge state the triplet is occupied by four electrons) anion interstitial can be deep donor as well as deep acceptor. The obtained results can be summarized as follows.

I begin with CdTe and first consider Te_i in T_d symmetry. Similar to the cation interstitial the anion interstitial can assume two nonequivalent interstitial sites with the tetrahedral symmetry, the first of which is surrounded by four anions, T:anion, and the other by four cations, T:cation (see Fig. 2.9). The energetic correspondence between the T:Te and the T:cation sites can be explained from electrostatic considerations like in Sec. 2.3 (see Fig. 2.25 and 2.26a), where representative cases can be chosen and explained:

- (i) **$Q=0$ case.** The T:Cd site in the neutral charge state is more stable than the T:Te site, because t_2 orbital is higher in energy in the case of the T:Te site.
- (ii) **$Q=3+$ case.** Depopulation of the t_2 orbital stabilizes the T:Te site because of both electrostatics, and the bigger energy gain due to the recombination of 3 electrons from higher energy level.

(iii) $Q=2-$ case. Stabilization of the T:Cd site is evidenced for the similar reasons (i.e., both electrostatics and bigger gain from population of t_2 orbital by conduction electrons).

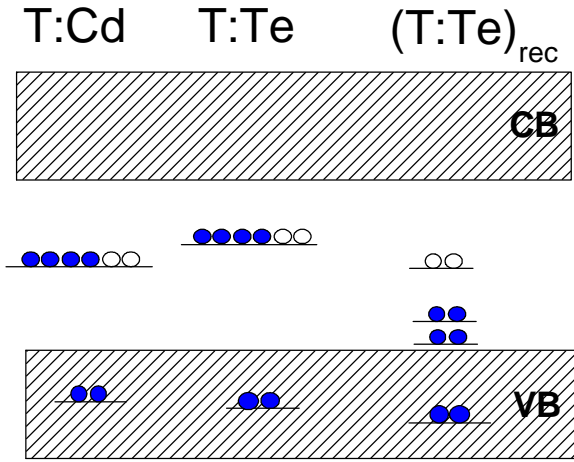


FIG 2.25. Energy levels of Te_i at the two tetrahedral sites with T_d symmetry, T:Cd and T:Te, and at the reconstructed T:Te site with C_2 symmetry, (T:Te)_{rec}.

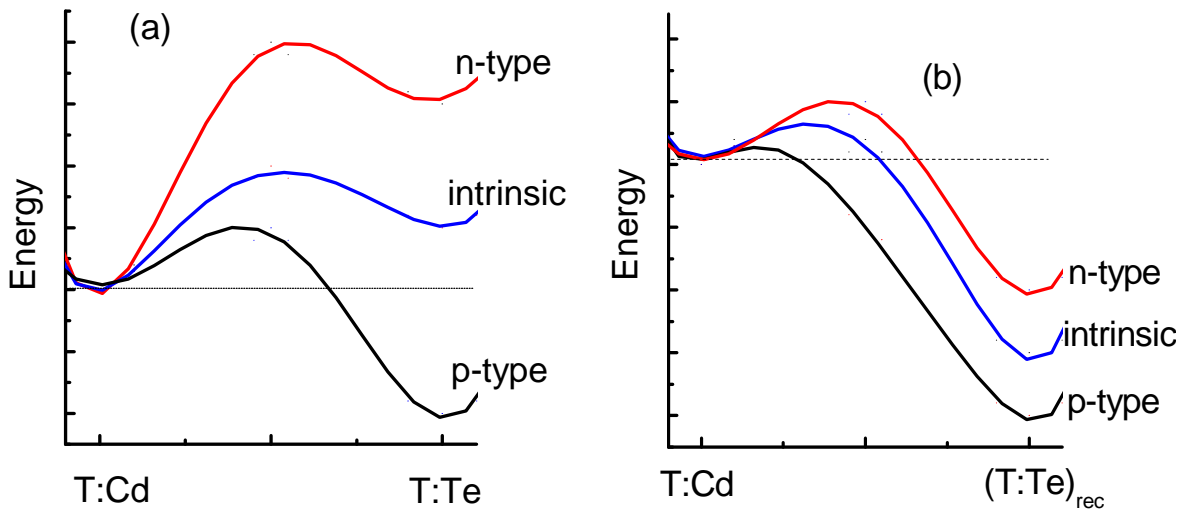


FIG. 2.26. Relative total energies of Te_i at characteristic sites with (a) T_d , and (b) C_2 symmetry.

However, for Te_i at the T:Te site, a pronounced local reconstruction occurs. This effect has not been previously recognized, and it strongly changes the energetics of Te_i (Figs. 2.25 and 2.26b).

1. First of all, because of huge symmetry lowering around the T:Te site, the reconstructed T:Te site, (T:Te)_{rec} is ground state throughout all the accessible charge states. Depending on

the charge state configuration with C_{3v} ($Q=2+$ and $3+$) and C_2 ($Q=-2, -1, 0,$ and $+1$) is ground state. In each case, the total energy of $(T:Te)_{rec}$ site is lower than that of the T:Cd site (Fig. 2.26b).

2. Moreover, the reconstruction splits t_2 triplet level, and two of the resultant singlets become shallow and close to the VBM (Figs. 2.25 and 2.27).

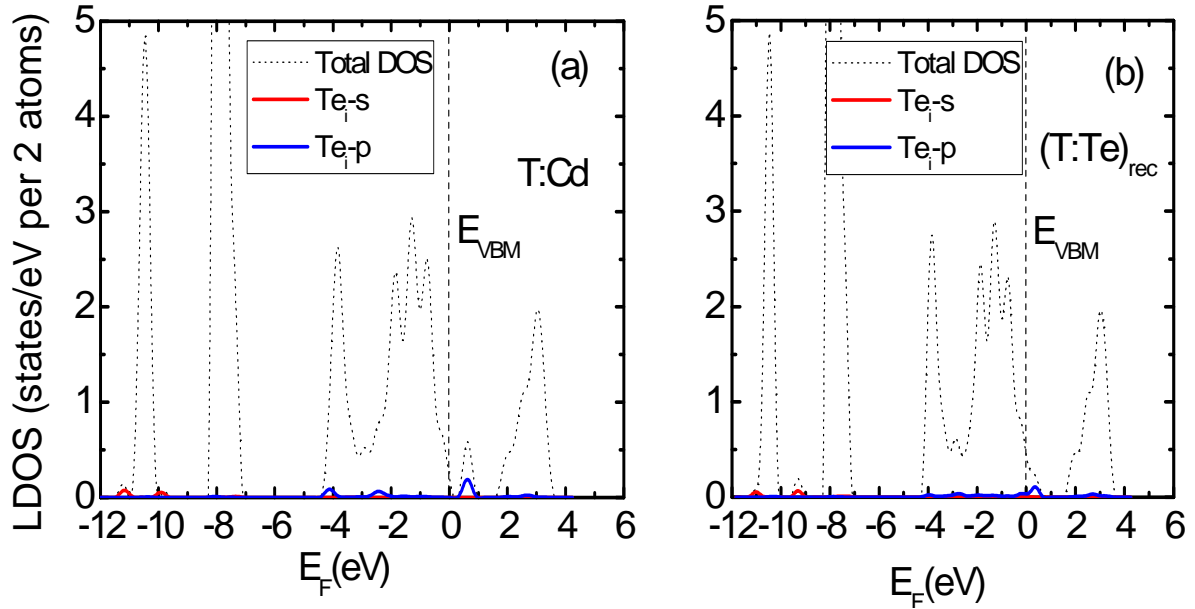


FIG. 2.27. Total DOS and LDOS of Te_i in CdTe at (a) the T:Cd and (b) the $(T:Te)_{rec}$ sites.

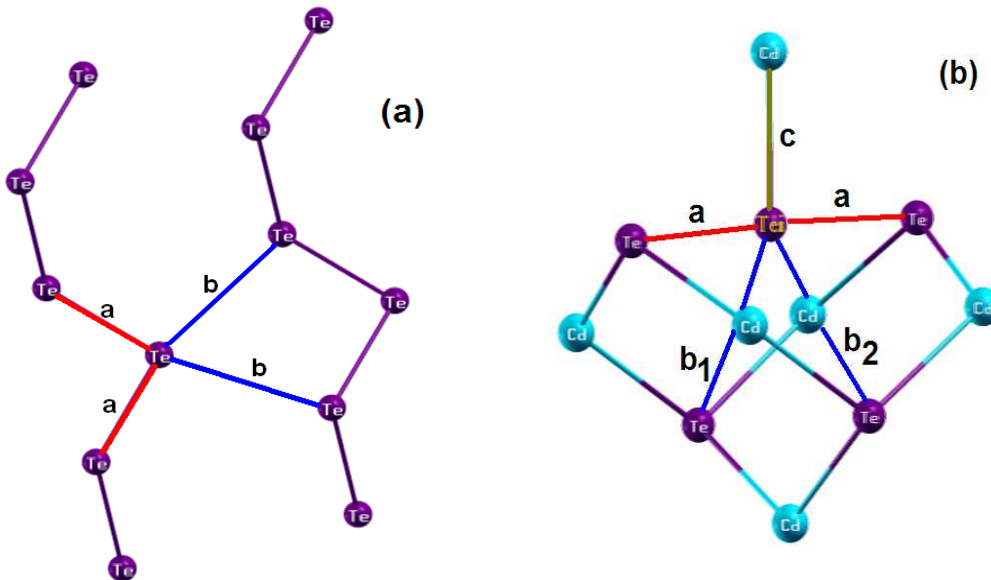


FIG. 2.28. Atomic configuration in (a) the α Se structure of elemental Te, and (b) Te_i at the $(T:Te)_{rec}$ in zinc blende CdTe.

3. Except two charge states ($Q=2+$ and $3+$) the relaxation lowers the system symmetry to C_2 , which reflects the tendency of the interstitial atom to be in the local coordination that resembles that of the α Se crystal structure (C_{2h}), which is the stable phase for the elemental Te. The geometric relations between the nearest neighbors for elemental Te and Te interstitial at the T:Te site are presented in Fig. 2.28. The corresponding distances (Table XII) prove the close resemblance of the atomic coordination between the elemental phase and Te_i at the $(T:Te)_{rec}$ site.

4. Starting from Te_i^{2+} and depopulating further, the C_{3v} symmetry configuration gives the lowest energy states. The distances between atoms are too large and the charge on the antibonding orbitals too small to stabilize the neighborhood similar to that operative in the elemental Te. The configuration where interstitial shares electrons with three Te atoms is more energetically privileged than the one employing two Te atoms. The latter is gaining advantage when at least three electrons are present in the bandgap. Actually, b_1 and b_2 bond lengths for neutral and negatively charged defects are very close to each other, the atomic configuration is very close to the local coordination of the elemental Te (Table XII). For positive charged defects, b_1 and b_2 values are significantly different from each other, and the configuration differentiates from the one characteristic of the elemental Te.

5. Stabilization of the C_2 reconstruction can be explained by the examination of $|\psi|^2$. As it is seen in Fig. 2.29b the second level derived from the split triplet has bonding nature and is directed towards two neighbor Te atoms. The lowest (Fig. 2.29a) and highest levels of this split are not directed toward Te atoms, and only partially participate in bond creation. This is the reason why occupancy of the middle level of the split triplet is so significant for the stabilization of the $(T:Te)_{rec}$ site. The antibonding character of the triplet state in the case of the T:Cd configuration is shown in Fig. 2.30. Each, out of three orbitals, reaches different pair of six Te second neighbors. The energetic equivalence of those levels is underscored comparing Figs. 2.30a and b. Charging the defect in this case alters interrelation of charge distribution between neighbors which gives rise to diverse, but systematic, changes to interatomic distances in the vicinity of the T:cation site defect (Table XII). This trends can be fully explained by the means of simple electrostatic consideration like those presented in Sec. 2.2.

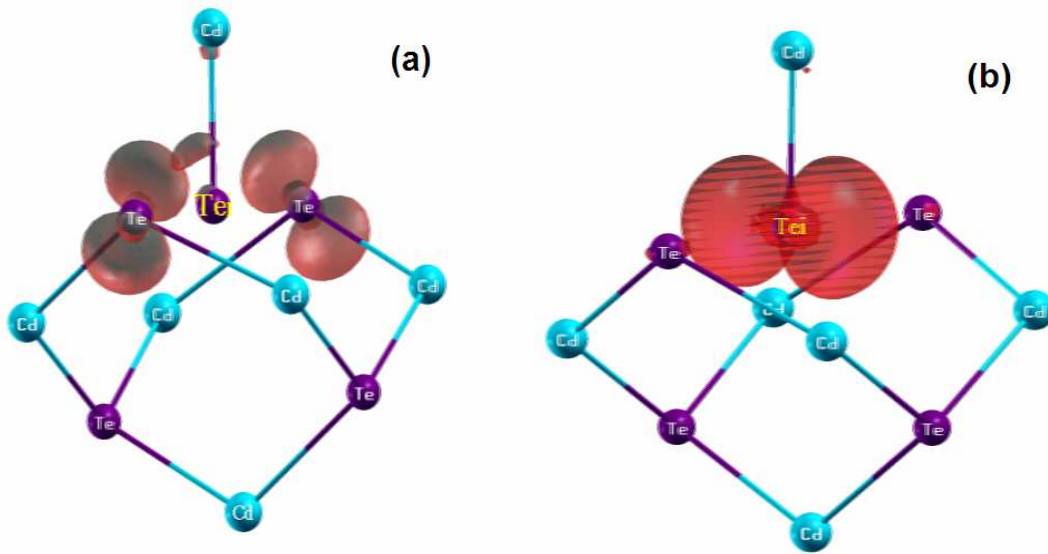


FIG. 2.29. Wave function square of the bandgap a_1 states pertinent to Te_i at the $(T:Te)_{rec}$ configuration in CdTe. (a) shows the lowest level and (b) the middle level of the split triplet of Te_i . In the neutral charge state both orbitals are fully occupied (see Fig. 2.25).

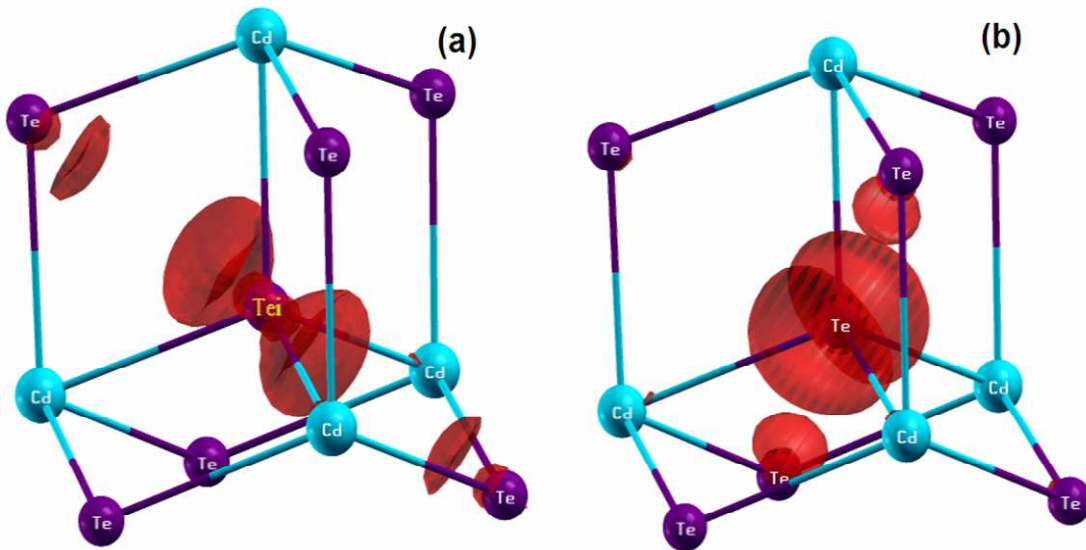


FIG. 2.30. Wave function square of the two bandgap t_2 states pertinent to Te_i at the T:Cd site in CdTe. In the neutral charge state both orbitals are fully occupied, and the third orbital, not shown here and overreaching to the remaining two second neighbor Te atoms, is empty.

TABLE XII. Energies of the triplet state t_2 (valid at the T:Cd site), singlets a_1 (at the $(T:Te)_{rec}$ site) with respect to VBM, and relaxation energies ΔE_{relax} for the neutral and charged states of Te_i in CdTe. When presenting energy of levels band gap correction ΔE_{gap} was

omitted. The distances as defined in Fig. 2.28a are listed below for the C_2 symmetry defects for the (T:Te)_{rec} configuration (denoted as Rec). For defects with C_{3v} symmetry a and b_1 represent the distance between the Te interstitial atom and three equivalent Te atoms, and the remaining fourth Te atom, respectively. The distance in the T:Cd configuration (T_d symmetry), c , depicts the distance between the Te interstitial atom and the four Cd nearest neighbor atoms. For comparison, the corresponding values for the elemental Te at the equilibrium lattice parameters of α Se crystal structure (C_{2h}), $a = 2.83$ Å, and $b = 3.67$ Å. Bond length in CdTe is 2.87 Å.

	$Te_i^0(C_2)$		$Te_i^{1+}(C_2)$		$Te_i^{2+}(C_{3v})$		$Te_i^{3+}(C_{3v})$		$Te_i^{1-}(C_2)$		$Te_i^{2-}(C_2)$	
	T:Cd	Rec	T:Cd	Rec	T:Cd	Rec	T:Cd	Rec	T:Cd	Rec	T:Cd	Rec
t_2 (eV)	0.55		0.49		0.47		0.50		0.57		0.63	
a_1 (eV)		0.08		0.04		0.02		0.01		0.08		0.08
		0.32		0.13		0.68		0.67		0.36		0.35
		0.68		0.68		1.05		1.06		0.68		0.67
a (Å)		2.97		2.92		2.97		2.93		2.98		2.98
b_1 (Å)		3.85		3.65		4.12		4.04		3.85		3.85
b_2 (Å)		3.89		4.18						3.89		3.89
c (Å)	2.96	2.69	3.02	2.77	3.11		3.23		2.88	2.69	2.83	2.70
ΔE_{relax} (eV)	0.80	2.34	0.83	2.44	0.87	2.03	0.94	2.09	0.69	2.21	0.76	2.27

TABLE XIII. Energies of the triplet state t_2 (valid at the T:Zn site), singlets a_1 (at the (T:Te)_{rec} site) with respect to VBM, and relaxation energies ΔE_{relax} for neutral and charged states of Te_i in ZnTe. When presenting energy of levels band gap correction ΔE_{gap} was omitted. The distances as defined in Fig. 2.28a are listed below for the (T:Te)_{rec} configuration (denoted as Rec). The distance in the T:Zn configuration (T_d), c , depicts the distance between the Te interstitial atom and the four Zn nearest neighbor atoms. For comparison, the corresponding values for the elemental Te at the equilibrium lattice parameters of α Se crystal structure (C_{2h}), $a = 2.83$ Å, and $b = 3.67$ Å. The bond length in ZnTe is 2.69 Å.

	$Te_i^0(C_2)$		$Te_i^{1+}(C_2)$		$Te_i^{2+}(C_2)$		$Te_i^{3+}(C_2)$		$Te_i^{1-}(C_2)$		$Te_i^{2-}(C_2)$	
	T:Cd	Rec	T:Cd	Rec	T:Cd	Rec	T:Cd	Rec	T:Cd	Rec	T:Cd	Rec
t_2 (eV)	0.55		0.54		0.53		0.51		0.59		0.62	
a_1 (eV)		0.11		0.02		0.03		0.03		0.11		0.12
		0.29		0.13		0.56		0.52		0.29		0.28
		1.10		1.12		1.13		1.15		1.09		1.11
a (Å)		2.91		2.88		2.84		2.84		2.91		2.91
b_1 (Å)		3.62		3.57		3.84		3.83		3.70		3.71
b_1 (Å)		3.71		4.09		4.86		4.85		3.65		3.67
c (Å)	2.73	2.50	2.81	2.54	2.88	2.58	2.96	2.58	2.68	2.50	2.62	2.50
ΔE_{relax} (eV)	0.92	2.41	1.01	2.60	1.14	2.55	1.22	2.49	0.79	2.32	0.86	2.37

6. The formation energy of Te_i in CdTe is presented in Figs. 2.23. The defect has only acceptor-like character in CdTe. The formation energies are especially low in the p-type regime. Te_i can pin the Fermi energy close to VBM, similar to cation interstitials. In n-type samples, formation energies are high. Finally, the formation energies of Te_i in both T:Te and T:Cd sites were calculated in Ref. 39 and agree with my results within 0.3 eV. However, these authors did not recognize the possibility of the low-energy reconstructed configuration at the T:Te site.

Te_i in ZnTe is qualitatively similar to the results of anion interstitial in CdTe. Huge symmetry lowering around the T:Te site, $(\text{T:Te})_{\text{rec}}$ is ground state throughout all the accessible charge states except in 2- charge state. The resemblance of atomic coordination to the elemental Te configuration is more pronounced for ZnTe, which has smaller lattice constant than CdTe and the corresponding interatomic distances are closer to those in the elemental phase of Te (Table XIII). As a consequence, for all charge states of Te_i in ZnTe, the C_2 symmetry is the ground state. The formation energy is higher than in CdTe (cp. Figs. 2.23 and 2.24) for the reasons previously elucidated. Due to the bigger bandgap, which favors the stabilization of negatively charge states, Te_i in ZnTe is amphoteric.

The tendency to have similar atomic surrounding like in the elemental phase is also present for O and N interstitials (which forms O_2 and N_2 molecules in the solids [54]) in compounds where these atoms act as anions. In the case of O and N, the propensity to form molecules instead of isolated interstitials can be explained by huge energy gain coming from formation of the molecules compared to the matrix bond gain. The anion atoms are more susceptible to reorganize themselves than cations, not only because of smaller size, but also because of ionicity-originated charge transfer. Because of the additional charge located on them, they can participate in new bond creation needed if the new surrounding is to be created. Furthermore, the cation atoms deprived of charge due to ionic charge transfer constitute themselves less demanding obstacle during atomic displacements and the relaxation can be more effective and pronounced. In the case of CdTe and ZnTe the discrepancies between compound constituents are not so significant like for ZnO or GaN, whereas they are also conducive to the formation of new local surrounding resembling that characteristic of the ground state elemental phase of the anion.

2.4.1 Diffusion of anion interstitials

Due to the stabilization of the $(\text{T:Te})_{\text{rec}}$ configuration throughout almost all accessible Fermi level energies, the diffusion undergoes only approximately along $-\text{T:Te}-\text{T:Cd}-\text{T:Te}$ -path shown in Fig. 2.9 like for $2+$ charged cation interstitials (Sec. 3.2.3). The difference here is that the $(\text{T:Te})_{\text{rec}}$ is the ground state relaxed configuration. Thus, the diffusion occurs by long and curvilinear jumps between two adjacent $(\text{T:Te})_{\text{rec}}$ sites with T:Cd or T:Zn site corresponding usually to the maximum of the energy barrier. The details of the diffusion and barrier heights in both CdTe and ZnTe are presented in Table XIV. Practically, for all positively charged and neutral states, the diffusion occurs as stated above. For negatively charged states, the T:cation site ceases to be the maximum of the energy barrier and manifests a non-negligible metastability with $(\text{T:Te})_{\text{rec}}$ configuration still acting like a ground state. Generally, the diffusion in ZnTe is more energetically demanding than in CdTe like in the previously considered defects and for the same reasons. To the best knowledge of the author no prior publications addressed diffusion of anion interstitials in CdTe and ZnTe.

TABLE XIV. Calculated diffusion barriers (in eV) for different configurations and charge states of anion interstitials in CdTe and ZnTe. T:c denotes the T:Cd and the T:Zn site depending whether the interstitial is considered in CdTe or ZnTe, respectively. $(\text{T:Te})_{\text{rec}}$ represents the reconstructed T:Te site configuration (see text for more details).

Path	Charge State	Barriers	
		CdTe	ZnTe
$(\text{T:Te})_{\text{rec}}-\text{T:c}$	2-	0.0	0.0
$\text{T:c}-(\text{T:Te})_{\text{rec}}$	2-	0.3	0.4
$(\text{T:Te})_{\text{rec}}-\text{T:c}$	1-	0.7	0.7
$\text{T:c}-(\text{T:Te})_{\text{rec}}$	1-	0.1	0.1
$(\text{T:Te})_{\text{rec}}-\text{T:c}$	0	1.3	1.6
$\text{T:c}-(\text{T:Te})_{\text{rec}}$	0	0.1	0.0
$(\text{T:Te})_{\text{rec}}-\text{T:c}$	+	1.0	1.3
$\text{T:c}-(\text{T:Te})_{\text{rec}}$	+	0.0	0.0
$(\text{T:Te})_{\text{rec}}-\text{T:c}$	2+	0.8	1.0
$\text{T:c}-(\text{T:Te})_{\text{rec}}$	2+	0.0	0.0
$(\text{T:Te})_{\text{rec}}-\text{T:c}$	3+	0.4	0.6
$\text{T:c}-(\text{T:Te})_{\text{rec}}$	3+	0.0	0.2

2.5 Compensation of doping by vacancies and interstitials

As it follows from Figs. 2.3, 2.4, 2.23, and 2.24 and Eq. (1.1), formation energies of defects depend on the Fermi level and growth conditions embedded in chemical potentials of the relevant atomic species. In particular, E_{form} of cation vacancies in both CdTe and ZnTe decreases with the increasing Fermi energy, and assumes very low values when E_F approaches the bottom of the conduction band. Therefore, because of their acceptor character, V_{Cd} and V_{Zn} are the dominant native acceptors that compensate p-type doping, and they set up an intrinsic limit on the possible n-type doping of both CdTe and ZnTe. This tendency is weaker when the growth occurs under cation-rich conditions, when formation energies of both V_{Cd} and V_{Zn} are higher. Finally, formation energies are lower in ZnTe than in CdTe, which explains bigger difficulties with obtaining n-ZnTe than n-CdTe [55].

Cation and anion interstitials are the dominant intrinsic donors that compensate p-type doping, which follows from their very low formation energies for low values of the Fermi energy. It is difficult to eradicate the p-type compensation, because the effects of any growth regime are counterproductive from the point of view of those two types of interstitials. For instance as the growth is carried out under Te-rich conditions it alleviates the detrimental effect coming from cation interstitial (i.e. moves pinning energy toward VBM) and simultaneously aggravates the situation in the context of anion interstitial (the pinning energy is moving higher in the bandgap). Because of higher formation energies of interstitials in ZnTe than in CdTe, less limits for p-type doping exist in the latter compound, again in agreement with experiment [55].

Anion vacancy acts as a donor in both CdTe and ZnTe, but is not expected to have a dominant role in compensation of p-type doping mainly due to its high formation energy.

Chapter 3

Frenkel pairs in CdZnTe

A nearest-neighbor vacancy-interstitial Frenkel pair (FP) is created by displacing an atom from the substitutional site along the [111] direction. In the final configuration the interstitial is displaced by about 6 Å from its initial position. In this Chapter, I analyze this process for both cation and anion sublattice, beginning with the former case. Next, the cation sublattice FPs are employed to explain the electric polarization and the resistive switching observed in CdZnTe. I propose a microscopic model of bistability which is extended further to CdZnMnTe alloys. In most cases FPs are metastable, since there are finite energy barriers for the return of the interstitial atom to the substitutional site, i.e., for the defect recombination. The stability of FPs is also investigated from the point of view of dissociation that can ensue from the diffusion of the constituents of FP.

3.1 Cation sublattice

In this case, a cation, displaced from the substitutional equilibrium position along the [111] direction, is close to the T:Te site, see Fig. 3.1. Changes in the total energy corresponding to the formation of cation FPs (c-FPs) in CdTe and ZnTe are shown in Figs. 3.2 and 3.3. The calculated barriers are given in Table XV. The results show that generation scheme and characteristics of FPs are very similar in CdTe and ZnTe. The most characteristic feature is the strong dependence of energy barriers and stability of FPs on the complex's charge state that I now discuss.

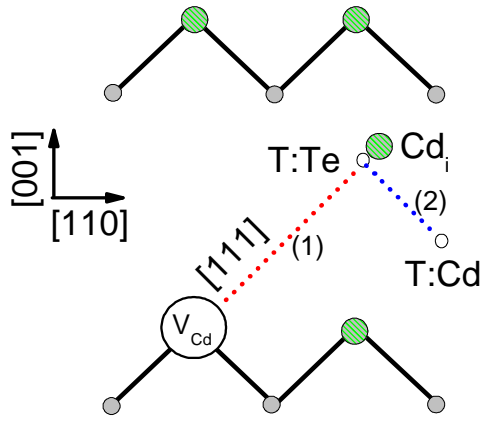


FIG. 3.1. Schematic representation of atomic positions of c-FP in the (110) plane of zinc blende CdTe. The large green circles represent Cd atoms, medium grey circles Te atoms. The high-symmetry tetrahedral interstitial sites are indicated by T:Cd and T:Te. The red short dotted line (1) indicate direction of displacement to generate c-FP. The blue short dotted line (2) represent the path, out of three equivalent ones, for out-diffusion of Cd_i .

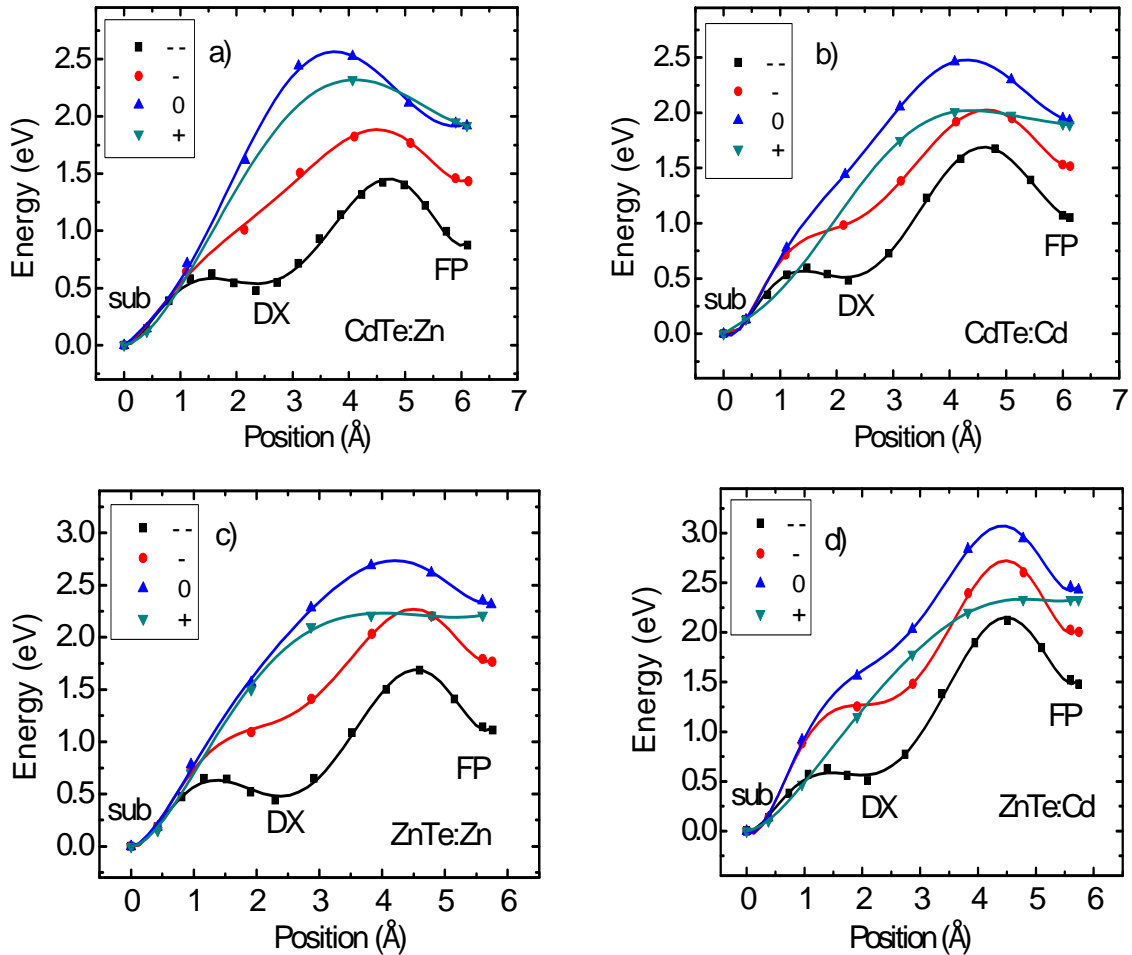


FIG. 3.2. Total energy change corresponding to a creation of (a) $V_{Cd} + Zn_i$, and (b) $V_{Cd} + Cd_i$ FPs in CdTe, and (c) $V_{Zn} + Zn_i$, and (d) $V_{Zn} + Cd_i$ FPs in ZnTe as a function of the distance from the substitutional site (sub) for 4 charge states. In 2- charge state DX configuration is metastable.

TABLE XV. Calculated barriers for generation (sub-FP) and recombination (FP-sub) (in eV) of c-FPs in CdTe and ZnTe for different configurations and charge states.

Path	Charge State	Barriers			
		CdTe: Cd	CdTe: Zn	ZnTe: Cd	ZnTe: Zn
sub-FP	0	2.45	2.55	2.95	2.70
FP-sub	0	0.55	0.60	0.50	0.40
sub-FP	-	1.95	1.80	2.60	2.20
FP-sub	-	0.45	0.40	0.60	0.45
sub- <i>DX</i>	2-	0.60	0.60	0.60	0.65
<i>DX</i> -FP	2-	1.20	0.95	1.60	1.25
FP- <i>DX</i>	2-	0.60	0.55	0.65	0.60
<i>DX</i> -sub	2-	0.10	0.15	0.10	0.20
sub-FP	+	2.00	2.30	2.35	2.20
FP-sub	+	0.10	0.45	0.00	0.00

(i) $Q=0$ case. In intrinsic samples, the energy barriers are 2.5-3.0 eV. The final configuration of the nearest-neighbor $V-I$ pair is relatively stable, since the calculated energy barriers for recombination are about 0.5 eV.

(ii) $Q=-2$ case. In n-type samples, after capturing 2 electrons the FP is in the 2- charge state. Figure 3.3 summarizes the results for the four considered FPs. The $Q=-2$ case is qualitatively different from the remaining charge states because formation of the FP is preceded by stabilization of a *DX*-like configuration, in which the interstitial-vacancy separation is 2.3-2.5 Å. This configuration corresponds to the local energy minima in Figs. 3.2 and 3.3. The barriers to form the *DX* centers are relatively low, 0.60-0.65 eV, see Table XV, and their energies are higher than the ground state by about 0.5 eV. Although barriers for recombination are low, about 0.2 eV, the metastability is clearly seen. The calculated metastability of $V_{Cd} + Cd_i$ pairs in CdTe in the *DX* configuration confirms the results of Lany *et al.* [56] Since in Ref. 56 the values of energies and barriers are not given, a detailed comparison is not possible.

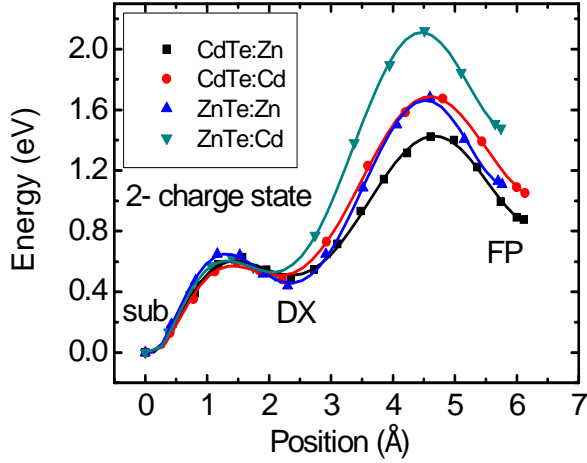


FIG. 3.3. Total energy change corresponding to a creation of c-FP in the 2- charge state.

Formation of FPs is realized as a result of larger displacements of about 6 Å. The process of formation may occur either in two steps, i.e., with the *DX* configuration mediating the transition to the final FP geometry, or in one large hop. The former possibility involves overcoming two consecutive barriers that are relatively low, while the latter case involves larger barriers of about 1.5 eV. A detailed evaluation of the relative efficiencies of both paths is outside the scope of this dissertation. However, Fig. 3.2 shows that in both cases the energy barriers are substantially reduced with respect to the $Q=0$ values. The barriers for defect recombination for all cases are about 0.5 eV, which implies a stability of 2- charged FPs.

The obtained results, i.e., the metastability of the complex and the increased efficiency of FP generation in the presence of excess electrons, are similar to the features characterizing both *DX* centers and the *EL2* defect in GaAs [57, 58]. This similarity stems from the common physical origin: a large displacement of an impurity, or of a host atom, from the substitutional site induces a deep level in the gap, which energy decreases with the increasing displacement and relaxation. This in turn induces a decrease of the total energy and the stabilization of the *DX* configuration when the band gap state is occupied with 2 electrons in the 2- charge state. In the real space, the wave function of the deep state is localized on the broken bond [57], and thus the occupation of this state by electrons corresponds to a passivation of the broken bond created by formation of the complex. However, we note that *DX* centers are less stable than FPs: while the *DX* configuration is metastable only in the 2- charge state (and thus is unstable after optical emission of an electron, or its recombination with free holes), FPs are metastable in the $Q = -1, 0$, or even $Q = +1$ charge states, see (iv) below, and the relevant barriers are higher.

(iii) $Q=-1$ case. In the intermediate case of the 1- charge state, (i.e., when one additional electron is captured by the complex), barriers are also intermediate between those for $Q=0$ and $Q=-2$, i.e., about 2 eV. The total energy curves display a non-linear dependence on the $V-I$ separation, indicating the tendency to stabilize the DX configuration in the 2- state.

(iv) $Q=+1$ case. Energy required to form a FP in p-type sample is very similar to that for the $Q=0$ case. However, the barriers for recombination in CdTe are reduced for $V_{Cd} + Cd_i$, and they even vanish in ZnTe. This means that in p-type samples the nearest-neighbor FPs have a lowered stability in CdTe, and are not stable in ZnTe.

Moreover, as it follows from Figs. 3.2 and 3.3, the properties of the $V_{Cd} + Zn_i$ in $Cd_{0.97}Zn_{0.03}Te$ differ from those of the remaining cases. First, the generation energy of the pair in the 2- state, 1.4 eV, is the smallest. In other cases it amounts to about 1.8 eV, implying a less efficient generation (since the generation probability depends exponentially on the barrier height, the difference of 0.2 eV in the barriers leads to a difference of three orders of magnitude in generation efficiency between them, assuming the same generation temperature of 300 K). Second, this is the only FP expected to be stable for charge states from 1+ to 3-. These results are significant in the context of experimental data discussed further in Sec. 3.3.

Finally, it is interesting to investigate the Fermi energy dependence on the barriers' height from the point of view of a net change in charge distribution when an additional electron or hole is introduced (Fig. 3.4). The same approach was employed while considering the influence of charge on the efficiency of diffusion of vacancies (Secs. 2.1.1 and 2.3.1). The addition of an electron gives rise to a decrease in a net charge around three Cd atoms (Fig 3.4b) which constitute barrier while the interstitial is intersecting and passing the plane composed of these atoms. This facilitates the diffusion and lowers the barrier height. Furthermore, a decrease in a net charge around the Te atoms is experienced which enable the Cd-Te bond fracture. In effect, it facilitates the displacement of cation atom along the [111] direction. Upon addition of a hole, bonds around Te atoms get softened (Fig. 3.4a), i.e., there is an outflow of the total charge from these areas. That is why p-type doping does not affect substantially the barrier height for generation of a c-FP but simultaneously diminishes the metastability by means of enhancing the recombination (cation interstitial in a metastable c-FP is surrounded by Te nearest neighbors). The changes in c-FP barriers are also influenced by a change in charging of its constituents. Both cation vacancy and cation interstitial introduce levels in the bandgap, i.e., both levels are electrically active and can accommodate

changes in net charge which can furthermore influence intrapair electrostatic interaction (more details below).

Summarizing this part, the simple general picture of dependence of barrier heights on the c-FP charge emerges. Generation barriers are determined by the interplay of the interstitial of c-FP and the three cation atoms. In covalent-ionic CdTe and ZnTe, three cation atoms that form a plane, which is to be surmounted and passed by the interstitial in order to generate c-FP, are positively charged. Thus, additional electrons on the interstitial facilitate generation of c-FP. On the other hand, the c-FP is stabilized by four Te atoms, which are negatively charged, and electrostatic interplay between surrounding Te atoms and the interstitial determine recombination barriers. In this case, positively charged c-FP enhances recombination barriers, and thus also stability of c-FP.

Formation of $V-I$ pairs on the cation sublattice in GaAs, CdTe, and NaCl has been considered by Wei *et al.* [59] who used unit cells containing from 4 to 16 atoms. These cells are too small for a correct description of energetics of FPs, which are relatively extended defects. Actually, these cells have lateral dimensions close to the equilibrium distance between vacancy and interstitial, $\sim 6 \text{ \AA}$. One may only note that the calculated energy increase of $\sim 1.75 \text{ eV}$ for displacements of $\sim 2.25 \text{ \AA}$ of neutral Cd or Zn from ideal sites in CdTe in Ref. 59 is similar to the results of Fig. 3.2.

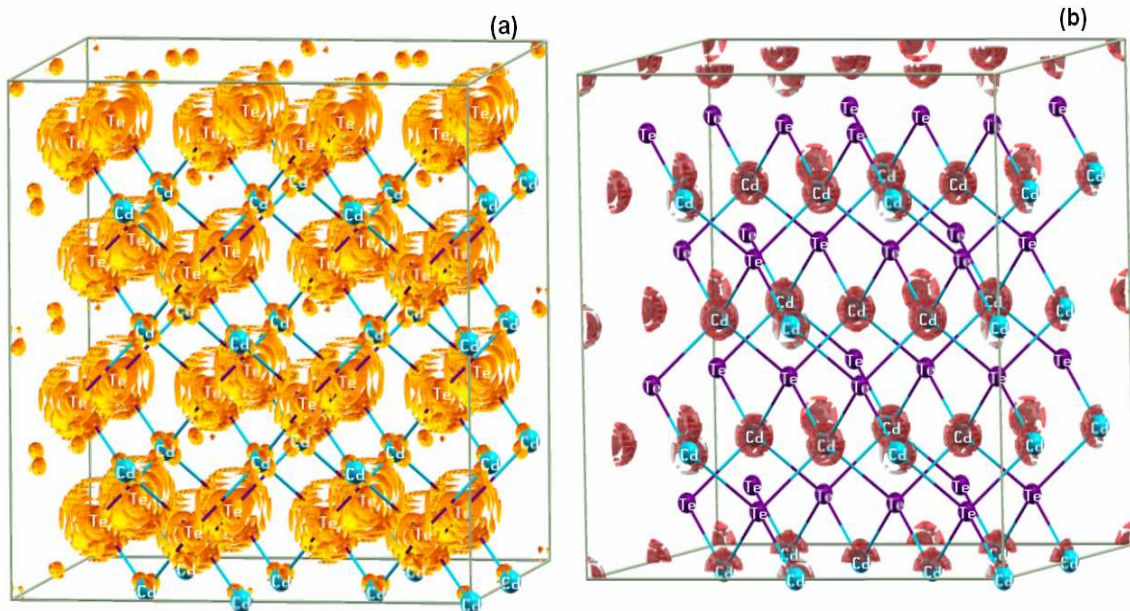


FIG. 3.4. Difference between (a) 1+ and neutral charge states, and (b) 1- and neutral charge states for CdTe, which reflect the wave function of (a) a hole, and (b) an electron. The (a) and (b) isosurfaces respectively correspond to charge densities of 0.001 e\AA^{-3} and -0.002 e\AA^{-3} . It means that upon adding a hole (a) and an electron (b) the respective isosurface represents a

decrease in the total charge density. In the case of both neutral and charged state the same atomic coordinates were employed.

Formation energy of a FP is given by Eq. (1.1), and can be expressed as:

$$E_{\text{form}}(V + I) = E_{\text{form}}(V^0) + E_{\text{form}}(I^0) + E^{\text{int}}(V + I) + E^{\text{ord}}(V + I). \quad (3.1)$$

Here, $E_{\text{form}}(V^0) + E_{\text{form}}(I^0)$ is the sum of formation energies of a neutral and isolated vacancy and interstitial. $E^{\text{int}}(V + I)$ is the interaction energy when V and I are next to each other and form a FP. Finally, in the supercell method, creation of a defect (or of a defect pair) in the unit cell corresponds to formation of an infinite and ordered array of defects that may interact. In the case under study, V - I pairs are electric dipoles that interact by Coulomb forces. The corresponding interaction energy is denoted by $E^{\text{ord}}(V + I)$. In a simple model assuming that the V - I pairs are [111]-oriented and localized dipoles, $E^{\text{ord}}(V + I)$ vanishes due to the fact that the supercell is simple cubic. In this case, the dipoles are parallel-ordered. It should be underlined that this configuration is a ground state, i.e., the dipoles that align in parallel are energetically privileged. Other configurations increase the dipole-dipole interaction between FPs from different supercells. This fact was checked using 254-atom supercell calculations where two variously orientated FPs were introduced and parallel alignment was lower in energy by at least 0.15 eV than other configurations. This difference increases with the decreasing distance between FPs, i.e. with the decreasing size of the supercell. The dependence on the chemical potentials is negligible because the calculated heat of formation for CdTe and ZnTe are the same to within 0.01 eV, see the discussion in Chapter 1.

There are three potential contributions to the interaction energy E^{int} of a neutral V - I pair, namely:

1. Charge transfer of two electrons from the donor (interstitial) to the acceptor (vacancy). After the charge transfer both the vacancy and the interstitial become charged, and a V - I donor-acceptor pair generates a dipole-like electric field. This occurs in spite of the fact that the pair is *neutral*, i.e., it does not exchange electrons with donors or acceptors possibly present in the sample.
2. The Coulomb attraction between charge defects that is created after charge transfer.

3. The atomic relaxation around the pair that is greater than the superposition of isolated defects relaxation.

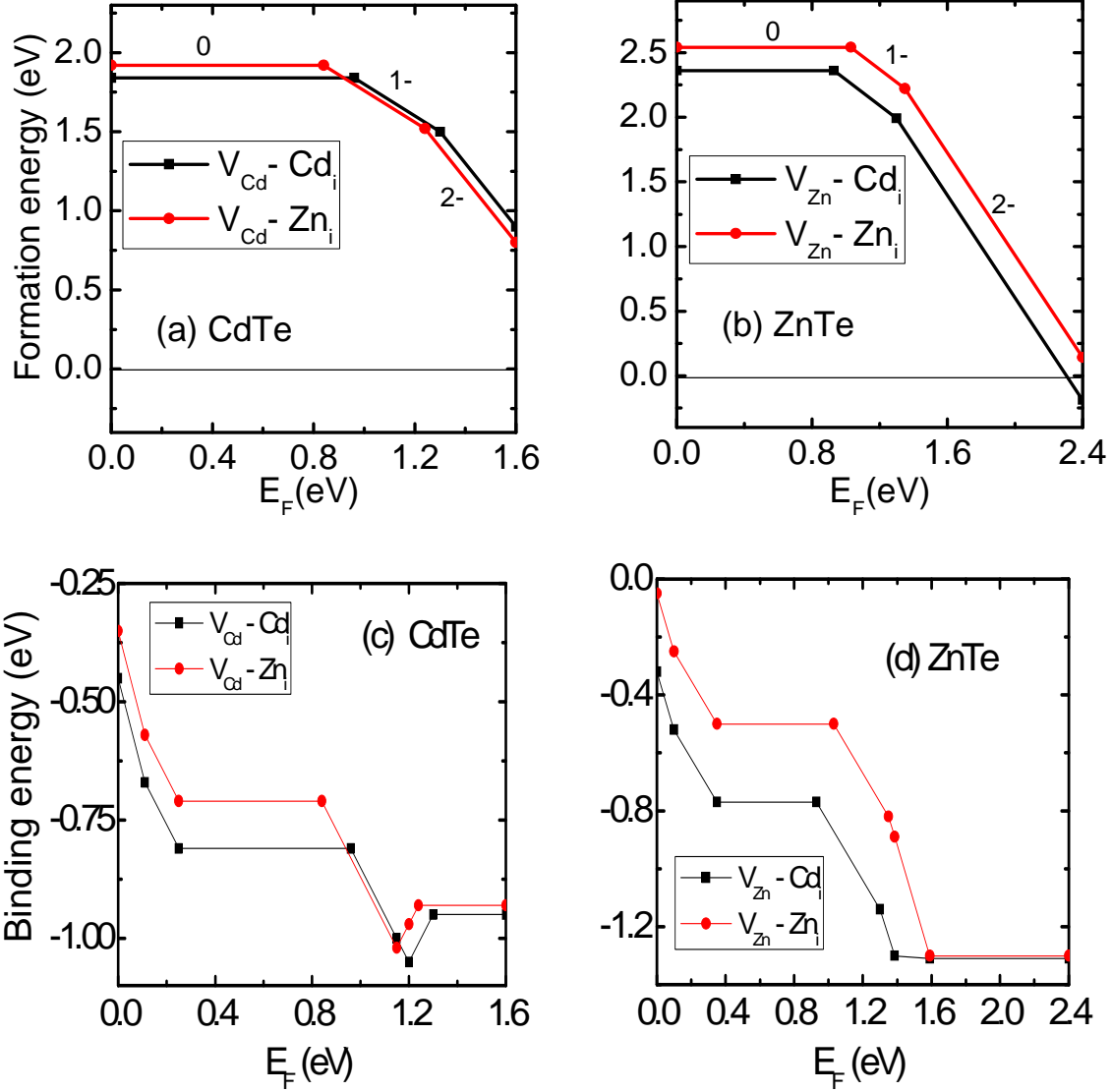


FIG. 3.5. Calculated dependencies on the Fermi energy of (a) formation energies $V_{\text{Cd}} + \text{Cd}_i$ and $V_{\text{Cd}} + \text{Zn}_i$ in CdTe and (b) $V_{\text{Zn}} + \text{Cd}_i$ and $V_{\text{Zn}} + \text{Zn}_i$ in ZnTe, and of the binding energies of FPs in (c) CdTe and (d) ZnTe.

As it stems from Table XVI, E^{int} ranges from -2.65 to -3.5 eV. In particular, for $V_{\text{Cd}}^{2-} + \text{Zn}_i^{2+}$, $E^{\text{int}} = -2.65$ eV, which decomposed onto the abovementioned contributions:

- (1) The main contribution, -2.1 eV, which is provided by transfer of two electrons from Zn_i to V_{Cd} orbitals (the value is obtained by comparison of the band gap levels of the constituent defects).

(2) Electrostatic attraction between the charged defects contributes -0.75 eV. In fact, after the transfer of two electrons from the interstitial to the V , both defects are charged, which gives rise the Coulomb attraction between them. More precisely, the gap state of the vacancy is occupied with two electrons that are transferred from the gap state of the interstitial. The value of the coupling was found by direct integration using the calculated wave functions of the vacancy and the interstitial. This value is lower than -1 eV obtained within a commonly used scheme that assumes two point charges located at the V and I sites, since the actual charge densities are delocalized. One may notice that in the considered case the transfer of two electrons is possible because the vacancy state is shallow and extended, and thus the intracenter Coulomb U interaction is small. The above procedure of integrating is valid because negative-feedback charge regulation [60, see also Sec.3.2] is not working here. Charging of the levels of both vacancy and interstitial does not alter the character of bonding and antibonding levels, and thus electron charging leads to a change in net charge of both constituent defects that is comparable to a change in charge of orbitals they introduce in the bandgap, and which are accordingly populated or depopulated upon the charging. It is not the case in anion vacancy – see a-FP below for thorough discussion.

(3) lattice relaxation (compared to relaxation of isolated defects that constitute a given FP) upon pairing gives +0.2 eV. This value is obtained by subtracting the values (1) and (2) from E^{int} and the positive value reflects that the relaxation of constituents in a pair is smaller in comparison to relaxation of isolated constituents. Consequently, formation energies of neutral V - I pairs drop to about 1.9 eV in CdTe and to about 2.5 eV in ZnTe, see Table XVI and Fig. 35.

TABLE XVI. The calculated formation energies $E_{\text{form}}(V^0) + E_{\text{form}}(I^0)$ (in eV) of noninteracting neutral defects and the intrapair interaction energies $E^{\text{int}}(V + I)$. Calculated transition energies, $\varepsilon(0/-)$ and $\varepsilon(-/-/-)$, in eV for the FP in CdTe and ZnTe are without M-P correction. The values obtained when including the image charge correction (cf. Chapter 1) are given in parentheses.

	$V_{\text{Cd}}^0 + \text{Cd}_i^0$	$V_{\text{Cd}}^0 + \text{Zn}_i^0$	$V_{\text{Zn}}^0 + \text{Cd}_i^0$	$V_{\text{Zn}}^0 + \text{Zn}_i^0$
$E_{\text{form}}(A^0) + E_{\text{form}}(B^0)$	4.69	4.57	5.77	5.45
$E^{\text{int}}(A + B)$	- 2.85	- 2.65	- 3.23	- 3.09
$E_{\text{form}}(A + B)$	1.84	1.92	2.54	2.36
$\varepsilon(0/-)$	0.96 (1.07)	0.84 (0.95)	1.03 (1.16)	0.93 (1.06)
$\varepsilon(-/-/-)$	1.30 (CBM+0.03)	1.24 (1.57)	1.35 (1.74)	1.30 (1.69)

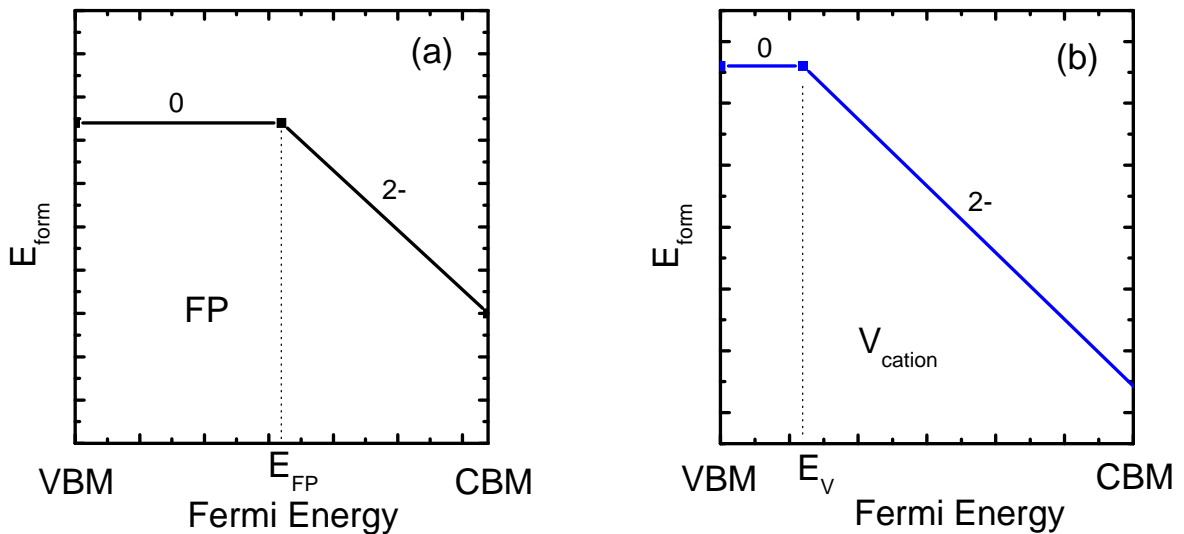
In both CdTe and ZnTe, a FP induces a deep mid-gap singlet, reminiscent of the singlet induced by an isolated interstitial (Sec. 2.2). This state is empty in the case of a neutral FP, and occupied with 1 or 2 electrons for sufficiently high Fermi level. Transition energies between the three charge states are listed in Table XVI. The dependence of formation energies on E_F is presented in Figs. 3.5a and 3.5b. E_{form} for different charge states is calculated using Eq. (1.1). For higher E_F we see a reduction of E_{form} , which reflects the acceptor-like character of a FP. As it follows from Figs. 3.5a and 3.5b, E_{form} can be reduced to 0.75 eV in CdTe and nearly zero for ZnTe as E_F approaches CBM. At first sight, it is in contradiction to the results shown in Fig. 3.2 and Table XV. Formation energies for 2- are about 1 eV higher there than for $E_F = \text{CBM}$ in Fig. 3.5. The reason for this “discrepancy” is that in Fig. 3.2 E_F is pinned to the doubly occupied singlet level that is positioned below CBM. In Fig. 3.5 we take into consideration the fact that reservoir of electrons can vary from VBM to CBM. This can be true if other sources of doping except FPs are present in the system. If E_F is higher in energy than the doubly occupied singlet, and the center acts like an acceptor, then additional energy that equals twice this difference (there can be two electrons on the singlet) is gained by the system. This additional energy gain is taken into account in Fig. 3.5, but not in Fig. 3.2, which implicitly assumes that the Fermi energy coincides with the energy of the gap state of the interstitial. The lowering is more pronounced in ZnTe than in CdTe as the energy difference between the singlet and CBM is larger due to larger bandgap. Considering the FP geometry, the close proximity of defects in the complex and the electrostatic coupling between them lower the distance between V and I by 0.4 Å in CdTe and 0.12 Å in ZnTe relative to the ideal configuration. Lowering of the local symmetry from T_d to C_{3v} weakly splits the triplet level of the vacancy into a doublet and a singlet by about 20-30 meV. The cation vacancy in a FP is a deeper defect compared to the isolated case. This due to the fact that as a constituent of a FP cation vacancy cannot fully relax like an isolated one. The energy levels of vacancy in FP are about 0.2 eV higher in energy than those in the same charge state of the isolated vacancy. This suggests that cation vacancy in a FP is no longer an efficient acceptor level, since its ionization energy is higher.

The interaction energy E^{int} introduced in Eq. (3.1) includes the energy gain of charge transfer between I and V , because the reference (i.e., initial) energy is that of the isolated and *neutral* V and I . However, it is more natural to define the binding energy E_{bind} of a FP as the energy gain due to formation of a FP from isolated V and I for a given Fermi energy, when the defects are in their appropriate charge states:

$$E_{\text{bind}} = E_{\text{form}}[V - I] - E_{\text{form}}[V] - E_{\text{form}}[I] \quad (3.2)$$

The binding energy E_{bind} includes not only the Coulomb coupling and changes in the local lattice relaxation, but also the electronic structure of the defects. The calculated binding energies shown in Figs. 3.5c and 3.5d display a relatively complex dependence on E_{F} , because this is E_{F} that determines the charge states of V , I , and the FP, and thus the effective coupling.

The dependence of E_{bind} on the Fermi level is schematically explained in Fig. 3.6. According to Eq. (3.2), E_{bind} is defined by the difference of formation energies of a FP relative to that of the isolated V and I , which are sketched in Figs. 3.6 a-c. For the sake of transparency the intracenter Coulomb interactions are neglected, and thus V may assume only the 2- and 0 charge states, and both I and the FP are in the 0 and 2- charged states. The dependence of E_{bind} on E_{F} , Fig. 3.6d, stems from the relative positions of the levels of the defects. The possible values of E_{F} span the band gap, and are split into four segments bound by the values of E_{F} at which one of the defects changes its charge state. The respective charge states are shown in Fig. 3.6e. In particular, the region B corresponds to the case of an intrinsic sample, when V and I are in the 2- and 2+ charge states, respectively. For higher E_{F} , in the segment C, formation of the FP lowers the total energy because the (occupied) level of the FP is lower than that of the isolated I . In the opposite case the total energy would rise. Similarly, the segment A can be explained in terms of the deeper vacancy levels in a FP in contrast to isolated vacancy. The changes of E_{F} in the segment D does not influence binding energy because all accessible levels of a FP are occupied.



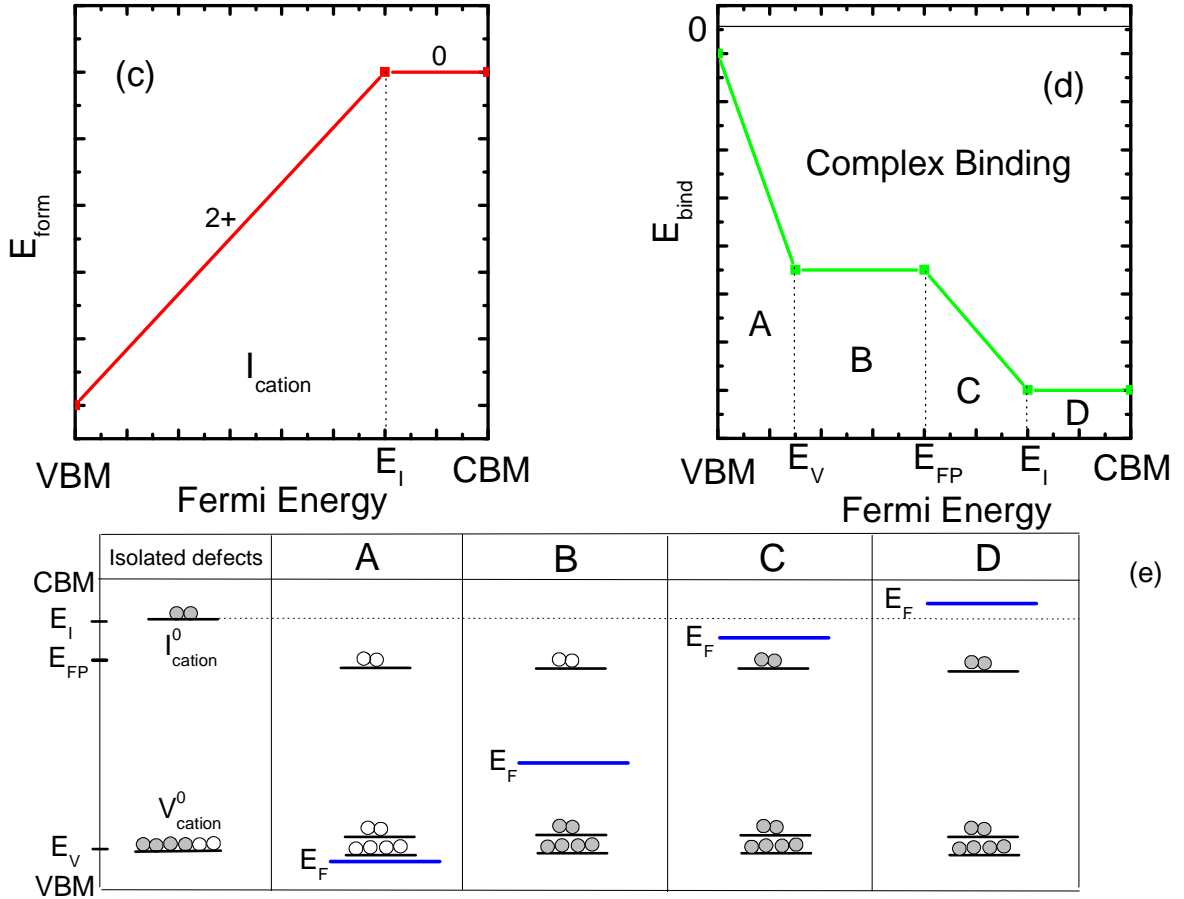


FIG. 3.6. Schematics of defect formation energies E_{form} of (a) a Frenkel pair, (b) an isolated cation vacancy V_{cation} , and (c) an isolated cation interstitial I_{cation} as a function of the Fermi level. The circles mark transition energies. (d) Binding energy E_{bind} of the FP obtained as the difference between E_{form} of the FP with respect to those of the isolated I_{cation} and V_{cation} . E_{bind} can be divided into 4 characteristic regions of E_F are denoted by A, B, C, and D, in which the charge states of the defects differ, as shown in (e).

The non-vanishing binding energies together with the mobility of Zn_i and Cd_i imply a tendency to form V - I pairs. Moreover, the formation barriers are comparable to the values of elementary excitations allowed in these materials, which are comparable with band gaps. In n-type samples, cation vacancies are the dominant compensating acceptors, and their concentration exceeds that of interstitials. Thus, most interstitials should form V - I pairs, but a finite concentration of isolated and non-paired vacancies is expected. The situation is reversed in p-type samples, where the interstitials are the dominant compensating donors, their concentration is higher than that of vacancies, and thus a finite concentration of isolated interstitials is expected.

Now we turn to research the stability of a FP with respect to the dissociation into its constituents. The diffusion of both an isolated cation vacancy and cation interstitial in CdTe

and ZnTe were investigated in Chapter 2. All mechanisms analyzed for isolated constituents were employed to examine the dissociation of a FP they constitute. The results for CdTe and ZnTe are in Tables XVII and XVIII, respectively.

TABLE XVII. Calculated dissociation barriers (in eV) for different diffusion mechanisms and charged states of c-FP ($V_{\text{Cd}} + \text{Cd}_i$) in CdTe. The values in parentheses represent barriers for the return to the initial c-FP.

		$V_{\text{Cd}} + \text{Cd}_i$ in CdTe						
		FP ⁰	FP ¹⁺	FP ²⁺	FP ³⁺	FP ⁴⁺	FP ¹⁻	FP ²⁻
Diffusion of V_{Cd}	First neighbor	-	-	-	-	-	-	-
	Plane passing	1.20 (1.20)	1.10 (1.05)	1.10 (1.05)	1.05 (1.00)	1.00 (0.95)	1.25 (1.15)	1.05 (1.00)
	Cluster assisted	2.00 (1.85)	1.90 (1.80)	1.85 (1.80)	1.80 (1.70)	1.70 (1.65)	2.15 (2.00)	2.05 (1.95)
	Fourth neighbor	2.95 (2.90)	2.90 (2.85)	2.90 (2.75)	2.80 (2.70)	2.75 (2.70)	3.20 (3.05)	3.00 (2.95)
Diffusion of Cd_i		-	-	-	-	-	0.50 (0.05)	0.65 (0.00)

TABLE XVIII. Calculated dissociation barriers (in eV) for different diffusion mechanisms and charged states of c-FP ($V_{\text{Zn}} + \text{Zn}_i$) in ZnTe. The values in parentheses represent barriers for the return to the initial c-FP.

		$V_{\text{Zn}} + \text{Zn}_i$ in ZnTe						
		FP ⁰	FP ¹⁺	FP ²⁺	FP ³⁺	FP ⁴⁺	FP ¹⁻	FP ²⁻
Diffusion of V_{Zn}	First neighbor	-	-	-	-	-	-	-
	Plane passing	1.40 (1.40)	1.30 (1.30)	1.30 (1.30)	1.30 (1.25)	1.25 (1.20)	1.40 (1.40)	1.30 (1.30)
	Cluster assisted	2.50 (2.45)	2.45 (2.40)	2.40 (2.40)	2.40 (2.30)	2.35 (2.30)	2.55 (2.55)	2.60 (2.55)
	Fourth neighbor	3.65 (3.60)	3.60 (3.50)	3.55 (3.45)	3.50 (3.45)	3.40 (3.40)	3.80 (3.75)	3.80 (3.80)
Diffusion of Zn_i		0.55 (0.25)	0.55 (0.20)	0.55 (0.15)	0.50 (0.10)	0.50 (0.10)	0.60 (0.20)	0.80 (0.30)

I begin with dissociation caused by out-diffusion of vacancy. As it follows from the comparison of Tables XVII and XVIII with Table III (sec. 2.1.1) barrier heights for vacancy diffusion to the second neighbor by plane passing mechanism in both compounds are

enhanced by at least 0.2 eV when vacancy constitutes a FP. It can be mainly attributed to electrostatic attraction between constituents of a FP, which firstly has to be compensated in order to trigger off the out-diffusion. The atomic rearrangements due to the formation of a FP can also influence the efficiency of diffusions (this aspect is of huge significance for a-FPs – Sec. 3.2). The barrier for dissociation (i.e., to form a distant V and I pair) is slightly higher than that corresponding one to the return to the initial FP configuration (presented in Fig. 3.1). It reflects a small, nevertheless, clearly evident propensity to stabilize the initial FP. The material trends operative in a description of isolated cation vacancies (Sec. 2.1.1) are also valid here. Other diffusion mechanisms than plane passing are more energetically demanding, and the diffusion to the first neighbor is not active ($\text{Te}_{\text{Cd}+} + \text{V}_{\text{Te}}^{1st}$ and $\text{Te}_{\text{Zn}+} + \text{V}_{\text{Te}}^{1st}$ defect pairs are not even metastable with respect to the vacancy of a FP, and the Te_{Cd} and Te_{Zn} antisite atoms spontaneously relax into the substitutional position, Te^{1st} , like it is in the isolated cation vacancy case).

The dissociation of a FP by out-diffusion of the interstitial can occur by the jump along (2) line in Fig. 3.1. There are three equivalent sites due to the C_{3v} symmetry of a FP, and the T:Cd site presented in (110) plane is one of them.

(i) In CdTe, such a jump is not possible, since Cd_i relaxes back to initial configuration of c-FP with no barrier to within my accuracy. This is due to the relatively strong value of intrapair electrostatic attraction in FP when compared with diffusion barriers for isolated cation interstitials – see Table VIII (Sec. 2.2.3). To a good approximation the cation interstitial location in the c-FP is the only one metastable position in CdTe. It means that out-diffusion of cation vacancy induces spontaneous relaxation of its interstitial partner in a FP, i.e., a FP does not dissociate as interstitial is following the jumps of diffusing vacancy. As a consequence, the stability of a FP in CdTe is limited solely to the effects of recombination.

(ii) Generally, the situation in the case of ZnTe is similar. The jump along (2) line is possible, but the barrier for the return is very small, 0.1-0.2 eV. In contrast to CdTe, the metastability of out-diffused positions is clearly evident for all charge states (Table XVIII). Due to electrostatic effects this metastability is diminished as a FP becomes positively charged. The diffusion barriers for out-diffusion are enhanced by about 0.1 eV juxtaposing with barriers valid for isolated cation interstitials if a FP is positively charged (it corresponds to cation interstitial in 2+ charge state) - compare Tables XVIII and VIII (Sec. 2.2.3). In negative charge states, when cation interstitial level is occupied, electrostatic repulsion of constituents facilitates out-diffusion in a FP compared with an isolated cation interstitial. Because of small,

but pronounced metastability of out-diffusion positions, FPs in ZnTe are expected to be less stable than in CdTe. Both recombination and out-diffusion of constituents can destabilize a FP in ZnTe.

3.2 Anion sublattice

I now turn to formation of a $V_{\text{Te}} - \text{Te}_i$ pair, i.e., an anion FP (a-FP). Properties of isolated V_{Te} and Te_i were discussed earlier in Secs. 2.3 and 2.4. The C_{3v} symmetry configuration, similar to that for c-FPs, is the metastable configuration with the lowest energy (see Fig. 3.1, with Cd and Te atoms interchanged, to visualize the a-FP). In the case of c-FPs it is a natural configuration, as their isolated constituents maintain approximately the T_d symmetry, and the final C_{3v} symmetry of a FP is a result of the superposition of the configuration of the vacancy and the interstitial. The perturbation stems more from the close vicinity of defects (i.e., correlated relaxation) than electrostatic interaction (see below for explanation). In the case of the a-FP the situation is different. An isolated anion vacancy can assume cation dimer and T_d configuration depending on a charge state (Sec. 2.3). An isolated anion interstitial occupies an ‘elemental Te’ like site that exhibits huge atomic rearrangements for almost all charge states except in $Q=-2$ charge state, for which the T_d symmetry is conserved (Sec. 2.4). Formation of an a-FP inhibits most for these configurations. The a-FP manifests the C_{3v} symmetry like a c-FP, but with a much smaller perturbation from the T_d symmetry.

The electronic structure of a-FP is presented schematically in Fig. 3.7. The large reconfigurations of isolated constituent defects cause the large lowering of energy levels with respect to the C_{3v} configuration. It is especially evident in the case of vacancy, for which ground state the C_{2v} configuration has doubly occupied singlet below the VBM, whereas the anion vacancy in metastable C_{3v} configuration introduces singlet close to the CBM. The singlet level of anion vacancy in a FP is above CBM (see Fig. 3.7), and give its two electrons to CBM, which with near zero energy barrier land into lower energetic levels originating from Te_i . The resultant a-FP has fully occupied singlet and doublet, which originate from Te_i in the C_{3v} configuration.

The close proximity of defects in the complex and the smaller electrostatic coupling between them increases the distance between V and I by 0.2 \AA in CdTe and 0.05 \AA in ZnTe relative to the ideal configuration. This is in contrast to a c-FP, where the distance is

diminished and the corresponding values are bigger (see Sec. 3.1). The main reason for this peculiarity can be attributed to the equilibrium configurations and properties of the constituents of a FP and will be elucidated below.

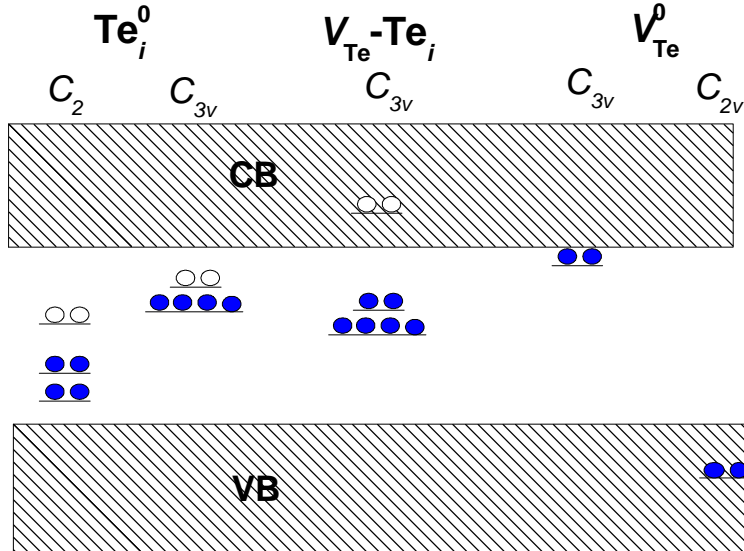


FIG. 3.7. Electron levels of a-FP, and its constituents in the lowest energy configurations and those characteristic of a-FP, i.e., in the C_{3v} symmetry. The triplet level of vacancy is in CB. The singlet level of interstitial is deep in VB.

First, the relaxation which lowers greatly the level position of V_{Te} is inhibited by the proximity of the interstitial. Thus, the orthorhombic (C_{2v}) relaxation mode, operative in an isolated anion vacancy, leading to the formation of Cd-Cd dimer bonds (Sec. 2.3) is not working here. When V_{Te} forms a a-FP, the relaxation does not take place and subsequently a singlet position lowering is not realized. This restriction of atomic relaxation around V_{Te} causes that the singlet level of V_{Te} is above the CBM for all possible charge states of a FP. This is why the singlet of V_{Te} in CdTe does not play crucial role during changes of charge state of the FP. The energetics and charging depends solely on anion interstitial. In the case of ZnTe the fully occupied singlet of V_{Te} is below the CBM (Sec. 2.3). The singlet is positioned to within 0.05 eV like in an isolated case. Here, those two electrons are transferred from V to I . The singlet level of V_{Te} in ZnTe is important in n-type regime, because it can accommodate up to 2 electrons even before the Fermi energy reaches CBM. That is why FP in ZnTe can assume 2- charge state (Fig.3.9b) in contrast to CdTe (Fig.3.9a).

Second, the splitting of triplet level of Te_i stemming from symmetry breaking from T_d to C_{3v} is weak and does not exceed 0.02 eV for all cases under study. The positions of split

triplet levels are to within 0.05 eV with those for isolated anion interstitials in the T_d configuration (the values for 1- and 2- charge states are presented in Tables XII and XIII for CdTe and ZnTe, respectively).

Third, it is important to emphasize that alterations in occupation of the singlet level of anion vacancy, although accompanied by 2e change in charge on the singlet, are not influencing overall net charge of this defect center. The similar behavior is common for transition metals (TM) in insulators [60] which exhibit peculiar tendency to maintain a constant local charge under external perturbations in terms of an inherent, homeostasis-like negative feedback. It is realized when the energetic relations between the anion dangling bond levels and those coming from TM orbitals are interchanged. The same symmetry representation and spin levels interact to result in bonding and antibonding levels. When the energy of TM level is lower than that of the anion dangling bond then the crystal field resonance which has pronounced TM character is bonding like. The antibonding dangling bond hybrid originates from the anion dangling levels. When the energetic relation between TM level and anion dangling bond is reversed (it can be realized, when additional electron is accommodated in TM orbitals, which is equivalent to charging of the defect), the bonding and antibonding origin is also switched. In this case the relative weight of the bonding levels shifts towards the ligands, and the negative feedback gives rise to a depopulation of TM charge in the bonding states. This outflow of charge counterbalances the increase in the antibonding gap-level charge. As a consequence of the self-regulated response, the net local charge at the TM site stays constant. The same charge self-regulation upon charging is observed for anion vacancy. Here, the a_1 orbital pertaining to the V_{Te}^0 is constructed from bondinglike combination of two Cd dangling bond orbitals, and is deep in the valence band. This is in contrast to V_{Te}^{++} state which is formed by combination of four nearest neighbor orbitals, has antibonding character, and is resonant with CBM (see Sec. 2.3 for details).

The changes of total energy are shown in Fig. 3.8. Several features can be distinguished.

1. The generation barrier exceeds 6 and 8 eV for any charge state, for CdTe and ZnTe, respectively. The generation of a FP in ZnTe costs more energy due to the higher stiffness of this compound in comparison with CdTe as it was discussed in detail in Chapter 2. The high energy to generate a $V_{\text{Te}} - \text{Te}_i$ pair is consistent with the calculated high formation energies of its constituent defects. One should remember that C_{3v} symmetry configuration is not the ground state of neither anion vacancy nor anion interstitial. Because the higher energetic

configurations have to be realized in a FP for its ingredients, the resultant formation energy is higher.

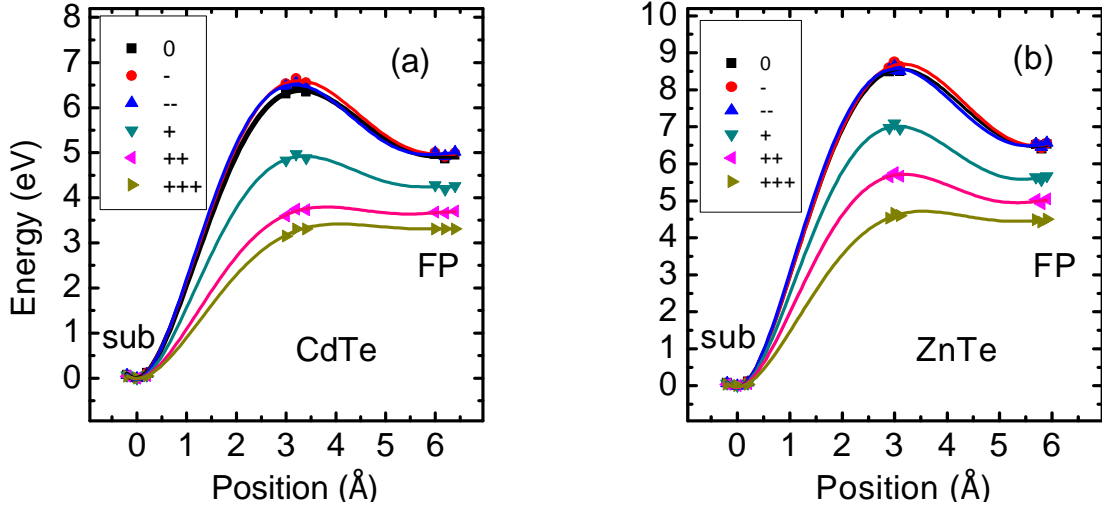


FIG. 3.8. Total energy change corresponding to a creation of $V_{Te} - Te_i$ Frenkel pair (FP) in (a) CdTe and (b) ZnTe as a function of the distance from the substitutional site (sub) for three charge states.

2. Formation energies of a-FP have strong dependence on the charge state. The formation barrier decreases to 3.3 and 4.7 eV for the 3+ charge state, for CdTe and ZnTe, respectively. The values of formation barriers are prohibitively large even in highly p-type material (barriers are at least 1.5 eV higher in energy than the band gaps of a given material), and the generation of FPs on the anion sublattice may be neglected until high temperature regime is considered. Moreover, the stability of the a-FPs is diminished with the barrier for recombination of a a-FP decreasing from 1.5 to 0.2 eV with the charge state changing from 0 to 3+ (see Table XIX). Thus, a-FP, in both CdTe and ZnTe, are practically unstable with respect to recombination. The discrepancies between formation energies for $E_F = \text{VBM}$ in Fig. 3.9 and those in 3+ charge state in Fig. 3.8 are due to the effect explained in Sec. 3.1 (namely, differences between Figs. 3.5 and 3.2). Because of acceptor-like character a FP can lower formation energy when an electron reservoir becomes lower in energy than the split triplet level and approaches VBM. The further lowering of formation energy in ZnTe, compared to CdTe, when E_F approaches CBM is due to the same reasons like for c-FPs. In opposition to c-FPs the formation of a-FPs is easier if additional holes are present. This is due to the fact that the energetics of FPs is ruled by C_{3v} symmetry configured anion interstitial, which acts like a deep donor. In effect, any lowering of the E_F is expected to lower formation energy. This is in contrast to c-FP, where energetics is governed by cation vacancy with two

additional states of cation interstitial acting like 2 additional deep acceptor levels. Naturally, cation vacancy is an acceptor, also as a FP's constituent, but because of pronounced interaction with cation interstitial it becomes much more deep (Fig. 3.5). In the case of a-FP, the interaction with its partner in a FP is weaker, mainly because of negative feedback effect that causes anion vacancy charge to be constant and overall neutral upon charging. Thus an a-FP has formation energy behavior facets very similar to those characteristic of formation energy of an isolated anion interstitial (cp. Fig. 3.9 and Figs. 2.23 and 2.24). a-FPs, both in CdTe and ZnTe, have transition energies within 0.25 eV to isolated anion interstitials in corresponding compounds. Finally, one can interpret the dependence of barrier heights on the charge state of the FP using the scheme adopted in the case of c-FP. Generation barriers are determined by the interaction between the interstitial of a-FP and the three anion atoms. In covalent-ionic CdTe and ZnTe, three anion atoms that form a plane, which is to be passed by the interstitial just in order to generate a-FP, are negatively charged. Thus, additional holes on the interstitial facilitate generation of a-FP. On the other hand, the a-FP is stabilized by four cation atoms, which are positively charged, and electrostatic interplay between surrounding cation atoms and the interstitial determine recombination barriers. In this case, negatively charged a-FP enhances recombination barriers, and thus also stability of a-FP.

3. Positive binding energies for both CdTe (Fig. 3.9c) and ZnTe (Fig. 3.9d) reflect the fact that low-energy, highly reconstructed configurations cannot be realized in the case of a-FP. If the C_2 symmetry a-FP was created, it would be less demanding energetically to generate and the binding energy could be negative. Moreover, the energy transfer from the singlet of V_{Te} to the split triplet of Te_i is not large and accompanied by electrostatic interaction which if was operative would decrease formation energy and move binding energy negative. Negative binding energy denotes a situation where total energy of a FP is lower than the sum of isolated constituents of the FP. It can be realized by charge transfers, surplus relaxation or interaction. In an a-FP the first contribution is small, the second nonexistent (actually, the stifled relaxation acts oppositely and enlarge the formation energy), and the last negligible due to charge self-regulation of anion vacancy. As a result, mainly due to strongly restricted relaxation and destitution of the other contributions, the binding energy is positive. In the case of a c-FP, relaxation is also weakened with respect to the isolated cases, but this inhibition is small and compensated by pronounced interaction and a charge transfer which together turn complex binding energy negative. An a-FP in CdTe has binding energy positive irrespective

of E_F . The a-FP in ZnTe is expected to be weakly stable against its constituents disproportionation in n-type regime and close to the intrinsic region.

TABLE XIX. Calculated diffusion barriers (in eV) for different configurations and charge states of a-FP in CdTe and ZnTe.

Path	Charge state	Barriers	
		CdTe	ZnTe
sub-FP	2-	6.6	8.6
FP-sub	2-	1.6	2.2
sub-FP	-	6.6	8.8
FP-sub	-	1.7	2.3
sub-FP	0	6.4	8.6
FP-sub	0	1.6	2.2
sub-FP	+	5.0	7.1
FP-sub	+	0.8	1.5
sub-FP	2+	3.8	5.8
FP-sub	2+	0.1	0.8
sub-FP	3+	3.3	4.7
FP-sub	3+	0.0	0.2

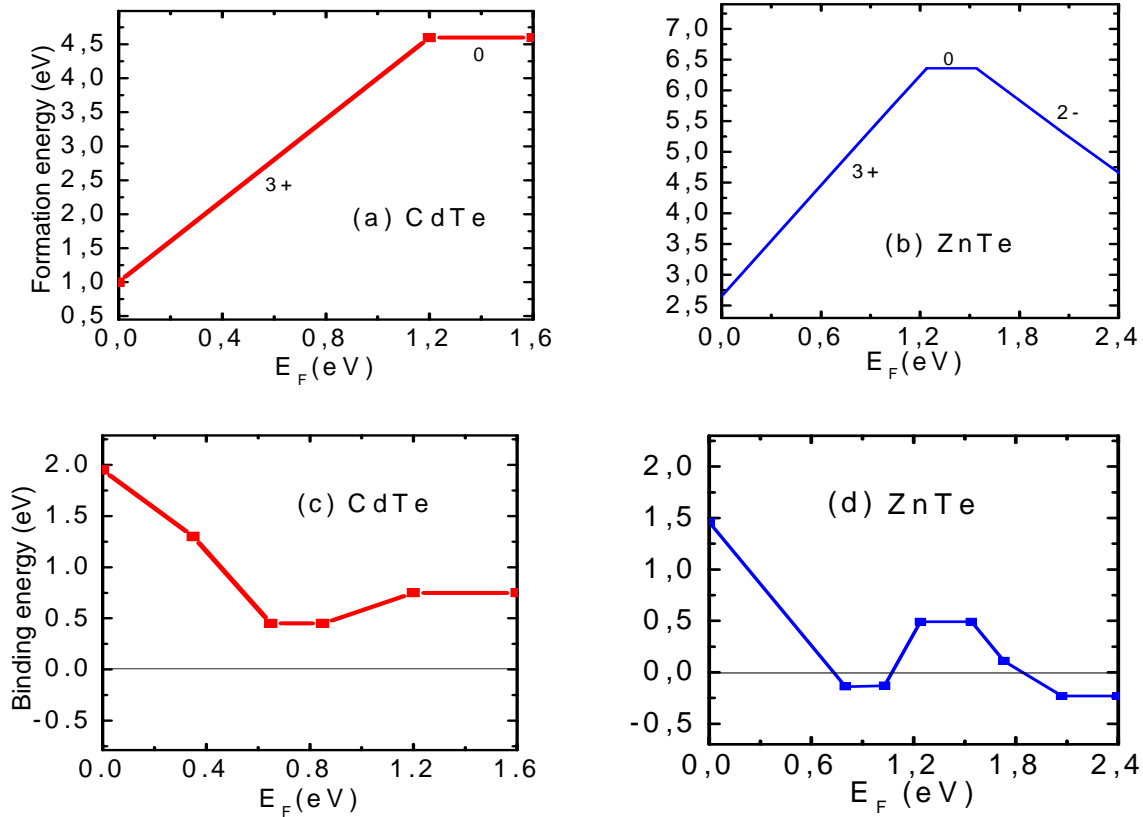


FIG. 3.9. Calculated dependencies on the Fermi energy of (a) formation energies $V_{Te} + Te_i$ in (a) CdTe and (b) ZnTe, and of the binding energies of FPs in (c) CdTe and (d) ZnTe.

TABLE XX. Calculated dissociation barriers (in eV) for different diffusion mechanisms and charged states of a-FP ($V_{\text{Te}} + \text{Te}_i$) in CdTe. The values in parentheses represent diffusion barriers for the return to the initial a-FP configuration.

		$V_{\text{Cd}} + \text{Cd}_i$ in CdTe						
		FP ⁰	FP ¹⁺	FP ²⁺	FP ³⁺	FP ⁴⁺	FP ¹⁻	FP ²⁻
Diffusion of V_{Te}	First neighbor	0.85 (1.85)	0.40 (1.55)	0.20 (1.45)	0.10 (1.10)	0.05 (0.95)	0.35 (0.65)	0.00 (0.25)
	Plane Passing	1.25 (1.10)	1.35 (1.40)	0.35 (1.80)	0.40 (1.55)	0.35 (1.30)	1.65 (1.40)	1.10 (0.85)
	Cluster Assisted	2.20 (1.95)	2.45 (2.20)	1.65 (2.40)	1.70 (2.60)	1.45 (2.50)	2.20 (2.00)	1.75 (1.85)
	Fourth neighbor	3.65 (3.90)	3.75 (3.65)	1.40 (3.40)	1.30 (3.15)	1.30 (3.45)	3.75 (3.40)	3.35 (3.15)
Diffusion of Te_i		0.05 (0.00)	0.00 (1.50)	0.00 (1.50)	0.00 (1.20)	0.00 (1.05)	0.05 (0.00)	0.15 (0.00)

TABLE XXI. Calculated dissociation barriers (in eV) for different diffusion mechanisms and charged states of a-FP ($V_{\text{Te}} + \text{Te}_i$) in ZnTe. The values in parentheses represent diffusion barriers for the return to the initial a-FP configuration.

		$V_{\text{Zn}} + \text{Zn}_i$ in CdTe						
		FP ⁰	FP ¹⁺	FP ²⁺	FP ³⁺	FP ⁴⁺	FP ¹⁻	FP ²⁻
Diffusion of V_{Te}	First neighbor	0.25 (2.00)	0.05 (2.00)	0.00 (2.10)	0.15 (1.90)	0.20 (1.60)	0.40 (2.25)	0.00 (2.30)
	Plane passing	0.90 (2.10)	0.85 (2.00)	0.50 (1.95)	0.40 (1.80)	0.35 (2.00)	0.90 (2.40)	0.60 (2.45)
	Cluster assisted	1.40 (2.75)	1.75 (2.55)	1.25 (2.70)	1.00 (2.35)	1.05 (2.05)	1.40 (2.60)	1.15 (2.70)
	Fourth neighbor	2.15 (4.85)	2.05 (4.10)	1.40 (4.20)	3.50 (3.45)	1.10 (4.15)	2.00 (4.95)	1.55 (5.00)
Diffusion of Te_i		0.05 (0.15)	0.00 (1.60)	0.00 (1.90)	0.00 (1.55)	0.00 (1.20)	0.00 (0.25)	0.00 (0.25)

The analysis of dissociation of a-FPs corroborates earlier considerations and results. The positive binding energy in both CdTe and ZnTe suggested that these FP can be unstable against dissociation. Due to unrealized, pent-up relaxation there is a tendency for the complex to dissociate. The results in Tables XX and XXI prove this assumption. From the point of view of anion interstitial in both CdTe and ZnTe, there is a propensity to disproportionate a FP. The barriers to accomplish this dissociation are zero or negligible. The easiness of out-diffusion of anion vacancy also encourage the dissociation. Even diffusion to the first

neighbor, not active in c-FPs, is acting in favor of tearing the FP apart. The diffusion of anion vacancy to both the second and the fourth neighbor also favors the dissociation, although not in all cases in CdTe. The barrier height relations between different mechanisms and different compounds are similar like in the previous investigations of diffusion.

To conclude, a a-FP is expected to be difficult to form and unstable against a disproportion of its constituents.

3.3 Conductivity switching and electric polarization effects – a microscopic model

Experimental results on conductivity switching and polarization effects can be summarized as follows:

(1) Schottky diodes based on CdZnTe [61, 62], CdZnS [63], CdZnSe [64], and CdMnTe [65] exhibit resistive bistability, i.e., reversible changes of resistivity between low and high resistance states induced by sufficiently high external voltages. Depending on the system, conductivities in these states differ from 2 to 6 orders of magnitude. They are due to the changes in carrier concentration and not because of changes in the mobility.

(2) II-VI alloys in high resistive state reveal ferroelectric-like behavior, i.e., the presence of electric polarization with a hysteresis loop [61, 62, 66-68]. Electric polarization can be altered by free carriers generated by illumination of the samples [61].

(3) Conductivity switching and ferroelectric-like behavior are observed only in alloys, and are absent in the end binary compounds [62, 68]. For example, the effect is observed in CdZnTe with the Zn content ranging from 4 to about 30%, but in neither pristine CdTe nor pristine ZnTe [62, 67].

(4) CdZnTe alloys have an undistorted zinc-blende structure, as shown recently by synchrotron radiation diffraction [69] and X-ray diffraction [62].

(5) Polarization effects in CdZnTe are observed in both bulk samples and epitaxial layers, and in both intrinsic and p-type samples, which indicates that the effects have an intrinsically bulk character [62, 70].

(6) Current-voltage characteristics and ferroelectric hysteresis is asymmetric in crystalline samples, and symmetric in polycrystalline samples [70].

(7) Optical spectra of CdZnTe are different in the two resistivity states [71].

Bistabilities of conductivity and electric polarization were previously observed in Schottky diodes based on the ferroelectric semiconductor PbTiO_3 [72]. In this system, the intrinsic electric field of PbTiO_3 contributes to the total field in the diode. Interpretation of the experiment is based on the fact that a reversal of ferroelectric polarization induces changes in the width of the depletion zone, and thus switches the diode between the high- and the low-conductivity states. The observed electrical characteristics of diodes based on II-VI alloys strongly resemble those of ferroelectric diodes. However, the zinc-blende structure of II-VI alloys prohibits ferroelectricity, and thus a different explanation is expected to be found. Clearly, it is not possible to provide a detailed interpretation of all experimental results at this stage, since this would require both a more complete experimental understanding of physical processes, and a simulation of conductivity of diodes at the mesoscopic scale, which is outside the scope of this thesis. However, the results obtained were allow to tentatively propose that the experimental data listed above stem from the generation-recombination of $V-I$ pairs.

In particular, generation of c-FPs may explain conductivity switching in CdZnTe diodes. The scenario is schematically shown in Fig. 3.10. Initially, the junction is in the low-resistivity state, since free carriers are present and concentrations of possible compensating defects are negligible. When the applied voltage is high, the induced electric field causes bending of bands and accumulation of electrons at the appropriate interface. The presence of excess electrons induces in turn generation of FPs, as it is discussed in Sec. 3.1 and shown in Fig. 3.10b. The process of c-FPs' generation is expected to be operative in CdZnTe as the elementary excitations are comparable in energy to the formation barriers, especially in the presence of additional electrons when the formation energy of the FP is lowered considerably. In the situation of FP's formation, partially occupied states exist in the band gap, and electrons from the defect states may compensate free holes and switch the system to the high-resistivity state. This process is shown for a p-type layer, but the possibility of compensation of n-type layers is also evident. As it was shown during discussion of c-FPs, after compensation, i.e., after losing electrons from the fully occupied state, the cation vacancy is not expected to behave as dominating acceptor, which is the case for an isolated cation vacancy. The formation of a FP induces the increase of the single electron levels of a cation vacancy by about 0.2 eV, and the ionization is considerably less efficient in the room temperature regime. FPs may recombine, which brings the system back to the low-resistivity state (a). The recombination can be caused by oppositely biased voltage or injection of holes as it was shown in Sec. 3.1. Thus, cation interstitial in a FP, which is electrically active, can

return to the substitutional position as high voltage is applied (temperature stimulus can accomplish this too). Although the levels are also optically active the switching between resistivity states is expected to be limited as a change in charge state of a FP does not destabilize profoundly the defect. This is in contrast to DX-like effects which are metastable only in one charge state, and optical manipulation actively influences the formation and the recombination of those defects provided they are optically active. Nevertheless, both barriers, i.e., the formation and for the return to the substitutional position (it was shown in Sec. 3.1 that dissociation for $V_{\text{cation}} - \text{Zn}_i$ entails higher energies, thus can be omitted in this discussion), can be altered by illumination and can influence greatly the efficiency of electric and temperature stimuli when applied simultaneously with optical one. Despite this limitation the optical experiments can probe two resistivity states and this model also explains why the observed optical spectra in the low- and the high-resistance states are different, ascribing the effect to the presence of defects in the latter case.

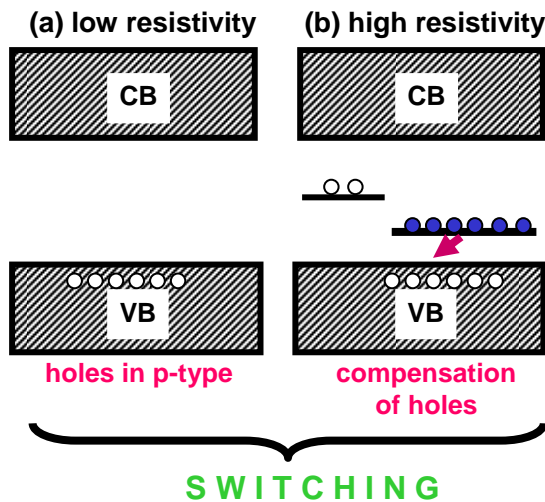


FIG. 3.10. Scheme of the electronic structure of CdZnTe. (a) Low resistivity situation: p-type CdZnTe with holes in the valence band. No defects are present. (b) High resistivity situation: after the generation of $V_{\text{cation}} - \text{Zn}_i$ pairs the holes are compensated by electrons from the defect states.

The presence of FPs is also a possible source of electric polarization and its changes. In fact, electric polarization and its hysteresis are observed in the samples in the high-resistivity state in which, according to the proposed model, there is a finite concentration of FPs. Since V_{cation} is a double shallow acceptor and Zn_i is a double deep donor, after formation of the complex two electrons are transferred from the interstitial to the vacancy, which corresponds to the formation of an electric dipole shown in Fig. 3.11. According to the

results of Chapter 1, diffusion of a positively charged Zn_i^{2+} occurs by long jumps between two adjacent T:Te sites with a barrier of about 0.85 eV. The calculation of diffusion between configurations (each time the interstitial is located approximately at T:Te) presented in Fig. 3.11 of a positively charged Zn_i^{2+} being in $V_{\text{cation}} - Zn_i$ complex gives value of 0.90 eV. Moreover, an investigation of diffusion in Sec. 3.1. implies that the out-diffusion of cation interstitial in such a complex in CdTe is expected to be highly improbable (see Table XVII). In the presence of external electric field, dipoles align along the field direction, and a change of the direction of the field induces a reconfiguration of the dipoles. However, since there are energy barriers between different configurations, a hysteresis of polarization is expected, in agreement with observations. Moreover, as the external electric field is approximately homogenous in the sample, the formation of dipoles in a direction indicated by the direction of applied electric field is energetically privileged. Finally, it was shown in Sec. 3.1 the electric dipoles lower their formation energy when they align in parallel with each other which suggests macroscopic orientation of dipoles.

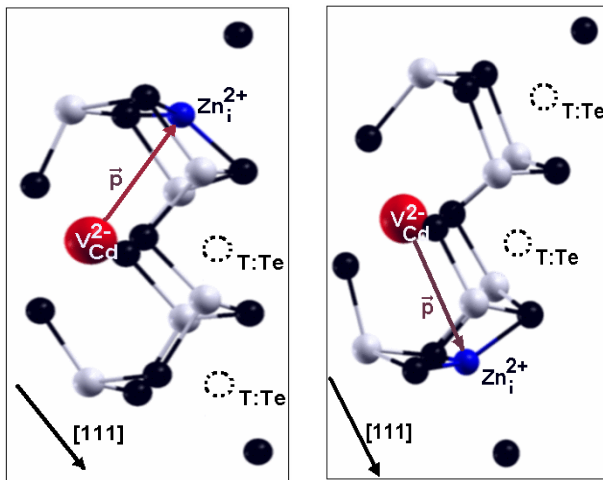


FIG 3.11. Two configurations of a $V_{\text{cation}} - Zn_i$ pair in CdZnTe. Cd and Te atoms are represented by white and black spheres, respectively. Dotted circles indicate possible interstitial T:Te sites. Left and right figures correspond to two different orientation of the electric dipole of the FP.

The proposed model requires a relative stability of FPs, which otherwise would recombine or dissociate. Stability of FPs from the point of view of the former aspect is discussed in Sec. 1.1, where I point out that in general there are finite barriers for recombination of 0.45-0.60 eV (for CdTe:Zn in different charge states). These values are at least twice higher than the barriers of 0.2 eV calculated for metastable DX -like configurations

of anion vacancies in ZnO and CdTe, which were proposed to cause PPC effects at room temperature [51]. Similarly, it was proposed that the barrier of 0.32 eV stabilizes metastable *DX* centers in Cu(In,Ga)Se₂ up to 300 K [5]. Finally, since the diffusion barrier of 0.2 eV is sufficient to prevent annealing of FPs in Si up to 150 K [4], one may expect that the barriers of about 0.5 eV should stabilize FPs in CdZnTe at room temperature. The calculated barriers for return also explain why annealing at the temperatures of about 400 K causes that the samples return to low resistivity state. Furthermore, as it follows from Tables XVII and XVIII, the barriers for the jump to the tear the FP apart are more than 1.2 eV, which is relatively high and thus stabilizes the $V_{\text{cation}} - \text{Zn}_i$ pair with respect to dissociation.

As it was already mentioned, the switching effects are observed only in alloys. This fact was recently confirmed by a detailed experimental study of CdZnTe [62]. The results of Sec. 3.1 are in qualitative agreement with this observation. First, the barrier for generation of a $V_{\text{cation}} - \text{Zn}_i$ pair is the lowest, see Figs. 3.2 and 3.3 and Table XV. Second, this pair is the only one with pronounced stability in all accessible charge states. For the remaining FPs in the 1+ state assumed in p-type samples the barrier for recombination is lower than 0.1 eV, or vanishes, see Fig. 3.2 and Table XV. These two factors may explain why both the conductivity switching and the ferroelectric behavior are observed only in CdZnTe alloys, and are absent in pure ZnTe and CdTe.

Finally, the model implies that in monocrystals both the resistivity switching and the polarization effects are not symmetric when the sign of the applied voltage is reversed, because the formation of the *V-I* pairs occurs along the [111] direction that lacks the reflection plane. This feature agrees with experimental results, which are symmetric only in the case of polycrystalline samples.

Concluding, the proposed microscopic model provides a tentative and qualitative interpretation of the experimental observations (1)-(8) summarized at the beginning of this Section. However, there are other effects that may affect both the resistivity and the capacitance of diodes based on II-VI alloys, such as the field-driven in-diffusion, surface effects and electromigration of contaminations from contacts due to the lack of control of interfaces.

3.4 Influence of the electrical conductivity on magnetic properties of CdZnMnTe

It is interesting to investigate the possibility of expanding the functionality of CdZnTe alloys by adding magnetic Mn ions into the system. CdMnTe is well known and the most extensively studied compound in $A_{1-x}^{II}Mn_xB^{VI}$ group in which Mn ions are antiferromagnetically (AFM) coupled by superexchange type interaction mediated by Te atoms [73]. The coupling is short ranged, nonvanishing practically only in the first neighbor configuration. These well established findings, in line with the electronic structure peculiarities, were corroborated in my LSDA calculations in which substitutional, low resistivity state $Cd_{29}Zn_1Mn_2Te_{32}$ and $Cd_{61}Zn_1Mn_2Te_{64}$ in different configurations was considered. In this case, both the Zn and the Mn atoms occupy cation sites. The first neighbor configuration represents the situation when two Mn ions are spaced only by the Te atom, like presented in Fig. 3.12. The coupling constant J is defined as the computed total energy difference between ferromagnetic (FM) and AFM configuration. The interaction is definitely short-ranged as expected, see Fig. 3.13. Because of the short-range interaction of the Mn ions, even relatively small supercells can adequately describe the magnetic behavior. In consequence, enlarging the system does change J only slightly as witnessed in Fig. 3.13.

The situation changes dramatically when a FP already attributed high resistivity state (see Sec. 3.3) is generated in the system with the Mn ions. In this case, the Mn ions are coupled FM, and the interaction is not limited to first neighbor (Fig. 3.14). It is important to employ big supercells to obtain undistorted picture of the dependence of J on the distance between magnetic ions. The interaction is operative to the third nearest neighbor, which suggests that the concentration of the Mn ions exceeding 6.2 % should be enough to establish percolation in zinc-blende structure [74]. The long-range FM interaction of the Mn ions is mediated by one of the levels of the cation vacancy which is the building block of a FP that was generated in the system (Fig. 3.15). This statement is substantiated when comparing the spatial distribution of spin-down polarization with $|\psi|^2$ of the levels inherent to cation vacancy in a FP. As it was underlined in Sec. 3.1 the formation of a FP lowers of the local symmetry from T_d to C_{3v} which splits the triplet level of the cation vacancy into a doublet and a singlet. The $|\psi|^2$ of the triplet level (Fig. 2.2) decomposes into $|\psi|^2$ of the higher

energetic singlet, and the doublet level (Fig. 3.16a and 3.16b, respectively). $|\psi|^2$ of the singlet (Fig. 3.16a) matches the spatial distribution of spin-down polarization (Fig. 3.15b).

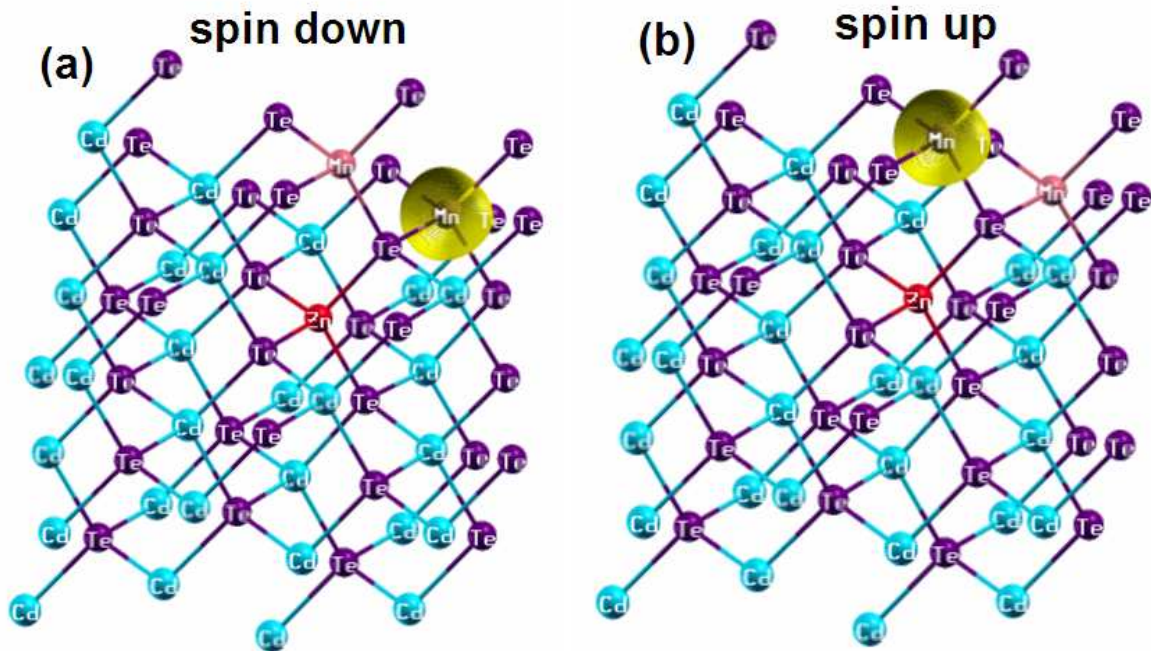


FIG. 3.12. Isosurfaces of (a) spin down, and (b) spin up polarization for substitutional, the Mn and the Zn ions on the cation-site, AFM coupled $\text{Cd}_{29}\text{Zn}_1\text{Mn}_2\text{Te}_{32}$. The Mn ions are in the first neighbor configuration.

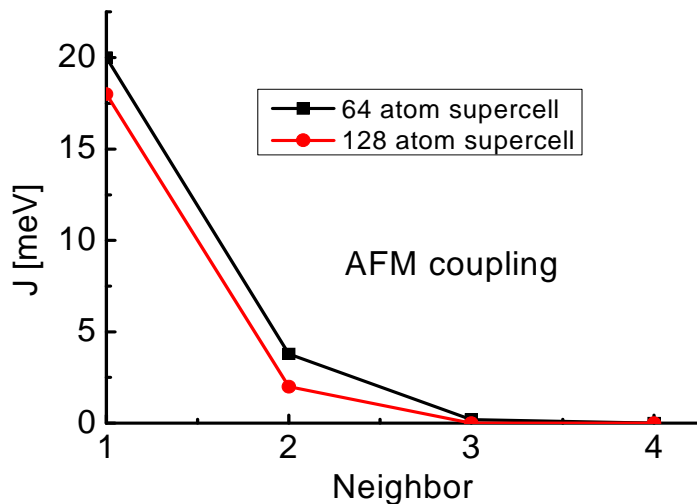


FIG. 3.13. Calculated dependence of the exchange parameter on the distance between the magnetic atoms in substitutional CdZnMnTe for various supercells. See text for the definition of J and the discussion. The lines are to guide eye only.

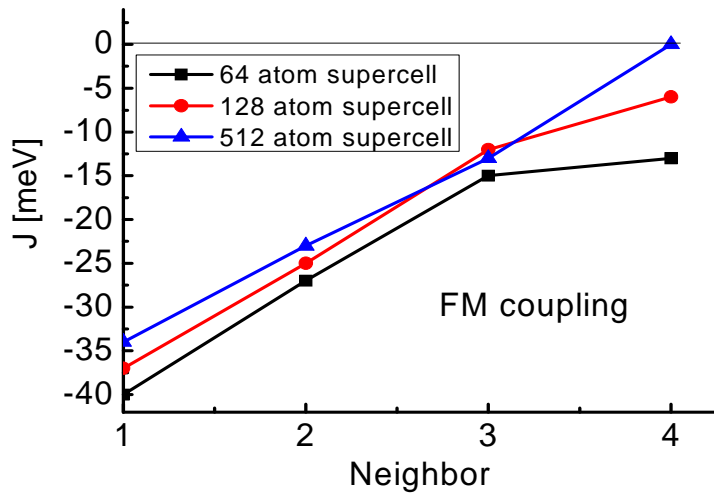


FIG. 3.14. Calculated dependence of the exchange parameter on the distance between the magnetic atoms in CdZnMnTe with c-FP for various supercells. See text for the definition of J and the discussion. The lines are to guide eye only.

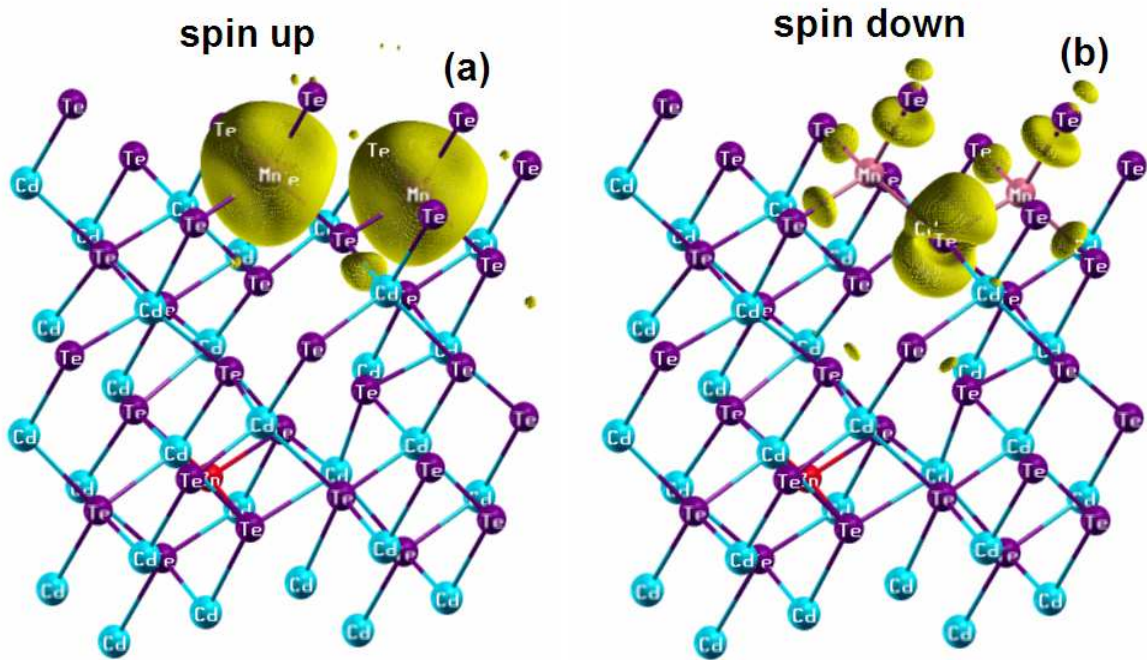


FIG. 3.15. Isosurfaces of (a) spin up, and (b) spin down polarization for the FM coupled Mn ions in the first neighbor configuration in $\text{Cd}_{29}\text{Zn}_1\text{Mn}_2\text{Te}_{32}$ with a c-FP.

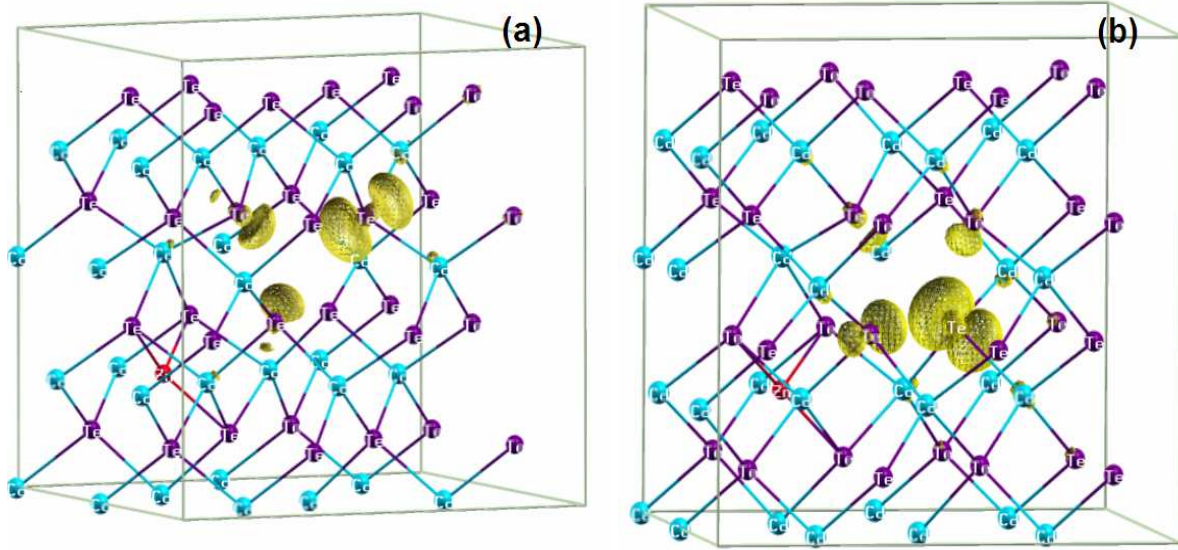


FIG. 3.16. Wave function square of (a) the singlet, and (b) the doublet levels pertinent to the cation vacancy in CdZnTe with c-FP.

Preliminary experimental results of CdZnMnTe samples exhibiting electric polarization bistability corroborate my theoretical inquiries [75]. EPR spectra experiments indicate that upon conductivity switching a quality change of magnetic behavior of the material takes place, and this change undergoes in a way I presented in this section.

Chapter 4

Frenkel pairs in other semiconductors

In this Chapter, the generation of FPs is investigated in the other important semiconductor systems. Both c-FPs and a-FPs are taken into consideration. In the beginning, I analyze these defects in two technologically important zinc blende systems, namely GaAs and 3C-SiC. Next, FPs are researched in wurtzite structure which although similar to the zinc blende structure can manifest different generation mechanism and exhibit diverse facets. Two emerging and intensively researched nowadays wurtzite compounds are addressed: GaN and ZnO.

4.1 GaAs

GaAs, similar to Si, was intensively investigated from the inception of ab-initio studies. In particular, the study of the defects received a decent attention [76-86]. In terms of relative concentrations of the native defects, the As antisite As_{Ga} is dominant in p-type regime, and the Ga vacancy V_{Ga} in n-type, both under the As-rich limit. For Ga-rich conditions and p-type, there are two defects: the As vacancy V_{As} and the Ga interstitial Ga_i with very similar E_{form} . In n-type material the Ga antisite Ga_{As} is a dominant native defect. It should be underlined that in any circumstances the anion interstitial As_i is energetically costly to produce. Because of this the defect pairs containing the above lowest-formation-energy constituents were envisioned to play an important role. Actually, the defect pairs, such as the DX centers [57], the EL2 [57], and the divacancies [79] were intensively investigated by both theoretical and experimental community. Due to the relatively high E_{form} of both a-

FPs and c-FPs they are expected to be energetically costly to generate. E_{form} of native defects differ from paper to paper, mainly because of different methodologies, supercell sizes, and methods implemented. Nevertheless, there is general agreement on the following properties of native defect (my results corroborate these finding):

(i) V_{Ga} acts like an acceptor with both transition energies $\epsilon_{V_{\text{Ga}}}(0/1-)$, $\epsilon_{V_{\text{Ga}}}(1-/2-)$, and $\epsilon_{V_{\text{Ga}}}(2-/3-)$ within 0.3 eV above the VBM [83]. E_{form} in As-rich regime is about 3 eV for E_{F} at the VBM and lowers below 1 eV at the CBM ($E_{\text{F}}=E_{\text{gap}}$). In Ga-rich regime E_{form} is respectively higher by the calculated ΔH in GaAs, ~ 1.0 eV [79, 80, 86], which is close to the experimental value, 0.736 eV [87]. In contrast to V_{cation} in II-VI compounds, V_{Ga} in the neutral charge state introduces the triplet level, which is occupied with three electrons.

(ii) Ga_i introduces a level in the band gap occupied with three electrons. The respective transition energies, $\epsilon_{\text{Ga}_i}(+/0)$ and $\epsilon_{\text{Ga}_i}(0/1-)$, are 1.0 and 1.2 eV above the VBM [86], which underline the amphoteric character of the Ga_i . E_{form} for $E_{\text{F}} = 0$ is below 1.5 eV at the Ga-rich limit. In n-type, under the Ga-rich conditions, E_{form} is about 2.0 eV. In all cases under study Ga_i prefers to occupy the T:Ga tetrahedral interstitial site [86].

(iii) V_{As} is a deep donor, which in the Ga-rich limit, and for $E_{\text{F}} = 0$, has relatively low E_{form} , 0.8 eV. In p-type it is in 3+ charge state in which the system undergoes substantial relaxation leading to the rehybridization of the four Ga atoms toward sp^2 bonding [81]. This lowers E_{form} by 1.5 eV making it a dominant defect in this regime and shifts upwards the a_1 level to about 1.1 eV above the VBM. The relaxation mode, similar to that observed in the V_{anion} in II-VI compounds (Sec. 2.3), results in nearly planar sp^2 bonding configuration. In n-type sample, the a_1 level captures two electrons, and V_{As} is in 1+ charge state with E_{form} of about 4 eV. The corresponding transition energy is expected to be in the mid band gap. E_{form} under the As-rich regime are higher than those at the Ga-rich regime by the ΔH .

(iv) As_i is an amphoteric native defect. It has a split interstitial ground state configuration in the neutral or -1 charge state, which entails two As atoms sharing an arsenic lattice site, displaced from this site in opposite directions along a [110] axis. The lowest energy configuration for positively charged As_i , namely the +1 charge state, is a split interstitial consisting of an As atom and a Ga atom sharing a gallium site, displaced from this site in opposite directions along a [100] axis [83-85]. The corresponding transition energies, $\epsilon_{\text{As}_i}(-1/0)$ and $\epsilon_{\text{As}_i}(0/1+)$, are within 0.2-0.6 eV above the VBM [83]. For all accessible E_{F} , E_{form} in the As-rich limit is not lower than 3.5 eV [83].

Despite the fact that V_{As} and As_i do not occupy sites with the T_d symmetry, both c-FPs and a-FPs have the C_{3v} symmetry in the ground state. Other configurations are much more energetically demanding with very small or zero barriers to relax into the ground state. The generation and recombination barriers (Table XXII) suggest that both types of FPs are possible, but energetically costly to generate. The material trends are similar to those characteristic of FPs in CdTe and ZnTe (Chapter 3):

- (i) The generation of c-FPs requires less energy than their anion counterparts for the same reasons like in CdTe and ZnTe.
- (ii) The generation barriers of c-FP can be further decreased in the presence of additional electrons, in opposition to a-FP which has comparable E_{form} in both intrinsic and n-type material.
- (iii) The injection of holes does not influence in a pronounced way the generation mechanism for c-FP. On the contrary, the generation barriers are considerably lower in p-type material for a-FP.

For short, even in n-type samples the generation of c-FP costs above 4 eV, which is prohibitively large in comparison with accessible energies and excitations ($\sim E_{gap} = 1.5$ eV). That is why generation of neither c-FPs nor a-FPs is expected to be efficient.

TABLE XXII. Calculated diffusion barriers (in eV) for different configurations and charge states of a-FP and c-FP in GaAs.

Path	Charge state	Barriers	
		Anion sublattice	Cation sublattice
sub-FP	2-	6.71	4.24
FP-sub	2-	0.97	1.28
sub-FP	-	7.38	4.89
FP-sub	-	0.98	1.09
sub-FP	0	7.57	5.34
FP-sub	0	0.97	1.03
sub-FP	+	7.08	5.25
FP-sub	+	1.01	1.02
sub-FP	2+	6.52	5.14
FP-sub	2+	1.13	1.04

FPs in GaAs were investigated in Ref. 76, and the calculated E_{form} agree to within 0.5 eV with my results. E_{form} was varied over E_F , and it was found that the c-FP is amphoteric in opposition to the a-FP which has a donor-like nature. The detailed comparison is not possible

due to the lack of barriers in Ref. 76, small supercells implemented, and failure to account for relaxation effects, which according to my calculations play an important role.

4.2. 3C-SiC

SiC is a very important emerging compound for high temperature, high frequency, and high voltage applications due to its high electron mobility, high thermal conductivity, high electron saturation velocity, and a wide bandgap. The comprehensive and unanimous investigation of native defects is complicated by the pronounced polytypism of the compound. More than 200 SiC polytypes have been determined, and two typical polytypes are zinc blende, 3C-SiC, with pure cubic stacking of the Si-C bilayers in the [111] direction and wurtzite, 2H-SiC, with pure hexagonal stacking in the [0001] direction. The other polytypes represent rhombohedral or hexagonal combinations of these stacking sequences with n Si-C bilayers in the primitive cell. When it comes to native defects, the differences between different polytypes are not very pronounced (see for example Ref. 88). I analyze only 3C-SiC here. There is a lot of publications concerning native defects in cubic SiC [88-94]. Generally, because of the strong chemical bonds done by C, the formation of native defects is very costly, and the mobility of such point defects is reduced. They are thermally stable at room temperature, and far above. Under C-rich regime the carbon vacancy V_C is the dominant native defect in p-type material, and when E_F approaches the CBM its equilibrium concentration is only than that of the carbon antisite C_{Si} . In the Si-rich limit, V_C is still the defect with the lowest E_{form} , which is 1 eV less than the silicon antisite, Si_C . In n-type sample, both V_C and Si_C dominate among all native defects. The properties of native defects acting as constituents of FPs that are the subject of my investigation (my results, in general, agree with those obtained in literature [88, 94]) are the following:

(i) The generation of V_C is generally accompanied by a remarkable Jahn-Teller distortion and as a consequence the low-spin states of V_C exhibit a negative- U behavior. The prototype behavior of this happens for V_C^0 . Here, the costs in energy to distort the crystal locally are overcome by an energy gain due to the overlap of dangling bonds and the formation of new dimerlike bonds, like it was in the case of V_{anion} in CdTe or GaAs. The effect is weakened for V_C^+ and vanishes for V_C^{++} . Under equilibrium conditions in the p -type limit, regardless of stoichiometry, V_C is a double donor with transition energy to neutral charge state of around

0.8 eV. In the Si-rich limit for $E_F = 0$, E_{form} of V_C^{++} is around 1eV, and for $E_F = \text{CBM}$, V_C is in neutral state with E_{form} of around 4 eV. In C-rich conditions E_{form} is increased by the calculated ΔH which is ~ 0.75 eV.

(ii) V_{Si} has E_{form} higher than 6 eV for all E_F . For all charge states only an outward breathing relaxation occurs due to the strong localization of the C dangling bonds at the neighboring C atoms. Consequently, high-spin configurations are predicted for V_{Si} with no Jahn-Teller distortion occurring independent of their charge state [88, 95]. The T_d symmetry is conserved and the basic mechanism is an outward breathing relaxation which increases with the decreasing number of electrons located at V_{Si} . The prohibitively large E_{form} clearly indicates that the concentration of V_C is higher than that of V_{Si} under equilibrium conditions. Only under extremely C-rich conditions and high n-doping levels E_{form} of V_{Si}^{--} approaches the values for V_C .

(iii) The neutral carbon interstitials C_i are found to have several nearly degenerate total-energy minima configurations in split-interstitial geometries (namely, the [100] split at carbon surrounded site, the [110] split at silicon surrounded site, and the geometry being the mixture of the two above see [94]), with E_{form} ranging—besides higher metastable ones—from 6.3 to 6.7 eV in stoichiometric SiC. C_i introduces deep levels in the band gap. The defect has amphoteric nature and E_{form} for any chemical potential, and for all E_F is not lower than 4 eV.

(iv) The neutral silicon interstitials Si_i have a clear ground state configuration at the tetrahedral site with the carbon nearest neighbors, with $E_{\text{form}} = 6.0$ eV. The split interstitial in the [110] direction at the silicon site and the tetrahedral configuration with the silicon nearest neighbors are metastable and have the significantly higher E_{form} . In contrast to C_i , Si_i at the tetrahedral site behaves like a shallow donor [94].

Now I turn to a discussion of FPs. According to my results, a plethora of defect pairs are metastable and thus possible to generate. This is due to the huge stiffness of the material, and the reduced role of relaxation and atomic rearrangements compared to CdTe. Thus, for example, in c-FPs the interstitial and the vacancy can be either the nearest- or the second-nearest-neighbors configured. Moreover, the diverse lowest energetic configurations characteristic of C_i are maintained and can form FPs. This is in opposition to FPs in softer CdTe or ZnTe, where the relaxation is much bigger and involves more surrounding atoms. The constituent defects may attract each other in 3C-SiC also at larger distances and in this way the recombination of the remote vacancy and interstitial demands a migration of the interstitial to the vacancy (this is because of the lower diffusion barriers of the interstitials

comparing to the vacancies [92]). In this thesis I analyze the generation and recombination of the following FPs:

(a) a-FPs:

(i) In the nearest-neighbor pair, V_C forms a complex with the split C_i at a silicon site $C_{Si<100>} - V_C$. Here, the only stable configuration is the one containing a three-fold coordinated C_i with a silicon dangling bond. The pair can assume the charge states from 2+ to 1-. The interaction of the p orbital of C_i and the silicon dangling bond of the vacancy located within the same plane gives rise to the formation of the defect states. The corresponding transition energies when coming from 2+ to 1- are 0.5, 0.6, and 1.7 eV, which is in line with those calculated in Ref. 92 (0.4, 0.7, and 1.8 eV, respectively). Due to the origin of the defect states, the recombination in n-type can be understood as a transition from the localized to the delocalized conduction band states [96] and in p-type as the neutralization by an electron transfer – see Fig. 4.1. Because of an additional energy cost in the form of charge transfer to more energetic the CBM in n-type, FPs are expected to manifest more stability from the point of view of a recombination. This is reflected in rising recombination barriers as E_F increases (Table XXIII). The generation of the FP costs a lot of energy, above 4.5 eV. Nevertheless, the binding energies are the biggest among all FPs under study. They are -2.3, -3.1, -3.8, and -4.2 eV for 2+, 1+, 0, and 1- charge state respectively. The E_{form} and generation barriers are the lowest amidst all considered FPs which is mainly due to the origin of the defect state.

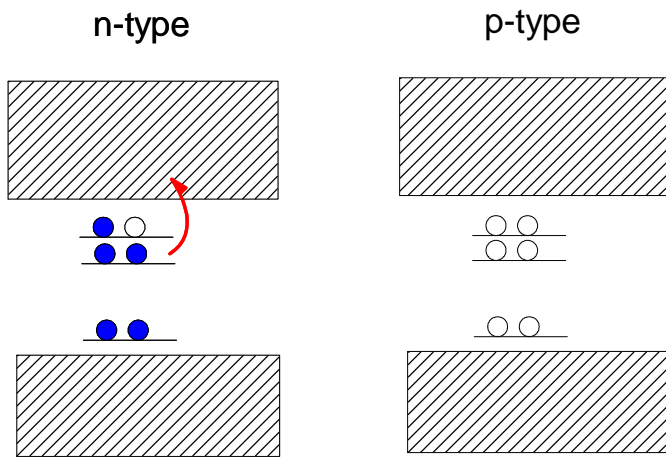


FIG. 4.1. Defect levels of $C_{Si<100>} - V_C$ in 3C-SiC. Red arrow indicates electron transfer required upon recombination in n-type.

(ii) The second-neighbor pair $C_{C<100>} - V_C$ has the interstitial located at the neighboring carbon site. The complex exists in the same charge states like the FP described above and introduces an interstitial-originated defect level in the bandgap. The calculated transition

energies from 2+ to 1- charge state (0.7, 1.0, and 1.7 eV) are within 0.1 eV accuracy compared with the respective values calculated in Ref. 92. The FP is less stable, i.e., the recombination barriers can be about 1 eV lower than those for $C_{\text{Si}<100>} - V_{\text{C}}$. Because both constituents are positively charged in p-type, and as a consequence repel electrostatically each other, the recombination barriers are higher. The formation energies are about 1.5-2 eV higher than for FP described in (i). The binding energies are about -1 eV for all accessible charge states.

(iii) The FP where the tetrahedral Si-coordinated interstitial is displaced along the [111] direction away from a carbon vacancy $C_{\text{Td}} - V_{\text{C}}$ introduces defect levels originated from C_i . The FP can assume four charge states, 2+ through 1- with the corresponding transition energies: 0.8, 0.9, and 1.1 eV. It is worth noting that the isolated tetrahedrally configured C_i is metastable, with E_{form} above 7.5 eV, and relaxes with negligible barrier into split configuration. Despite the stiffness of the host material and the weak metastability of the interstitial constituent $C_{\text{Td}} - V_{\text{C}}$ generation is possible. This is in contrast with the results of Ref. 92, where such a FP was not found to be metastable. The binding energies are approximately -0.5 eV. Nevertheless, the generation barriers are prohibitively large.

(b) c-FPs:

(iv) According to my calculations, the FP where the interstitial is tetrahedrally coordinated at the C site, $\text{Si}_{\text{Td}} - V_{\text{Si}}$, is the only metastable configuration. It exists only in neutral and positive charge states. This was corroborated also in Ref. 92. I found that the FP can recombine via a hop of the interstitial passing close to the adjacent T:Si site (Table XXIII) in contrast to the results of Ref. 92. They acknowledge that instead of the above path an antistructure pair forms $C_{\text{Si}} - \text{Si}_{\text{C}}$. It is accomplished by a hop of the carbon neighbor into the V_{Si} and, simultaneously, the interstitial displacement into the site left by the carbon atom in a concerted manner. The reaction barrier amounts to 3.2 eV for all accessible charge states, which is comparable with the migration barrier of the Si_i at the T:C site. My calculations support the feasibility of this path, but with calculated diffusion barrier of higher than 2.9 eV for any charge state it puts this process lower in hierarchy of annealing mechanisms. It costs at least 1 eV more than the recombination along the [111] direction. The generation barriers are enormous and important only when considering irradiation experiments. The binding energies are not surpassing 0.4 eV.

Rauls *et al.* [97] investigated the recombination of the vacancies with the split C_i in 4H-SiC where only neutral FPs were considered. Similar recombination barriers were found

as in my calculations for 3C-SiC. Furthermore, native defects in 3C-SiC and 4H-SiC bear a close resemblance giving only quantitative differences [88, 94]. These can be explained by the huge stiffness of SiC and the same atomic neighborhood of zinc-blende and wurtzite up to the second nearest neighbors (see Sec. 4.3 for detailed comparison of both crystal structures from the point of view of FP generation). In effect, all substantial atomic arrangements pertinent to the nature of native defects and FPs undergo within the distances that exhibit common atomic configurations in both structures. Thus, no qualitative differences are observed between those crystal structures and a number of configurations is possible. Finally, abundant polytypism can be advocated using the same arguments.

TABLE XXIII. Calculated diffusion barriers (in eV) for different configurations and charge states of a-FPs and c-FPs in 3C-SiC.

Path	Charge state	Barriers			
		Anion sublattice			Cation sublattice
		$C_{Si<100>} - V_C$	$C_{C<100>} - V_C$	$C_{Td} - V_C$	$Si_{Td} - V_{Si}$
sub-FP	-	8.8	9.1	14.1	-
FP-sub	-	1.5	0.4	0.6	-
sub-FP	0	7.6	8.0	13.9	14.6
FP-sub	0	1.4	0.3	0.3	1.3
sub-FP	+	5.1	5.4	12.0	13.6
FP-sub	+	1.2	0.6	0.1	1.5
sub-FP	2+	4.6	4.9	10.0	12.8
FP-sub	2+	1.0	0.9	0.5	1.9

4.3. ZnO

ZnO has recently attracted a lot of attention due to its outstanding versatility in electrical, chemical, and optical properties. Ultraviolet light emission capabilities along with nontrivial problem of p-type doping prodded research community into the detailed investigations of defects in this interesting compound. A number of publications was devoted to the study of native defects in ZnO and various theoretical approaches were employed. Because of different correction schemes implemented, the calculated E_{form} for a given defect differ even by 4 eV. Despite this incumbent, and rather discomfoting situation, intensive, still on-going debate over the pros and cons of the employed correction procedures, some

judicious correction schemes are emerging, and recent results are converging [98-102]. Generally, under the Zn-rich conditions in p-type crystal, the dominance of both the Zn interstitial Zn_i and the oxygen vacancy V_O is pronounced with E_{form} below zero for E_F close to the VBM. For n-type samples, the zinc vacancy V_{Zn} has the lowest E_{form} of about 2 eV, being 2 eV lower than E_{form} of V_O and the tetrahedrally coordinated oxygen interstitial O_i . Under the opposite O-rich conditions, in p-type material, the split O_i is expected to be dominant native defect with E_{form} of about 2 eV. ZnO has substantial concentrations of V_{Zn} due to its near zero E_{form} together with both forms of O_i that have the relatively low E_{form} of about 1 eV. The constituents of investigated FPs have the following properties (these are my results that generally agree with those presented by other authors employing similar computational methodology) :

(i) V_O is deep donor with the lowest E_{form} among all native donors. E_{form} of V_O is very high (~3 eV) in n-type ZnO, and it is much lower (~-1 eV) in p-type ZnO, where V_O assumes the 2+ charge state. In effect, V_O is a potential source of compensation in p-type ZnO. Similar to V_{anion} in CdTe and ZnTe, V_O is a negative- U defect with the $\epsilon_{V_O}(2+/0)$ transition level at 1 eV below the CBM. Moreover, dimerization of Zn neighbors in the neutral charge state is observed which is contrasted with a pronounced outward displacement of the Zn nearest neighbors in 2+ charge state.

(ii) V_{Zn} introduces partially occupied levels in the bandgap near the VBM and acts as an acceptor. V_{Zn} is a deep acceptor with the transition level $\epsilon_{V_{Zn}}(0/1-)$ and $\epsilon_{V_O}(1-/2-)$ amounting respectively to about 0.2 eV and 0.9 eV. Because of acceptorlike behavior V_{Zn} in ZnO easily forms in n-type and under O-rich conditions.

(iii) Zn_i in wurtzite ZnO can assume two interstitial sites: the tetrahedral and the octahedral one. The latter is 0.9 eV more stable than the tetrahedral site for $Q=0$. Due to the high E_{form} in n-type crystal approaching ~6 eV, and thus low concentration, it is unlikely for Zn_i to be responsible for an unintentional n-type doping. Nevertheless, in p-type, being in 2+ charge state, it has E_{form} near zero, and as a consequence, it is a potential source of compensation in p-type. Because throughout accessible E_F , Zn_i is in 2+ charge state, the defect always acts as a shallow donor.

(iv) O_i can assume three nonequivalent configurations: the tetrahedral, the octahedral, and the split one. The first one is not stable. In the octahedral configuration O_i is electrically active, and induces a singlet state in the lower part of the band gap, empty for $Q = 0$. In n-type crystal, being in the 2- charge state, it has E_{form} lower by about 1 eV than the split

configuration. The defect levels are of oxygen p orbitals origin and therefore deep transition acceptor levels at ~ 0.7 eV and ~ 1.6 eV are identified. The split configuration in the neutral charge state, dominating in semi-insulating and p-type material, is electrically inactive. It is not possible to depopulate the gap level of O_i , since its transition level $\varepsilon_{O_i}(1+/0)$ is located below the VBM. In the process of formation, O-O molecule of bond length ~ 1.46 Å (compared to 1.26 Å of an isolated O_2 molecule) two almost degenerate and completely filled states are introduced in the band gap. They resemble the antibonding $pp\pi^*$ state of the isolated O_2 molecule [100, 103]. In an isolated O_2 molecule, the $pp\pi^*$ orbital is occupied with 2 electrons with parallel spins resulting in the triplet ($S=1$) ground state. O_2 in the split configuration has two more electrons from the four zinc nearest neighbors, hence the $pp\pi^*$ orbital is fully occupied. The additional occupation of the antibonding orbital explains the significantly longer bond length of O-O in the solid compared with that of the isolated O_2 molecule.

I investigated the generation of FPs in both zinc-blende and wurtzite ZnO. Various configurations of vacancy-interstitial pairs were analyzed. The results are summarized in Table XXIV and below:

(i) In zinc blende ZnO, for FPs on both sublattices, the interstitial is solely tetrahedrally coordinated. The generation barriers are prohibitively large and exhibit the same trends as it was in the case of CdZnTe and GaAs. c-FPs, $Zn_{Td} - V_{Zn}$, behave like deep donors in opposition to a-FPs which assume an acceptor like dependence of E_F .

(ii) In wurtzite ZnO, only a-FPs exhibit a pronounced metastability, $O_{split} - V_O$, and in this case the interstitial has the split configuration. When the interstitials in FPs occupies either the octahedral or the tetrahedral sites, those interstitials recombine spontaneously with the vacancy. The analysis took into consideration the sites within the radius containing the sixth nearest neighbor of the vacancy. The FPs with a longer separation between V and I are expected to be stable, and behave more like isolated native defects that can obviously migrate [100] and finally recombine. The generation and recombination path of $O_{split} - V_O$ is presented in Fig. 4.2. It is curvilinear and somewhat different in the immediate region of O-O molecule for different charge states. This is mainly due to the different O-O bond lengths for the different charge states. V_O being the constituent of the FP changes the position and availability of the O_2 molecule defect levels comparing to what is valid for the isolated O_2 molecule in the solid ZnO (see Fig. 4.3). In the neutral charge state there are two occupied singlets with energy ~ 0.6 eV above the VBM introduced in the bandgap, ~ 0.25 eV moved

upwards by the interaction with V_O . The upward shift of the defect energy level is also the case for V_O which in the FP has the $\varepsilon_{V_O}(2+/+1)$ and $\varepsilon_{V_O}(1+/0)$ transition levels occurring at around 0.1 eV below the CBM. It is in opposition to the isolated V_O in ZnO, which is negative- U defect which undergoes substantial relaxation in neutral charge state resulting in defect level below the VBM. The relaxation around the V_O in the FP is curtailed, the dimer does not form, and thus the defect level is located below the CBM with rising energy as the level is populated. It means that in p-type and semi-insulating ZnO, V_O is in 2+ charge state introducing an empty singlet close to the CBM. In n-type material, V_O introduces a doubly occupied singlet below the CBM. Consequently, the population and depopulation of the O_{split} levels determine the dependence of the a-FP on E_F . What distinguishes between O_2 being the constituent of a-FP and an isolated O_2 is that in p-type the depopulated defect levels of a FP are above the VBM, while for the O_2 molecule upon the depopulation, the defect level moves below the VBM making the defect electrically inert. As a consequence, in p-type material, the depopulation of the defect states of O_2 molecule can take place. Thus, electrostatic repulsion between ionized O_2 molecule and the V_O^{2+} can stabilize the FP.

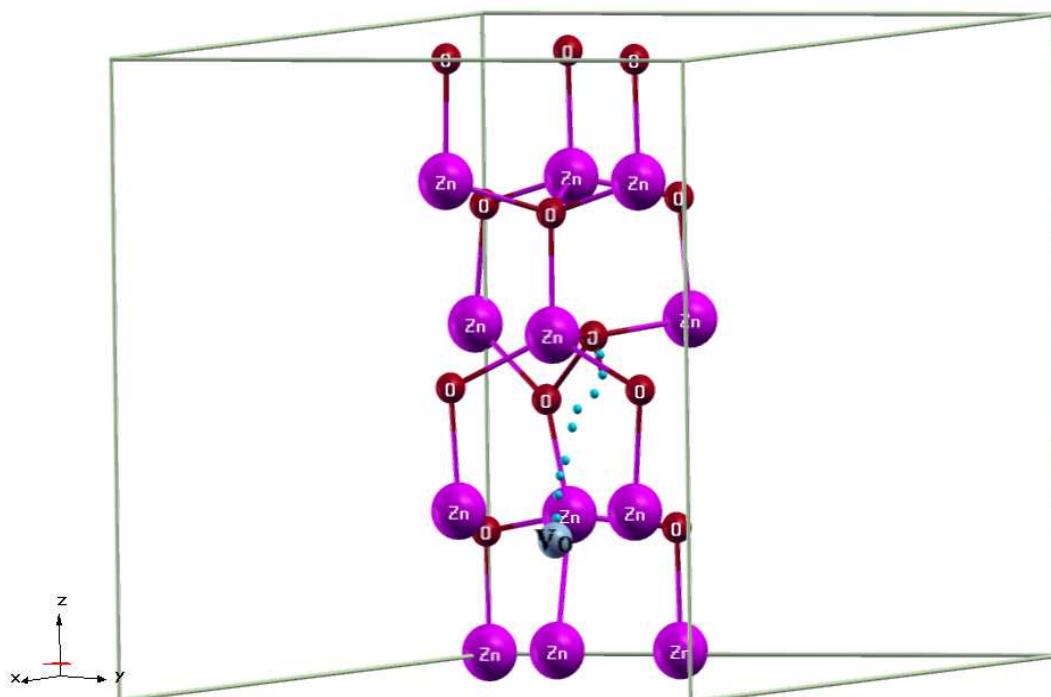


FIG. 4.2. Generation path of $O_{split} - V_O$ in wurtzite ZnO for the neutral charge state.

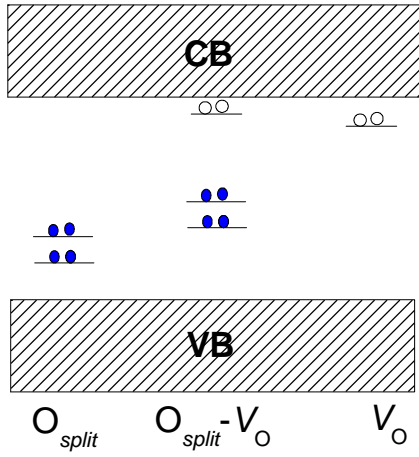


FIG. 4.3. The defect levels of the neutral charged O_{split} , V_O , and $O_{split} - V_O$ in wurtzite ZnO.

TABLE XXIV. Calculated generation and recombination barriers (in eV) for FPs in ZnO.

Path	Charge state	Barriers		
		zinc-blende		wurtzite
		$Zn_{Td} - V_{Zn}$	$O_{Td} - V_O$	$O_{split} - V_O$
sub-FP	2-	5.6	6.5	6.0
FP-sub	2-	1.1	2.8	0.4
sub-FP	1-	5.8	7.6	6.1
FP-sub	1-	1.1	2.4	0.5
sub-FP	0	6.0	7.7	5.7
FP-sub	0	1.3	2.4	0.4
sub-FP	+	6.0	6.1	5.0
FP-sub	+	1.3	1.5	0.4
sub-FP	2+	6.0	5.3	4.4
FP-sub	2+	1.4	1.1	0.6
sub-FP	3+	6.0	4.9	3.8
FP-sub	3+	1.5	1.0	0.9
sub-FP	4+	5.9	4.7	3.5
FP-sub	4+	1.3	1.0	1.1

Besides the electrostatic repulsion between the constituents of a-FP, the depopulation of singlets in p-type is tantamount to the depopulation of electrons in the antibonding $pp\pi^*$ state which stabilizes O_2 molecule. It is reflected in Table XXIV where the increase of the stability of $O_{split} - V_O$ is evident when the charge of the a-FP alters from the neutral to the 4+ state. In effect, the recombination barrier is increased to 1.1 eV for 4+ charge state.

Simultaneously, due to the acceptorlike character of $O_{split} - V_O$, and the rising electrostatic repulsion between the constituents of the FP with the increasing E_F , the generation barriers are also substantially diminished in p-type samples. When all defect levels are depopulated, the generation barrier decreases to 3.5 eV which is comparable to the bandgap (~3.3 eV at the room temperature), and thus also to elementary excitations. It means that p-type ZnO is expected to manifest significant instabilities by the means of the generation of $O_{split} - V_O$, which exhibit a pronounced metastability. From that point of view I reckon that unless microscopic solutions to inhibit the formation of FPs are devised, ZnO is not expected to play an important role in high voltage/ temperature devices that exploit both p-type and n-type form of the compound.

It is interesting to understand why the FPs with the interstitial coordinated differently than O split coordination (obviously except the remote FPs) cannot form FPs in the wurtzite structure. As it is presented in Table XXIV the calculated zinc-blende ZnO assume FPs on both sublattices with the interstitials at the tetrahedral sites, but wurtzite ZnO allows solely the generation of $O_{split} - V_O$. This difference may be surprising, since the local environment of the substitutional atom is very similar in two phases. Namely, the two phases only differ at the positions of third-nearest neighbors and beyond, and no qualitative differences between phases are usually observed for native defects if the given material crystallizes in both phases (see in SiC [88] or GaN [104, 105]). The change of the space-group symmetry from T_d in zinc-blende to C_{6v} in wurtzite arises from the respective change of the stacking sequence from ABC to ABAB. The change of the stacking sequence results in an increase of the fundamental energy gap by about 0.7 eV in the wurtzite case which influences the energetical stability and ionization levels of the defects. The reason for the nonequivalence of wurtzite and zinc-blende structure stems from the different surrounding of the corresponding interstitial sites in both crystal structure (Fig. 4.4). I will discuss them now.

(i) The displacement along the [0001] direction (Fig. 4.4a), analogous to the displacement along the [111] direction in zinc-blende crystals (Fig. 4.4b), leads to the T:site position very close to the substitutional position (red arrow denoted as (1) in Fig. 4.4a). Reaching the next T:site along this direction, possible in the case of the [111] displacement in zinc-blende crystal, is not feasible here because of the Zn atom located on the displacement path. The FP with the interstitial at the T:site position is not even metastable and the atom spontaneously recombines with the vacancy. Nevertheless, the oxygen DX centers in wurtzite $Al_xGa_{1-x}N$ with $x > 0.3$ were found to be stable in such a coordination [106]. Here, the DX center is

stabilized by electrostatic attraction between the negatively charged O_N and the third-nearest neighbors of the oxygen atom along the [0001] direction which are positively charged Al atoms. As a consequence, both the oxygen and Al atoms interact and shortens the mutual distance. The silicon DX center realized by displacement along the [000-1] direction of Si_{Al} is not possible because now negatively charged nitrogen is the third nearest neighbor. It is worth underlining that oxygen DX center is unstable in wurtzite GaN. In zinc-blende crystal the nearest neighbor T:site never favors the creation of the FP due to the fact that the interstitial is surrounded there by four atoms that are not contributing substantially to electrostatic attraction (for example in Fig. 4.4b the O_i at this site is destabilized by four O atoms). Obviously, depopulating the interstitial from electrons lowers the electrostatic repulsion, thus in p-type material the barriers for generation of the a-FPs are lowered.

(ii) There is a hypothetical possibility of stabilization of a more spaced FPs with the interstitial coordinated at the T:site (the red arrow denoted (2) in Fig. 4.4a). Two different counteracting nearest neighbors (the T:site is equidistant from four O and four Zn atoms) destabilize this FP in wurtzite crystal and eventually it spontaneously recombines. This is also the case for the FP with the interstitials at the I_{oct} - or I_{oct}' octahedral-site where the electrostatic attraction is too small to stabilize the FP (here the I_{oct} -site is equidistant from six O and six Zn atoms). In zinc-blende crystal the next nearest T:site coordination stabilizes the FP. The interstitial is attracted by four atoms (for example in Fig. 4.4b the O_i at this site is stabilized by four Zn atoms). The stabilization of the FP can be undermined by the weakening of this attraction, i.e., by making the interstitial less negatively charged. Hence, although p-type material facilitates the overcoming of the generation barrier (which is influenced by electrostatics depicted in the point (i) above), it also lowers the recombination barriers of the a-FP in zinc-blende crystal. This is in opposition to $O_{split} - V_O$, which has the lowered generation barrier and the enlarged recombination barrier in p-type. This is the hallmark of FP in wurtzite ZnO in comparison to the zinc-blende ZnO.

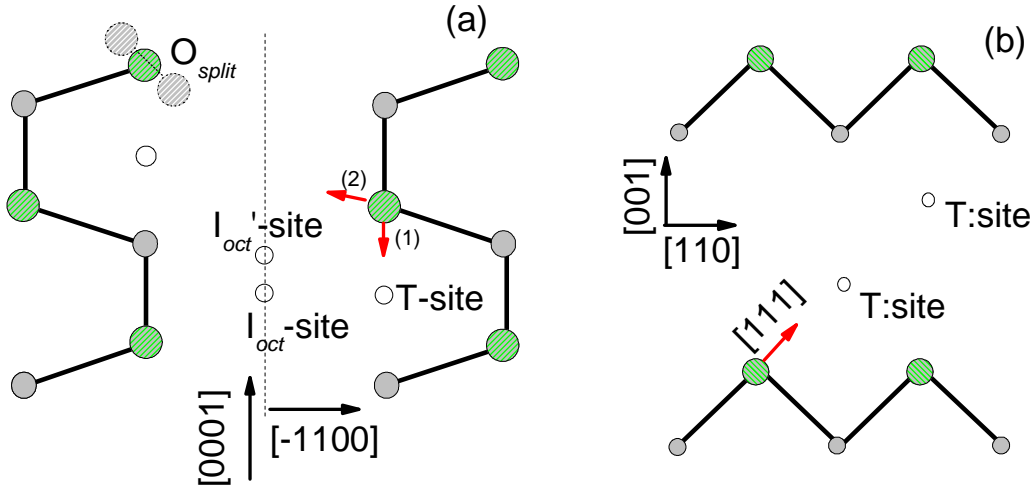


FIG. 4.4. Schematic representation of atomic positions in (a) the (11-20) plane of wurtzite, and (b) the (110) plane of zinc-blende in ZnO. The large green circles represent Zn atoms, medium grey circles O atoms. The high-symmetry interstitial sites are indicated: I_{oct} is the octahedral interstitial site, T the tetrahedral interstitial site. The red arrows indicate possible directions of displacement to generate FP with the T-site coordinated interstitial. I_{oct} sites are out of the plane. O_{split} denotes split that is also out of plane.

4.4. GaN

GaN is a direct-bandgap semiconductor material of wurtzite crystal structure, with a wide (3.4 eV) band gap, used in optoelectronic, high-power and high-frequency devices. It can be produced in zinc blende structure using non-equilibrium growth methods. Because GaN transistors can operate at much higher temperatures and work at much higher voltages than GaAs transistors, the compound is used for ideal power amplifiers at microwave frequencies. The huge number of papers were addressed to investigate native defects in GaN [104-107]. Under Ga-rich conditions, the nitrogen vacancy V_N has E_{form} going into negative values in p-type and the gallium vacancy V_{Ga} has the lowest E_{form} of ~ 1 eV when $E_F = CBM$. In the N-rich limit, both the nitrogen interstitial N_i and V_N are dominating among native defects with E_{form} of ~ 1 eV for p-type material. In n-type, V_{Ga} is responsible for the pinning energy with E_{form} of near zero. The fundamental properties of native defects constituting the investigated FP are following (my results agree with those in Ref. 104 - Ref. 107 within the accuracy of the method and the methodologies used):

(i) V_N behaves as shallow donor with the a_1 state lying close to the VBM, and the t_2 states above the CBM. Because in the neutral charge state there is one electron on the t_2 level that is automatically transferred to the lower-lying CBM, V_N acts always as a donor. It has the transition level $\varepsilon_{V_N}(3+/1+)$ occurring at 0.5 eV above the VBM. The 2+ charge state is never stable which is characteristic of a negative- U defect, and associated with a strikingly large outward lattice relaxation of one of the four atoms surrounding the vacancy. In effect, it raises the energy of the a_1 level and eventually shifts it into the band gap. The rise in the a_1 level can only take place if the level is empty, hence the stabilization of the 3+ charge state. A similar behavior was observed for the V_{As} and V_{Se} in GaAs and ZnSe, respectively. The low E_{form} of the 3+ charge state under p -type conditions indicates that nitrogen vacancies can be a serious source of compensation in p -type GaN.

(ii) V_{Ga} acts as a triple acceptor showing the levels within about 1 eV above the VBM. V_{Ga} has a deep transition level $\varepsilon_{V_{Ga}}(2-/3-)$ about 1.1 eV above the VBM. Transitions between the conduction band (or shallow donors) and this deep level would therefore result in emission around 2.3 eV. Thus, the V_{Ga} has been proposed as the source of the ‘‘yellow luminescence’’.

(iii) N_i has split-interstitial configuration ground state that is strongly energetically preferred over the other metastable configurations (the octahedral and the tetrahedral) because of the large strength of N-N bond. The N-N bond distance varies from 1.1 Å in the 3+ charge, which is then comparable to the bond distance in N_2 , to 1.45 Å in the 1- charge state. The elongation of the N-N bond can be explained in the same manner like it was in the case of O_2 molecule in ZnO. An isolated N_2 molecule has 14 paired electrons in the following molecular orbitals: $ss\sigma$ and $ss\sigma^*$ coming from 1s and 2s (8 electrons), $pp\sigma$ (4 electrons), and HOMO $pp\pi$ (2 electrons). The two $pp\pi^*$ are LUMOs. The N_2 molecule in GaN has three additional electrons from the four Ga atoms which occupy the $pp\pi^*$ antibonding states. These levels are nondegenerate in GaN and introduced in the bandgap. N_i can act both as a acceptor and donor depending on E_F and the defect can assume all charge states from 3+ to 1- with the corresponding transition energies within around 2 eV above the VBM. E_{form} is higher than ~3 eV for all E_F under any growth conditions.

(iv) Ga_i has the ground state that is octahedrally coordinated with pronounced metastability at the T:site. The only stable charge state are 3+ and 1+ with $\varepsilon_{Ga_i}(3+/1+)$ around 1 eV below the CBM. Ga_i introduces a deep donor level and a resonance level above the CBM. Similar as for V_N one electron is automatically donated to the conduction band producing a shallow donor level.

TABLE XXV. Calculated diffusion barriers (in eV) for FPs in GaN.

Path	Charge state	Barriers		
		zinc-blende		wurtzite
		$\text{Ga}_{Td} - V_{\text{Ga}}$	$\text{N}_{Td} - V_{\text{N}}$	$\text{N}_{split} - V_{\text{N}}$
sub-FP	2-	9.1	9.6	5.2
FP-sub	2-	0.3	2.7	0.0
sub-FP	1-	10.1	10.3	5.6
FP-sub	1-	1.0	1.7	0.0
sub-FP	0	11.3	10.9	7.7
FP-sub	0	1.8	0.8	0.0
sub-FP	+	10.8	9.3	6.2
FP-sub	+	2.1	0.1	0.0
sub-FP	2+	10.6	8.4	4.9
FP-sub	2+	2.5	0.0	0.0
sub-FP	3+	10.3	7.5	3.8
FP-sub	3+	2.3	0.0	0.0
sub-FP	4+	10.1	6.6	3.5
FP-sub	4+	2.1	0.0	0.2

The a-FP and c-FP with interstitials at the T: site, split, and I_{oct} -site configurations were investigated in wurtzite GaN within the radius containing the sixth nearest neighbor of the substitutional atom undergoing the displacement. Only $\text{N}_{split} - V_{\text{N}}$ pairs exhibit very weak metastability (the recombination barriers are on the order of the errors pertinent to computational method, except the 4+ charge case). Other FPs under study spontaneously recombine. The reason for this was discussed in Sec. 4.3. The metastability of $\text{N}_{split} - V_{\text{N}}$ is negligible in charge states from 2- to 3+ due to the occupation of the antibonding levels created by the interaction of the singlets pertinent to N_2 molecule and V_{N} . The occupation of these antibonding orbitals obviously destabilizes the FP. Both constituents of the FP when isolated introduce singlets above the VBM (Fig. 4.5). Upon the formation of the FP, the singlet of V_{N} is shifted below the VBM, and the N_2 molecule-originated antibonding levels move upward, mainly because of an additional electron transfer. The defect levels in the bandgap originate mainly from the N_2 molecule levels, but they contain also contribution for V_{N} (Fig. 4.5). This is manifested by wave function square of these levels which are only slightly perturbed and delocalized than those characteristic of N_{split} in GaN. In effect, even in 3+ charge state, the FP has one antibonding level partially occupied, which effectively destabilizes the complex from the point of view of recombination. The depopulation of all antibonding defect levels in the bandgap takes place in 4+ charge state. This increases

recombination barrier to 0.2 eV (Table XXV). To conclude, $N_{split} - V_N$ has an acceptorlike behavior with negligible metastability. Thus, GaN is believed to have a pronounced structural stability from the point of view of the FP generation, which advocates the utilization of this compound in the high temperature/high voltage applications.

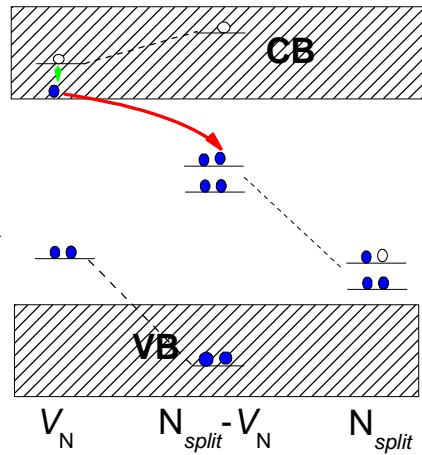


FIG. 4.5. The defect levels of the neutral charged N_{split} , V_N , and $N_{split} - V_N$ in wurtzite GaN.

Both a-FPs and c-FPs in zinc-blende GaN give the results that obey the trends already identified. The generation barriers are enormous (Table XXV), much higher than the accessible excitation energies and the band gap, and therefore the zinc-blende GaN manifests a strong structural stability.

Conclusions

The thesis is dedicated to the study of generation and stability of FPs in the important classes of semiconductors. Formation of FPs is the principal mechanism that defines microscopic structural stability of crystals. First principles approach and state-of-the-art computational methodologies are used. The special treatment is given to the investigation of FPs in CdTe, ZnTe, and their alloys, especially in the context of electronic and magnetic properties, and bistability switching phenomena observed in CdZnTe alloys. Generation of FPs in other semiconductors, namely GaAs, SiC, GaN, and ZnO, is also covered and juxtaposed. A number of important facets are identified, summarized, and listed below.

First, comprehensive investigation of a FP requires the advanced knowledge of native defects that constitute the FP, especially electronic properties, formation energies, and relaxation effects. The stability of a FP has to be researched both from the point of view of recombination and dissociation of its constituents. State-of-the-art Minimum Energy Paths methods (like NEB) are methods of choice for the determination of generation and metastability barriers.

Second, it is informative to delve into a FP starting from isolated defects that constitute it, and analyze contributions from electrons transfer, electrostatic interaction, and relaxation. The binding and formation energies of the FP indicate the stability of the complex which can be further understood by looking at the metastability of the FP.

Third, FPs can be generated on both anion and cation sublattices. The generation barriers are determined by electrostatic interactions of the interstitial and the nearest surrounding at its way to create the FP. Anion-FPs require more energy to form than cation-FPs, mainly due to the lack of contributions from electron transfer and lower electrostatic interaction in the latter case. Upon doping, both generation and recombination barriers can change dramatically. Anion-FPs can lower generation energy in p-type semiconductor, in

opposition to cation-FPs which generation becomes more efficient in n-type samples or in the presence of additional electrons.

Fourth, cation-FPs in CdZnTe alloys have generation barriers of the order of 1.5 eV in n-type samples, which is comparable to the bandgap. Thus, generation of cation-FPs can be important. I attribute switching phenomena observed experimentally in CdZnTe to the possibility of efficient generation of cation-FPs. The generation of the cation-FP in CdZnTe leads to high resistivity state that has distinct optical, symmetry, and magnetic features observed in experiments. Anion-FPs in CdZnTe are prohibitively costly to generate and its constituents tend to dissociate and as a consequence separate each other.

Fifth, the relatively small formation barriers in n-type CdZnTe of cation-FPs in zinc-blende II-VI compounds indicate that FPs creation may be responsible for generation of ‘dark defects’ common in these compounds. They are undesired due to its notorious degradation of LEDs made out of II-VIs and prevent wide market adoption of II-VI LEDs in the industry. FPs in GaAs cost 1 eV more than bandgap, which predispose this compound to LEDs applications operating in normal conditions. Generation of FPs in SiC or wurtzite GaN is prohibitively high cost, which makes microscopical stability very robust in these compounds, and suggests utilization as materials of choice for devices working under extreme conditions. Wurtzite ZnO has pronounced propensity to form anion-FPs in p-type regime, which in the absence of advanced counterbalancing defect engineering disqualifies it as a material in high temperature/voltage/pressure applications.

Sixth, the generation pattern of FPs depends on crystal structure. Generation on both sublattices in zinc-blende is possible, although asymmetric in terms of formation energy. Generation of FPs in wurtzite is possible only on anion sublattice. The tendency to form N₂ or O₂ molecules in bulk GaN and ZnO, respectively, stabilizes the anion-FPs, although not in all charge states.

Moreover, cation-based native defects (cation interstitials and vacancies) in CdZnTe are ‘well behaved’ by means of T_d symmetry conservation, weak relaxation, and standard electronic behavior. I corroborate previous results published by other authors. Cation vacancy is shallow acceptor with relatively small formation energy. Cation interstitial is negative- U deep donor, a dominant hole-killer in p-type regime. It can occupy two nonequivalent tetrahedral sites which become ground state depending on the charge state of the defect. The cation interstitial diffuses along path joining tetrahedral sites with relatively small barriers, which suggest high mobility even at room temperature. The diffusion of cation vacancy, which until my work was not addressed, occur by second neighbor plane-passing mechanism

and also hinges on charge state. There are other channels of diffusion possible, although with higher diffusion barriers.

Finally, anion-based native defects in CdZnTe are not ‘well behaved’, and exhibit pronounced relaxation and symmetry breaking. Only anion vacancy, prior to my work, received substantial consideration, though diffusion was not addressed. Anion vacancy is deep negative- U donor which in a neutral state (i.e., upon capturing two electrons) experiences huge relaxation, symmetry lowering, and gives rise to creation of dimer bonds. When ionized it retains T_d symmetry and is a resonant in CB. It possesses similar diffusion channels like cation vacancy plus additional channel of first neighbor diffusion. Anion interstitial is amphoteric defect undergoing huge atomic reconstruction with the final configurations mimicking configurations valid for elemental Te. It is a common feature, also operative for anion interstitials in ZnO or GaN. The diffusion occurs between reconstructed sites with cation tetrahedral site acting as a barrier.

References

- [1] G. D. Watkins, in *Defects and Diffusion in Silicon Processing*, edited by T. D. de la Rubia *et al.* (MRS, San Francisco, 1997), Vol. 469, pp. 139–150; G. Watkins, in *Properties of Crystalline Silicon*, edited by R. Hull (The Institute of Electrical Engineering, London, 1997), pp. 641–652.
- [2] G. A. Baraff and M. Schlüter, *Phys. Rev. Lett.* **55**, 1327 (1985).
- [3] M. Bockstedte, A. Mattausch, and O. Pankratov, *Phys. Rev. B* **69**, 235202 (2004).
- [4] M. J. Beck, L. Tsetseris, and S. T. Pantelides, *Phys. Rev. Lett.* **99**, 215503 (2007).
- [5] S. Lany and Alex Zunger, *Phys. Rev. Lett.* **100**, 016401 (2008).
- [6] R. Martin, *Electronic Structure: Basic Theory and Practical Methods*, Cambridge University Press, 2006.
- [7] E. G. J. Dreizler, *Density Functional Theory*, Springer Verlag, 1999; P. Hohenberg and W. Kohn, *Phys. Rev.* **136**, B864 (1964).
- [8] W. Kohn and L. J. Sham, *Phys. Rev.* **140**, A1133 (1965).
- [9] J. P. Perdew, J. A. Chevary, S. H. Vosko, K. A. Jackson, M. R. Pederson, D. J. Singh, and C. Fiolhais, *Phys. Rev. B* **46**, 6671 (1992); J. P. Perdew, K. Burke, and M. Ernzerhof, *Phys. Rev. Lett.* **77**, 3865 (1996).
- [10] S. Baroni, A. Dal Corso, S. de Gironcoli, and P. Giannozzi (<http://www.pwscf.org>).
- [11] D. Vanderbilt, *Phys. Rev. B* **41**, 7892 (1990).
- [12] M. Methfessel and A. T. Paxton, *Phys. Rev. B* **40**, 3616 (1989).
- [13] H. J. Monkhorst and J. D. Pack, *Phys. Rev. B* **13**, 5188 (1976).
- [14] C. Kittel, *Introduction to Solid State Physics* (Wiley, New York, 1996).
- [15] M. J. Kirton, P. W. Bank, L. D. Lian, and M. Jaros, *J. Phys. C* **17**, 2487 (1984).
- [16] T. Soma, *J. Phys. C* **11**, 2669 (1978).

- [17] W. A. Harrison, *Electronic Structure and Properties of Solids* (Freeman, San Francisco, 1980).
- [18] See for example, C. Persson, Y.-J. Zhao, S. Lany, and Alex Zunger, *Phys. Rev. B* **72**, 035211 (2005); C. G. Van der Walle, and J. Neugebauer, *J. Appl. Phys.* **95**, 3851 (2004).
- [19] P. Bogusławski and J. Bernholc, *Phys. Rev. B* **56**, 9496 (1997).
- [20] Y. Bar-Yam and J. D. Joannopoulos, *Phys. Rev. B* **30**, 1844 (1984).
- [21] G. Makov, M. C. Payne, *Phys. Rev. B* **51**, 4014 (1995).
- [22] M. Gaio and P. L. Silvestrelli, *Phys. Rev. B* **79**, 012102 (2009).
- [23] See, e.g., G. B. Bachelet, G. A. Baraff, and M. Schluter, *Phys. Rev. B* **24**, 4736 (1981).
- [24] G. Kresse and J. Hafner, *Phys. Rev. B* **47**, R558 (1993).
- [25] M. S. Hybertsen and S. G. Louie, *Phys. Rev. Lett.* **55**, 1418 (1985).
- [26] A. Janotti and Chris. G. Van de Walle, *J. Cr. Growth* **287** (2006) 58-65.
- [27] S. Lany and Alex Zunger, *Phys. Rev. B* **72**, 035215 (2005).
- [28] F. Oba, A. Togo, I. Tanaka, J. Paier, and G. Kresse, *Phys. Rev. B* **77**, 245202 (2008).
- [29] C. Freysoldt, J. Neugebauer, and C. G. Van de Walle, *Phys. Rev. Lett.* **102**, 016402 (2009).
- [30] J. Lento, J-L. Mozos, and R. M. Nieminen, *J. Phys.: Condens. Matter* **14**, 2637 (2002).
- [31] R. Elber and M. Karplus, *Chem. Phys. Lett.* **139**, 375 (1987).
- [32] G. Henkelman and H. Jónsson, *J. Chem. Phys.* **113**, 9978 (2000).
- [33] G. Henkelman, B. P. Uberuaga, and H. Jónsson, *J. Chem. Phys.* **113**, 9901 (2000).
- [33] W. E. W. Ren, and E. Vanden-Eijnden, *Phys. Rev. B* **66**, 052301 (2002).
- [34] C. Dellago, P. G. Bolhuis, F. S. Csajka, and D. Chandler, *J. Chem. Phys.* **108**, 1964 (1997).
- [35] D. Passerone and M. Parrinello, *Phys. Rev. Lett.* **87**, 108302 (2001).
- [36] A. Laio and M. Parrinello, *Proc. Nat. acad. Sci. U.S.A.* **99**, 12562 (2002).
- [37] Carlo Sbraccia, *Computer Simulation of Thermally Activated Processes*, PhD thesis, SISSA (Italy), February 2005.
- [38] P. Pulay, *Chem. Phys. Lett.* **73**, 393 (1980).
- [39] S.-H. Wei and S. B. Zhang, *Phys. Rev. B* **66**, 155211 (2002).
- [40] Yia-Chung Chang, R. B. James, and J. W. Davenport, *Phys. Rev. B* **73**, 035211 (2006).
- [41] M. J. Puska, S. Poykko, M. Pesola, and R. M. Nieminen, *Phys. Rev. B* **58**, 1318 (1998).
- [42] M. Bockstedte and M. Scheffler, *Z. Phys. Chem. (Munich)* **200**, 195 (1997).
- [43] F. El-Mellouhi and N. Mousseau, *Phys. Rev. B* **74**, 205207 (2006).

- [44] P. E. Blöchl, E. Smargiassi, R. Car, D. B. Laks, W. Andreoni, and S. T. Pantelides, *Phys. Rev. Lett.* **70**, 2435 (1993); F. El-Mellouhi, N. Mousseau, and P. Ordejón, *Phys. Rev. B* **70**, 205202 (2004).
- [45] F. Wooten, K. Winer, and D. Weaire, *Phys. Rev. Lett.* **54**, 1392 (1985).
- [46] G. M. Dalpian and S.-H. Wei, *Phys. Rev. B* **72**, 075208 (2005).
- [47] T. M. Duc, C. Hsu, and J. P. Faurie, *Phys. Rev. Lett.* **58**, 1127 (1987).
- [48] J. C. Bourgoin and J. W. Corbett, in *Lattice Defects in Semiconductors*, edited by F. A. Huntley, IOP Conference Proceedings No. 23 (Institute of Physics, Bristol, 1975), p. 149.
- [49] M. Illgner, H. Overhof, *Phys. Rev. B* **54**, 2505 (1996).
- [50] J.E. Northrup, S.B. Zhang, *Phys. Rev. B* **50**, R4962 (1994); A. Garcia, J.E. Northrup, *Phys. Rev. Lett.* **74**, 1131 (1995).
- [51] S. Lany and Alex Zunger, *Phys. Rev. B* **72**, 035215 (2005).
- [52] S. Lany and Alex Zunger, *Phys. Rev. Lett.* **93**, 156404 (2004).
- [53] S. Lany, V. Ostheimer, H. Wolf, and Th. Wichert, *Physica B* 308-310 (2001) 958.
- [54] see for example A. Janotti and Chris G. Van de Walle, *Phys. Rev. B* **76**, 165202 (2007); Chris G. Van de Walle and J. Neugebauer, *J. Appl. Phys.* **95**, 3851 (2004).
- [55] S. B. Zhang, S.-H. Wei, and Alex Zunger, *J. Appl. Phys.* **83**, 3192 (1998).
- [56] S. Lany, H. Wolf, and T. Wichert, *Phys. Rev. Lett.* **92**, 225504 (2004).
- [57] J. Dabrowski and M. Scheffler, *Phys. Rev. Lett.* **60**, 2183 (1988); D. J. Chadi and K. J. Chang, *Phys. Rev. Lett.* **60**, 2187 (1988); D. J. Chadi and K. J. Chang, *Phys. Rev. Lett.* **61** 873 (1988).
- [58] S.-H. Wei and S. B. Zhang, *Phys. Rev. B* **66**, 155211 (2002).
- [59] S.-H. Wei, S. B. Zhang, and Alex Zunger, *Phys. Rev. Lett.* **70**, 1639 (1993).
- [60] H. Raebiger, S. Lany, and Alex Zunger, *Nature* **453**, 763 (2008).
- [61] D. J. Fu, J. C. Lee, S. W. Choi, S. J. Lee, T. W. Kang, M. S. Jang, H. I. Lee, and Y. D. Woo, *Appl. Phys. Lett.* **81**, 5207 (2002).
- [62] T. Wojciechowski, E. Janik, E. Dynowska, K. Fronc, and G. Karczewski, *phys. stat. sol. (c)* **3**, No. 4, 1197-1200 (2006).
- [63] P. van der Sluis, *Appl. Phys. Lett.* **82**, 4089 (2003).
- [64] L. Benguigui, R. Weil, E. Muranevich, A. Chack, and E. Fredj, *J. Appl. Phys.* **74**, 513 (1993).
- [65] D. J. Fu, J. C. Lee, S. W. Choi, C. S. Park, G. N. Panin, T. W. Kang, X. J. Fan, *Appl. Phys. Lett.* **83**, 2214 (2003).
- [66] R. Weil, R. Nkum, E. Muranevich, and L. Benguigui, *Phys. Rev. Lett.* **62**, 2744 (1988).

- [67] Y. Hotta, E. Rokuta, H. Tabata, H. Kobayashi, and T. Kawai, *Appl. Phys. Lett.* **78**, 3283 (2001).
- [68] Y. Hotta, E. Rokuta, J.-H. Jhoi, H. Tabata, H. Kobayashi, and T. Kawai, *Appl. Phys. Lett.* **80**, 3180 (2002).
- [69] Y. Yoneda, N. Matsumoto, K. Suzuya, S. Kohara, and J. Mizuki, *Ferroelectrics* **268**, 697 (2002).
- [70] I. Stolichnov, E. Colla, N. Setter, T. Wojciechowski, E. Janik, and G. Karczewski, *Phys. Rev. Lett.* **97**, 247601 (2006).
- [71] T. Wojciechowski, P. Jakubas, P. Bogusławski, and G. Karczewski, *J. of Korean Phys. Soc.* **53** (1): 23-27 Jul 2008.
- [72] P. W. M. Blom, R. M. Wolf, J. F. M. Cillessen, and M. P. C. M. Krijn, *Phys. Rev. Lett.* **73**, 2107 (1994).
- [73] S.-H. Wei and Alex Zunger, *Phys. Rev B* **35**, 2340 (1987).
- [74] J. Osorio-Guillen, S. Lany, S. V. Barabash, and Alex Zunger, *Phys. Rev. Lett.* **96**, 107203 (2006).
- [75] T. Wojciechowski, P. Jakubas, V. Kolkovsky, K. Świątek, W. Knoff, T. Story, P. Bogusławski, and G. Karczewski, conference paper in 29th International Conference on the Physics of Semiconductors, Rio de Janeiro (Brazil) – 2008.
- [76] G. A. Baraff and M. Schlüter, *Phys. Rev. Lett.* **55**, 1327 (1985).
- [77] G. A. Baraff and M. Schlüter, *Phys. Rev. B* **33**, 7346 (1986).
- [78] S. B. Zhang and J. E. Northrup, *Phys. Rev. Lett.* **67**, 2339 (1991).
- [79] S. Poykko, M. J. Puska, and R. M. Nieminen, *Phys. Rev. B* **53**, 3813 (1996).
- [80] K. Laasonen, R. M. Nieminen, and M. J. Puska, *Phys. Rev. B* **45**, 4122 (1992).
- [81] J. E. Northrup and S. B. Zhang, *Phys. Rev. B* **50**, 4962 (1994).
- [82] H. Seong and L. J. Lewis, *Phys. Rev. B* **52**, 5675 (1995).
- [83] J. T. Schick, C. G. Morgan, and P. Papoulias, *Phys. Rev. B* **66**, 195302 (2002).
- [84] T. E. M. Staab, R. M. Nieminen, J. Gebauer, R. Krause-Rehberg, M. Luysberg, M. Haugk, and Th. Frauenheim, *Phys. Rev. Lett.* **87**, 045504 (2001).
- [85] D. J. Chadi, *Phys. Rev. B* **46**, 9400 (1992).
- [86] M.-A. Malouin, F. El-Mellouhi, and N. Rousseau, *Phys. Rev. B* **76**, 045211 (2007)
- [87] *Handbook of Chemistry and Physics*, 83rd ed., edited by D. R. Lide (CRC, Boca Raton, FL, 2003).
- [88] A. Zywietz, J. Furthmüller, and F. Bechstedt, *Phys. Rev. B* **59**, 15166 (1999).

- [89] F. Gao, E. J. Bylaska, W. J. Weber, and L. R. Corrales, *Phys. Rev. B* **64**, 245208 (2001) and references therein.
- [90] C. Wang, J. Bernholc, and R. F. Davis, *Phys. Rev. B* **38**, 12752 (1988).
- [91] F. Gao, W. J. Weber, M. Posselt, and V. Belko, *Phys. Rev. B* **69**, 245205 (2004).
- [92] M. Bockstedte, A. Mattausch, and O. Pankratov, *Phys. Rev. B* **69**, 235202 (2004).
- [93] L. Torpo, S. Poykko, and R. M. Nieminen, *Phys. Rev. B* **57**, 6243 (1998).
- [94] J. Lento, L. Torpo, T.E.M. Staab, and R. M. Nieminen, *J.Phys.: Condens. Matter* **16**, 1053 (2004).
- [95] Oksana Volnianska, *Theory of magnetic properties based on atomic p-orbitals in perfect and defected solids*, PhD thesis, Institute of Physics, Polish Academy of Sciences (Poland), September 2009.
- [96] P. R. Kent and Alex Zunger, *Phys. Rev. Lett.* **86**, 2613 (2001); P. R. Kent and Alex Zunger, *Phys. Rev. B* **64**, 115208 (2001).
- [97] E. Rauls, T.E.M. Staab, Z. Hajnal, and T. Frauenheim, *Physica B* **308-310**, 645 (2001).
- [98] S. Lany and Alex Zunger, *Phys. Rev. B* **78**, 235104 (2008).
- [99] C. Freysoldt, J. Neugebauer, and C. G. Van de Walle, *Phys. Rev. Lett.* **102**, 016402 (2009).
- [100] A. Janotti and C. G. Van de Walle, *Phys. Rev. B* **76**, 165202 (2007).
- [101] F. Oba, A. Togo, I. Tanaka, J. Paier, and G. Kresse, *Phys. Rev. B* **77**, 245202 (2008).
- [102] P. Rinke, A. Janotti, M. Scheffler, and C. G. Van de Walle, *Phys. Rev. Lett.* **102**, 026402 (2009).
- [103] S. Limpijumnong, X. Li, S.-H. Wei, and S. B. Zhang, *Appl. Phys. Lett.* **86**, 211910 (2005).
- [104] C. G. Van de Walle and J. Neugebauer, *J. Appl. Phys.* **95**, 3851 (2004).
- [105] J. Neugebauer and C. G. Van de Walle, in *Diamond, SiC and Nitride Wide Bandgap Semiconductors*, edited by C. H. Carter, Jr., G. Goldenblat, S. Nakamura, and R. J. Nemanich, MRS Symposia Proceedings No. 339 (Materials Research Society, Pittsburgh, 1994), p. 687.
- [106] C. G. Van de Walle, *Phys. Rev. B* **57**, R2033 (1998).
- [107] P. Boguslawski and J. Bernholc, *Phys. Rev. B* **56**, 9496 (1997).